Laminated glass: dynamic rupture of adhesion

Paul Elzière

Université Pierre et Marie Curie

École Doctorale 397 : Physique et Chimie des Matériaux

Saint-Gobain / Laboratoire SIMM

Verre feuilleté : rupture dynamique d'adhésion

Paul Elzière

Thèse de doctorat en physico-chimie des polymères

Dirigée par Matteo Ciccotti, Étienne Barthel et Cécile Dalle-Ferrier

Présentée et soutenue publiquement le 29 septembre 2016

Devant un jury composé de:

R. Estevez	Professeur – INP Grenoble	Président du Jury
L. Leger	Professeur émerite – Université Paris Sud	Rapporteurs
T. Pardoen	Professeur – Université Catholique de Louvain	
C. Maurini	Maître de Conférences – IJLRA/UPMC	Examinateur
M. Ciccotti	Professeur – ESPCI Paris	Directeur de thèse
E. Barthel	Directeur de Recherches CNRS – SIMM/ESPCI Paris	Co-directeurs de thèse
C. Dalle-Ferrier	Saint-Gobain Glass	

Laminated glass: dynamic rupture of adhesion

Paul Elzière

Matteo Ciccotti, Étienne Barthel and Cécile Dalle-Ferrier

September 29th, 2016

Remerciements

Je voudrais remercier tout d'abord mes trois encadrants Matteo Ciccotti, Étienne Barthel et Cécile Dalle-Ferrier.

Je souhaite témoigner ma reconnaissance à Matteo Ciccoti, pour sa confiance, ses conseils précieux, son enseignement patient de la mécanique des polymères et de la fracture, sa bonne humeur constante et la passion communicative dont il fait preuve dans son travail.

Je veux faire part de ma plus profonde gratitude à Étienne Barthel pour sa disponibilité, ses innombrables conseils, son soutien sans faille et surtout sa patience tout au long de ce projet lorsque, trop souvent, je venais interrompre son travail.

J'aimerais adresser à Cécile Dalle-Ferrier mes plus chaleureux remerciements pour la confiance qu'elle a bien voulu m'accorder, pour avoir initié, poussé et accompagné ce projet, pour la chance qu'elle m'a donnée de travailler au plus près de l'outil industriel ainsi que pour les discussions que nous avons eu sur le monde de l'entreprise et tant d'autre sujets.

Je voudrais remercier ensuite les membres du jury qui ont généreusement pris le temps de relire et de commenter ce document ainsi que pour les discussions que nous avons eu lors de la soutenance.

Ce travail n'aurait pu avoir lieu sans le soutien financier de Saint-Gobain Recherche. Je souhaite remercier Mathieu Joanicot et François Creuzet, directeurs de la recherche du centre de R&D d'Aubervilliers, pour leur soutien et leur suivi du projet.

Je tiens à remercier Vincent Rachet pour avoir initié cette thèse et avoir soutenu et suivi le projet mais aussi pour ses conseils sur mon projet professionnel et son accueil chaleureux au centre R&D de Sully-sur-Loire.

J'ai eu la chance de pouvoir intégrer une équipe industrielle qui m'a toujours accueilli avec bonne humeur et je tiens à remercier toute l'équipe PIL de Saint-Gobain Recherche et en particulier : Joel Azevedo, Julien Beaumont, Jaona Girard, Hans Herbert, Diamante Mace, Caroline Parneix, Joel Robineau, Cyrielle Rudaz, Tamar Saison, et Leila Tahroucht. Je voudrais aussi remercier tous ceux qui à Saint-Gobain m'ont aidé pour mes expériences, pour la compréhension et la modélisation des phénomènes observés ou avec qui j'ai eu le plaisir de discuter : Alessandro Benedetto, Ivan Berline, Pierrick Cavalie, Samuel Dubrenat, Alexandre Kerambloch, Jean-Yvon Faou, Maxime Van Landeghem...

En particulier, je veux remercier Nathalie Dideron qui a eu la patience de me former à mon arrivée et qui, avec gentillesse, a su m'encourager et m'aider durant

ces trois années et sans qui ce projet n'existerait pas.

Je souhaite aussi remercier Marie Lamblet et Hélène Lannibois-Dréan pour l'intérêt qu'elles ont porté à ce projet, leur suivi assidu, leur aide et leurs conseils tant scientifiques que sur le monde de l'entreprise.

Je voudrais remercier Alexis Chenneviere et Keyvan Piroird pour leur aide et leur contribution à mon travail. Je veux aussi exprimer ma gratitude à René Gy, pour son intérêt pour le projet, pour avoir participé à tous mes points d'avancements et ses remarques et conseils. Je voudrais également adresser mes remerciements à Romain Decourcelle qui a lui aussi travaillé sur ce sujet durant sa thèse, pour son suivi de ce projet avec intérêt et les échanges que nous avons pu avoir. Je remercie également Jean Charles-Sauvesty pour son aide sur les éléments finis.

Au cours de ma scolarité à l'ESPCI j'ai eu la chance de pouvoir travailler à de nombreuses reprises au sein du laboratoire SIMM : aussi, je souhaite remercier très chaleureusement Christian Fretigny directeur du laboratoire et Guylaine Ducouret directrice adjointe, pour m'avoir accueilli dans cette unité durant toutes ces années. Mes très sincères remerciements à Costantino Creton pour m'avoir accueilli au sein de son équipe et pour les nombreuses discussions et ses conseils pertinents ainsi que pour avoir partagé sa passion du vin et de la table avec nous.

J'exprime ma profonde reconnaissance à Alba Marcellan qui m'a donné le gout des polymères et de la mécanique des matériaux et qui m'a permis de vivre des aventures scientifiques riches et passionnantes.

Je tiens également à remercier tous les permanents du laboratoire et en particulier ceux qui ont toujours eu un moment pour discuter avec moi d'un problème pratique ou plus philosophique. J'ai pu en effet apprécier au cours de ces années dans le laboratoire, la disponibilité des chercheurs pour m'aider à surmonter les obstacles que nous pouvions rencontrer. Ainsi je tiens à remercier: Sabine Cantournet, Antoine Chateauminois, Dominique Hourdet, François Lequeux, Hélène Montès, Laurence Talini, Yvette Tran et Emilie Verneuil.

Je voudrais aussi remercier les personnes qui font vivre le laboratoire au quotidien et sans qui nos efforts ne pourraient aboutir: Pierre Christine, Gilles Garnaud, Pierre Landais et Flore Lasaone, mais aussi Armand Hakopian, à qui je promets de ne rien modifier sur les serveurs en partant, Freddy Martin esprit et corps de ce laboratoire, Bruno Bresson et ceux qu'on ne remercie plus, Ludovic Olanier et David Martina pour leur aide et leurs conseils dans le montage de mes expériences. Je souhaite adresser des remerciements très particuliers à Mohamed Hanafi pour m'avoir aidé dans la réalisation des expériences de DSC et dans l'analyse des résultats.

Cette thèse s'est faite dans la joie et la bonne humeur, cela n'aurait pas été possible sans tous les stagiaires, doctorants et post-doctorants qui constituent le cœur de ce laboratoire. Je voudrais commencer par remercier mes co-bureaux présents et passés: Francisco Cedano, Jessica Delavoipiere, Richard Villey et Jingwen Zhao qui ont enduré mes sautes d'humeurs. Je voudrais aussi remercier les différents bureaux de l'escalier H, Romain Dubourget, Natacha Goutay, Jennifer Macron et Cécile Mussault, Benjamin Chollet, Robert Gurney, Anne-Charlotte Le Gulluche et Pierre Millereau, Alice Boursier, Davide Colombo, Pierre Gelineau et Robin Masurel, pour leur patience exceptionnelle lors de mes visites quotidiennes mais aussi pour les bons moments que nous avons partagés au travail et en dehors. Merci également à Quentin Demassieux qui a non seulement été un excellent camarade mais qui a aussi contributé aux expériences de SAXS. Je voudrais aussi remercier mes amis de la $128^{ème}$ promotion avec qui j'ai partagé ces trois années au SIMM, Pascaline Hayoun, Marine Protat et Marc Yonger. Sans pouvoir les citer tous je voudrais remercier les personnes avec qui j'ai partagé rires, bons moments et conseils précieux: Mélanie Arangalage, Charles Barrand, Laure Bluteau, Xavier Caliès, Julien Chopin, Rémi Deleurence, Étienne Ducrot, Guillaume Fisher, Hui Guo, Thitima Limpanichpakdee, Éric Lintingre, Ekkachai Martwong, Yannick Nziakou, Séverine Roses, Tom Saint-Martin, Corentin Tregouet, Pauline Valois, Judith Wollbrett-Blitz,...

Je souhaiterait également remercier les professeurs Chung-Yuen Hui et Anand Jagota pour leurs enseignements et les longues et riches discussions qu'ils ont bien voulu avoir avec moi. Je veux aussi remercier toutes les personnes qui ont pris le temps de discuter de mon sujet et qui ont participé ainsi à la construction de ce projet: José Bico, Guillaume Parry, Suomi Ponce, Claire Prada-Julia, Samuel Raetz et Benoît Roman.

Durant cette thèse j'ai eu la chance d'encadrer et de travailler avec Louis Debertrand et Noëlig Daggorn. Je souhaite les remercier pour leur importante contribution à mon travail. Je voudrais aussi remercier Raphaëlle Kullis qui a réalisé un travail exceptionnel au cours de son stage.

Un immense merci à mes très chers amis Adrien, Loic, Nathalie, Nicolas, Samy, Sarah et Yann qui ont toujours été là pour moi. Un très très gros merci également à Adrien, Nicolas, Thomas, Ugo et Ève pour les copieux repas que nous avons partagés et les heures passées sur nos jeux favoris. Enfin un très grand merci à Charlène pour son oreille attentive et son amitié durant toutes ces années.

Il me faut à ce stade avoir une pensé spéciale pour le raton...

Je ne pourrais jamais assez remercier ma sœur et mes parents qui ont toujours été à mes côtés.

Enfin, je dédie ce travail à mes grands-parents qui sont pour moi une source d'inspiration et de courage:

Βασιλική και Σταύρος Παπαγιάννης Simone et Pierre Elzière

Contents

Table of Abbreviations

Interlayer Behavior

σ_{T}	Uniaxial traction true stress
ϵ_{T}	Uniaxial traction nominal strain
λ	Uniaxial traction stretch
μ	Shear modulus
E	Young modulus
τ_i	Viscoelastic relaxation times
λ_m	Maximal chain extensibility

Through Crack Tensile Test and Finite Element Modeling

h	Interlayer thickness
w	Laminated glass sample width
δ	Applied displacement
$\dot{\delta}$	Applied velocity
a	Position of the delamination front relative to the glass crack
x_{F}	Distance to the point at the vertical of the delamination front
F_{TCT}	Delamination force
F^0_{TCT}	Delamination force, steady state value
ϵ_{TCT}	Delamination nominal strain
$\epsilon^0_{\mathrm{TCT}}$	Delamination nominal strain, steady state value
G_m	Macroscopic work of fracture
Γ_{bulk}	Bulk stretching work
Γ^{visco}_{bulk}	Viscoelastic losses part of the bulk stretching work
Γ^{el}_{bulk}	Elastic part of the bulk stretching work
Π_{bulk}	Volumic density of the bulk stretching work
Γ_{crack}	Near crack work of fracture
Γ_s	Separation work (molecular scale at the interface)

Chapter 1

Introduction

1.1 A brief industrial history of laminated glass

Glass has been used in housings for about 2000 years and in vehicles for more than a century for its transparency and elegance. However, its poor mechanical resistance and other issues, in relation to its poor thermal and sound insulation, prevented it to be used as a structural material in buildings. It is only thanks to some improvements of these properties that glass was made suitable for use as one of the main building materials. For example, multiple glazing and the use of an inert gas in between the two glazings reduce heat transfer. Glass surface treatment enables new properties such as hydrophilic self-cleaning glasses or active glasses which can be tinted at will under the action of an electric field. Finally, the mechanical properties of glass and especially its resistance to impact, were improved through toughened or laminated glass. It made it suitable for safety applications in housings and vehicles.

Laminated glass and toughened glass are often mistaken even if these two materials are really different and do not bring the same safety features. Toughened glass results from a rapid cooling of glass plates which traps tension stresses in the glass volume and compression stresses at the surface of the glass. This surface precompression increases the resistance to fracture of the material. It can also be obtained thanks to chemical treatments. Toughened glass is also used because it breaks into small, smooth and thus less dangerous pieces. However, due to the negligible dissipation these glass are not suitable for impact resistance. On the other hand, laminated glass is made of an elastomeric interlayer sandwiched in between two glass plates. Dissipation mechanisms increase the performance to impact of the glass structure. The adhesion between the glass and the interlayer furthermore prevents flying glass parts, which might lead to severe injuries when a glass wall or a windshield is im-

pacted. Finally, laminated glass will keep the structural integrity of the glass plate, which is of special interest in some harsh conditions such as hurricane.

Laminated glass was discovered by Edouard Benedictus a French artist (1878-1930) who dropped a glass flask containing a cellulose based glue. The flask presented cracks in the glass but the whole structure remained. This discovery occurred in 1903 [1]. Several patents were written beginning in 1909 and the *Société du Verre Triplex* (a company partially bought by Saint-Gobain in 1928) started to commercialize the *Triplex* glass for car windshields. Back then, laminated glass was made of two glass plates of 2.5 mm thickness and the glass surface was cleaned and coated with a 10 µm gelatin film which was dried before another wet collodon based layer was applied. This last layer was used as an adhesion primer. Then a celluloid layer was put in between the two glasses. The laminated structure was finally immersed in alcohol which helped remove air bubbles before it was pressed while heating. A mastic was also applied on the edge of the glass to protect the interlayer from external atmosphere. The celluloid interlayer presented at least two drawbacks. First it yellowed while aging and it was also delaminating from the glass quite easily. It was replaced by a Poly(VinylButyral) (PVB) in the 40's-50's.

This is still the mostly used interlayer for laminated glass. Other interlayers such as Polyurethane (PU) or EthyVinylAlcool (EVA) are used for different applications. Indeed, laminated glasses are used in a wide range of applications. In cars, it is used for windshields, for roofs and in some lateral car glass on premium cars. In housing the variety of applications is also quite large. Laminated glass is used for the external glass of buildings as well as inside panels and walls. Its high resistance to static loading and impact makes it suitable for floors and ceilings. Polyurethane is used for plane windshields or other high performance applications. EVA is mainly used in solar photovoltaïc panels and for lower impact performance and lower cost applications. Printed interlayers are also available and thus laminated glass can be used as a decorative piece inside the housing. Some famous example of usage of Saint-Gobain laminated glass in remarkable buildings are the Louvre Museum pyramid, or at the first floor of the "Tour-Eiffel",...

It can be seen through this brief history of laminated glass that the industrial "know how" is really old. However the mechanical response of the laminated glass structure during an impact remains a puzzling question. Impact is a complex problem which involves different mechanical processes: glass rupture, interface breakage and interlayer stretching.

1.2 Impact on laminated glass

1.2.1 Standard tests

Because laminated glass is mainly used as a safety product, it has to comply with different standard tests depending on the final application. These tests may slightly vary from one country to another. Their general aim however is hopefully to reproduce the type of loading to which the laminated structure will be subjected during an impact. We will present here two different tests used in France and Europe to qualify building glasses.

Pendulum test – EN 12600 [2]

The pendulum test is supposed to reproduce the impact of a human body falling onto a window or a glass wall. The functionality that is tested aims at preventing the fall of a person through the glass and the injuries which might be induced by the glass splinters.

The tests are performed on samples of approximately two square meters. The tests are conducted at room temperature and they have to be repeated at least on four samples of the same laminated glass. A weight of 50 kg with two inflated tires around it (which are supposed to reproduce the mechanical behavior of a human body), is dropped from an increasing height on the glass (Figure 1.1). Three falling heights are considered and the materials are ranked according to the maximal falling height they can sustain. It does not necessarily mean that the glass is not broken but that if it does, it will break in a specific manner which hopefully will not arm the occupants of the building.

Ball drop test – EN 356 [3]

This test is used to qualify the resistance of laminated glass against manual attack. Thus its main target is the use of laminated glass in applications such as showcases or ground floor housings. A steel ball of 4 kg and 100 mm diameter falls from different heights on an approximately one square meter laminated glass plate (Figure 1.2). The ball is dropped three times on the glass at the summits of an equilateral triangle. The test is conducted at ambient temperature. The test is passed if the ball does not go through the glass in the five seconds following the impact. The laminated structure is ranked from P1A to P4A which corresponds to drop height going from 1.5 m to 9 m (A P5A class is also used for structure holding 9 drops from 9 m).

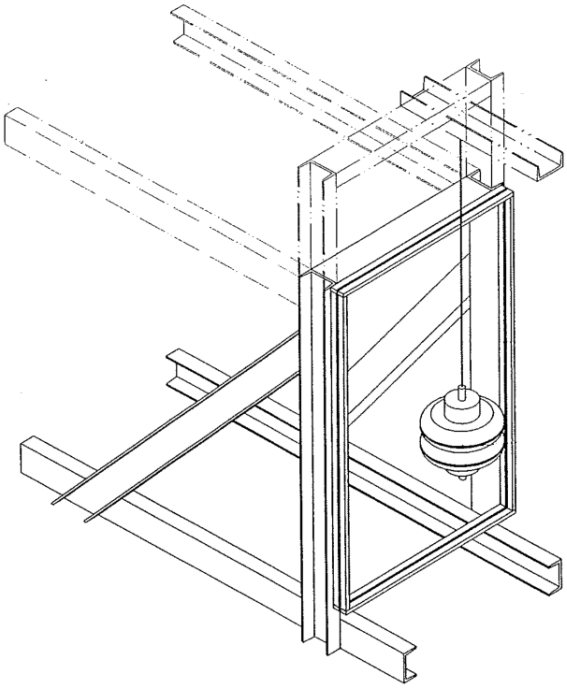

Figure 1.1: The 50 kg pendulum test used in European Standard EN 12600. A weight surrounded by two inflated tires is dropped from different heights on a laminated glass plate [2].

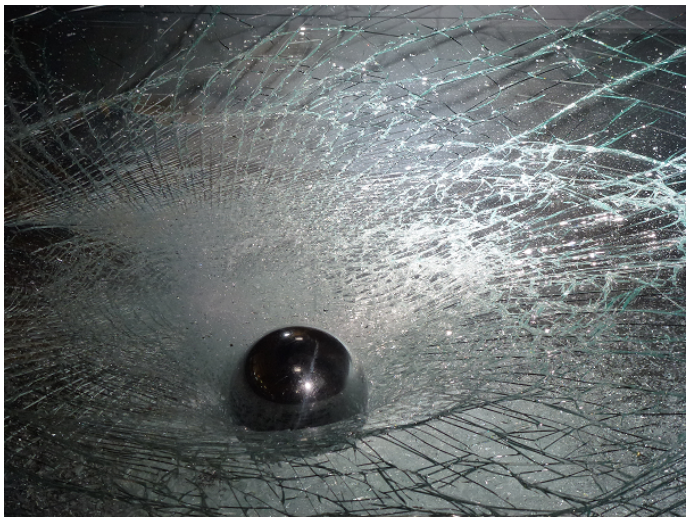

Figure 1.2: A 4 kg ball test used in European Standard EN 356. The ball is dropped three times on the glass which has to sustain the impacts [3].

A similar drop test is done with laminated glass used for windshields (ECE R43) in which a smaller steel ball modeling a small rock hitting the windshield is dropped from different heights onto a smaller piece of laminated glass. The glass has also to prevent the penetration of the ball but also it must show limited shattering or glass. This test is performed at -20 °C, 20 °C and 50 °C as the windshield might be subjected to various temperature conditions.

It can be seen that even if a lot of care is put into these tests in terms of controlled environments and testing procedures, these tests remain qualitative. In case the glass fails to pass one of these tests, it is difficult to identify the origin of the problem. Moreover, it is difficult to predict the behavior of a glass before it is tested in these specific conditions. This means that in order to develop new products a lot of trials in large dimensions have to be made.

1.2.2 Kinematics of impact on laminated glass

From these tests, a first picture of what is happening during an impact can be drawn. During the ball drop standard test for example, the highly complex process of the impact can be divided into different stages as described in Figure 1.3. Three main steps might be considered:

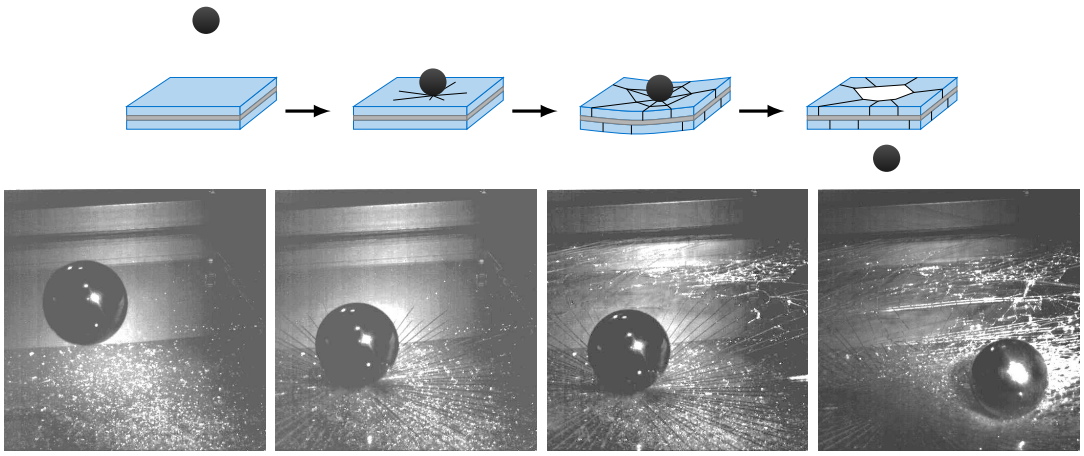

Figure 1.3: Schematic view a ball drop test impact and corresponding high speed camera frames.

- In a first step the impacting object hits the glass. This step lasts for a few tens of microseconds during which the cracks propagate towards the sample edges. The crack propagation velocity might be affected by the interlayer but it will

be of the order of magnitude of the Raleigh wave speed in glass ($5000\,\mathrm{m\,s^{-1}}$). During this step the whole plate can be considered as rigid as it does not show yet a large bending.

- In a second time ($>100\,\mu\mathrm{s}$), the glass plate undergoes a large bending. The plate reaches a maximal bending of about 10 cm after 1 s. Broken parts of glass are still holding on the interlayer and are pulled apart from each other due to the plate bending. Meanwhile, the interlayer delaminates from the glass and is stretched in between the glass parts.

- In the final stage of the impact, the main questions are the following: is the impacting object going through the glass? Is the object bouncing back the glass? Are large parts of glass detaching from the glass? Does the glass pass the standard test? These are questions of industrial relevance.

Basic understanding

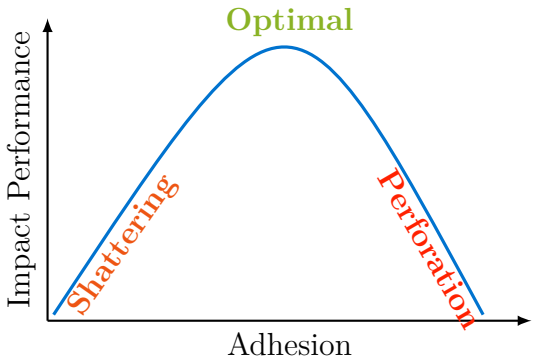

Figure 1.4: A balance in the interlayer/glass adhesion is required to reach good impact performances.

A first understanding of the problem arises from the facts that the impacting object should not perforate the glass and that no large glass part should detach from the structure. As underlined by [4], the adhesion between the glass and the polymeric interlayer must be balanced (Figure 1.4). Indeed, if the glass and the interlayer are too tightly bonded together the impacting object will go through the structure as if there was no interlayer. On the contrary, if adhesion is too low, the broken glass parts will be ejected from the structure. There is a generally admitted understanding that the impact energy is not dissipated, in these both extreme cases because the interlayer can not be stretched in both situations.

First results: order of magnitude

Beyond this very basic understanding of the problem, several works have already focused on the resistance of laminated glass to impact. It is difficult, during a real impact or a standard impact test, to implement measurements of plate deflection or of interlayer delamination, because of the speed of the impacting object (about $10\,\mathrm{m\,s^{-1}}$) and because of the complex and not predictable crack pattern. That is why smaller impact tests or bending experiments have been implemented to give a feeling of the processes at work during rupture. We can draw from these simpler experiments some orders of magnitude for the delamination of the interlayer and bending of the glass plate.

Delamination length: On a laminated glass in which a single crack has been propagated into the glass on each side, a small delamination of the interlayer can be observed on each part of the crack even if there was little bending (about 1 mm) applied on the glass to propagate the cracks (Figure 1.5). The delamination length in this case is about 0.2 mm.

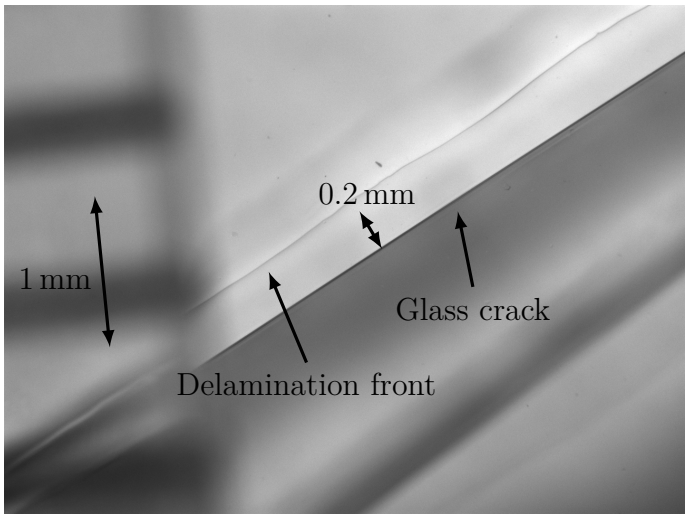

Figure 1.5: Delamination front and glass crack after propagation by undergoing a 1 mm bending. This image was taken under a microscope on a broken laminated glass sample. Here, the focus is made at one of the PVB glass interfaces close to the crack that has been propagated in the glass.

Small impact test: Information can also be derived from small impact tests such as order of magnitude of the time and space scales involved during the impact. In this experiment square plates of laminated glass of about 10 cm width were used.

The broken laminated glass plate can be considered as a two piece laminated glass bridged by a stretched interlayer as in Figure 1.6. The plate maximal bending is about 10 mm. If 200 µm of interlayer is delaminated, then the interlayer is stretched up to 500 µm which corresponds to a strain of 150%. From this it appears that large strain behavior of the interlayer has to be considered in this problem. The impact speed is close to $10\,\mathrm{mm\,s^{-1}}$ and thus the traction speed on the interlayer is about $500\,\mathrm{mm\,s^{-1}}$. Similar order of magnitudes can be derived from what is happening during a standard ball drop test.

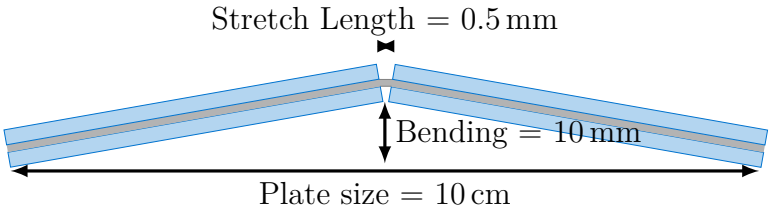

Figure 1.6: Schematic view of a bent and broken laminated glass.

1.2.3 Previous works on impact

More in depth studies on the impact resistance of laminated glass can be found in the literature.

The laminated glass is often considered as a sandwich object in which the interlayer/glass interface is supposed to be perfect. The laminated glass structure is thus considered as a sandwiched of two perfectly elastic plates with a viscoelastic layer in between and delamination is not taken into account. This approach is appropriate to model bending before rupture (large glass thickness or small impacting object velocities) or for constant loads (wind, snow, ...).

In his PhD conducted with Saint-Gobain, *Vidal* [5], has developed an analytical and a finite element model of the impact, based on beam and plate mechanics. The interlayer was described as a linear viscoelastic material. The purpose of this model is to predict glass rupture. *Vidal* was able to predict the experimental impact behavior of the laminated plate with both hard and soft impacting objects, before the glass rupture. The whole stress field, calculated by this finite element model, can then be used to predict the glass rupture. A statistical model is used to describe the rupture probability based on defects present in the glass.

Flocker has developed a similar description of the impact. In [6], he used a linear viscoelastic material to describe the interlayer and described the glass/interlayer

interface as perfect. The effect of different parameters on the laminated glass resistance to impact were studied: impacting object size, interlayer properties, thickness and boundary conditions. In particular, this work focused on the prediction of the maximal principal stresses.

Hooper has developed a finite element model of laminated glass using shell elements [7]. In a first step, the structure was modeled as a perfect laminate in order to study glass rupture. In a second step however, the stiffness of the broken glass elements was locally reduced to zero and a rate dependent plastic material was used to describe the interlayer. This work emphasized the fact that large dissipation occurs as soon as the interlayer delaminates from the glass and is stretched under impact loading. However, *Hooper* does not study the relationship between the mechanical behavior of the interlayer and the glass/polymer adhesion.

A different approach was considered by *Nourry* [8] and *Decourcelle* [9]. In both of these works the laminated glass was not considered as a perfect sandwich. These two works, conducted with Saint-Gobain, presented the stretching of the interlayer following its delamination from glass as the main source of dissipation. *Nourry* used a controlled perforation test to evaluate the amount of energy dissipated during the impact. In this test, the impacting object hits a glass (30 cm width) and is stopped after a certain distance of penetration. He showed, that almost 87% of the impact energy is dissipated during impact, after a 14 cm perforation (Figure 1.7).

Decourcelle pursued *Nourry*'s work and compared the results of the controlled perforation test with a standard ball drop test through the critical energy needed to perforate the laminated glass.

Chen et al. presented the interlayer as a polymer bridge between glass shatters [10] and [11]. In particular, they described the influence of the interlayer on crack propagation in the glass ply. Namely, the crack propagation velocity was reduced in the laminated glass compared to a simple monolithic glass under the same impact conditions.

1.3 Questions

As pointed out in many of the previous studies, for instance by *Nourry* [8], interlayer delamination and stretching is the main source of energy dissipation. As explained in 1.2.2, during impact, because of glass breakage and flexion of the overall structure, glass shatters go away from each other. In the process, the interlayer is delaminated

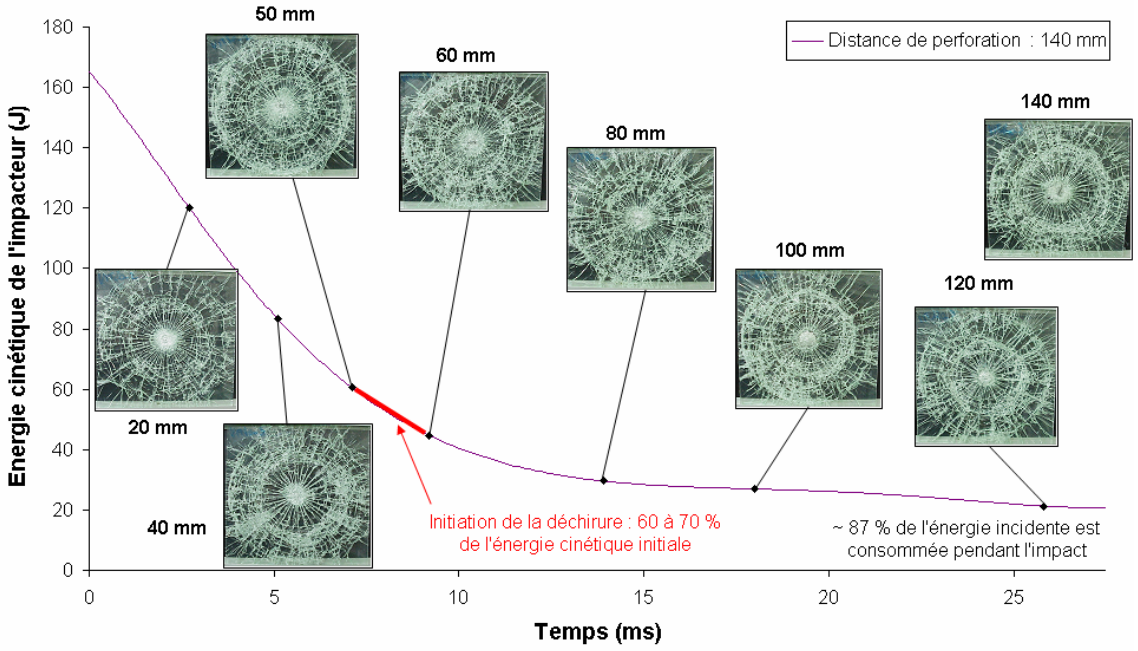

Figure 1.7: The kinetic energy of the impacting object is plotted as a function of time and perforation length. This test is conducted at 20 °C and the impacting object has a velocity of 9.2 m s^{-1} (Results from *Nourry*'s PhD thesis [8]).

from the glass. In between the delamination fronts, the polymer is stretched (Figure 1.8). Thus we decided to focus on this particular step of the impact.

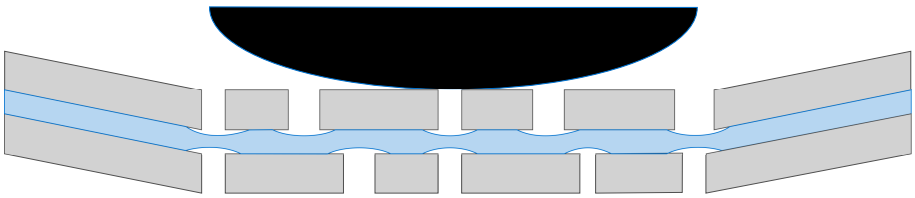

Figure 1.8: Following the impact, the bending of the plate drives glass shatters away from each other inducing stretching of the interlayer

Our main objective is to identify the main dissipation processes. We want to show that the basic understanding presented in 1.2.2 is correct and that the large amount of dissipated energy is the result of a balance in adhesion. Moreover, we will quantify the different mechanisms involved in the delamination and stretching of the interlayer during the impact.

During impact, due to the fast succession of events and to the complicated crack pattern, it is difficult to target specific dissipating mechanisms. Thus model experiments have been developed. *Seshadri and al.* have used such model experiments

to study the delamination and subsequent stretching of the interlayer. They used a Through Crack Tensile test (TCT test) to model these two phenomena [12]. This test presented more thoroughly in 2.5.2, consists in a uniaxial tension test on a laminated glass in which both glass sides are pre-cracked (Figure 1.9). It partially reproduces what is happening during the flexion step of the impact in between two glass parts.

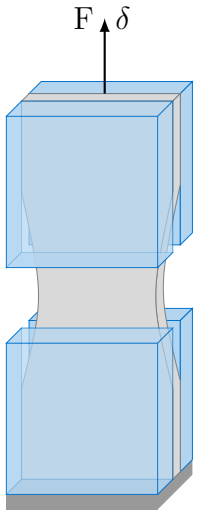

Figure 1.9: Schematic representation of the Through Crack Tensile Test sample. The delaminated part of the interlayer is stretched in between the delamination fronts.

This test combines the actions of the glass/interlayer interface and of the interlayer rheology.

Due to the key role of the interlayer, its rheology will be studied. It will provide a tool to analyze the delamination experiments that will be conducted in a second time. In this study, we will focus on:

- The rheology of the interlayer in both small and large strains.
- The amount of energy that the interlayer is dissipating.
- The relation between dissipation and polymer chemistry and structure.

Based on this understanding of PVB rheology and with the delamination experiment we will try to answer to the following problems:

- Can we quantify interlayer stretching and delamination velocity?
- How much energy is dissipated in this process?

- What is the impact of applied velocity and temperature?
- Can we identify distinct zones of dissipation?
- What is the effect of the level of adhesion?
- Can we provide a basic understanding and modeling of the delamination?
- And finally, what does that imply for the industrial application?

Chapter 2

Methods

In this chapter, the preparation of laminated glass samples will be shortly described. A method to modify the interlayer/glass interface thanks to silanization will be briefly presented. The different experimental methods (mechanical tests and optical measurement systems) used to characterize the interlayer behavior and the rupture of adhesion with the glass will be presented.

2.1 Laminated glass assembly

Laminated glass is generally composed of a layer of Poly(VinylButyral) sandwiched in between two glass plies. The glass used in this study is a Planiclear glass from Saint-Gobain with a 2 mm thickness. Laminated glass is assembled at Saint-Gobain Recherche. At the laboratory scale it is a one day process (Figure 2.1), which reproduces the industrial process. The glass is first cut using a glass cutter, then the glass edges are smoothed onto an abrasive band. The PVB interlayer is cut at the correct dimensions. Assembly is carried out in a clean room after washing the glass on both sides (industrial concentrated soap highly diluted in ultra pure water), carefully rinsing and drying the glass. The glass assembly is then put into a vacuum bag which is subjected to a heat and pressure treatment in an autoclave for 1.5 hour at 140 °C and 10 bar.

2.2 Silanization

For some experiments, the adhesion in laminated glass was modified by silanization of the glass surface. In order to obtain a stronger or a weaker adhesion two

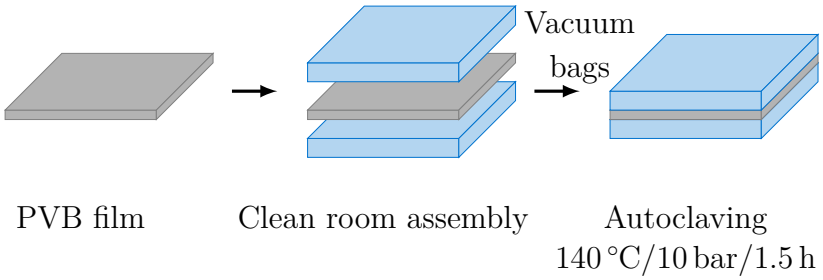

Figure 2.1: Schematic representation of laminated glass assembly at the laboratory scale

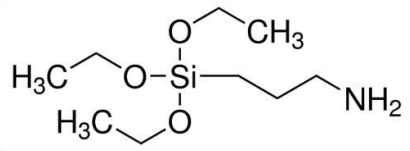

(a) APTS (3-Aminopropyl)triethoxysilane

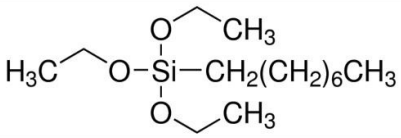

(b) OTES triethoxy(octyl)silane

Figure 2.2: The two silanes used for (a) enhancing and (b) reducing the adhesion between the glass and the PVB interlayer

silanes were used. (3-Aminopropyl) triethoxysilane (APTS) was used to enhance the adhesion while triethoxy(octyl)silane (OTES) was used to reduce it.

The silanes were applied by a wiping method. This method is not commonly used in academic research but has proved to be very reproducible. Moreover it is easily scalable to large samples such as the one used in the peel and TCT tests. A Cerox® solution was used to clean the glass. Cerox® is an abrasive powder which activates the glass surface by removing molecules already interacting with the glass silanols (light surface etching of the glass). After rinsing the glass surface with deionized water the silane solution previously prepared was applied on the cleaned surface.

The silane agents were pre-hydrolyzed. The silanes were deposited onto the glass with a cleanroom wiper. Finally, the treated glass was cleaned with a solvent solution.

More details about the silanization process can be found in the MS degree thesis of *Raphaelle Kulis* [13].

2.3 Mechanical behavior of the interlayer

The interlayer meachanical behavior was investigated in both the small strain and large strain regimes. The different devices and techniques used to conduct this study are presented here. Since the mechanical tests were done on a PVB as received and that the PVB in laminated glass is subjected to a heat and pressure treatment during the lamination process, we checked that the behavior in both small strain and large strain deformation are similar before and after lamination temperature and pressure treatment. Results can be found in Appendix A.

2.3.1 Dynamical Mechanical Analysis (DMA)

Mechanical response of polymers subjected to small oscillatory strain

When applying an oscillatory deformation on a viscoelastic sample at a given frequency ω ($\epsilon = \epsilon_0 \cos(\omega t)$) the response of the material is delayed in time. This delay δ characterizes the viscoelastic response of the material ($\sigma = \sigma_0 \cos(\omega t + \delta)$). One can then define a complex modulus E^*. The real part E', is called the storage modulus and reflects the elastic storage of the energy. The imaginary part E'' is called the lost modulus and accounts for the viscoelastic losses. The ratio between these two moduli is often denoted $\tan\delta$ and it is a way to compare the stored versus lost energy during the deformation of the material. The stress is then given by $\sigma = E^*\epsilon$.

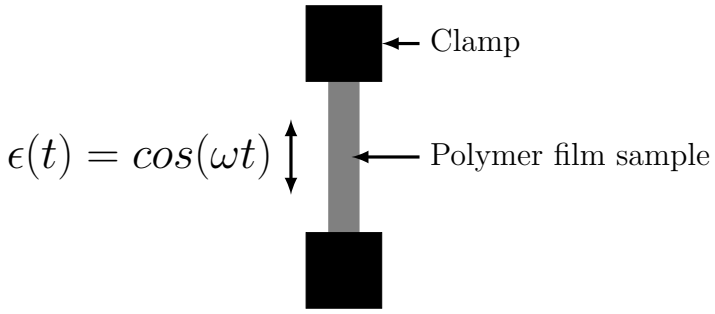

Figure 2.3: DMA experiment on a polymer film in uniaxial tension geometry. A sinusoidal strain is applied on the sample and a shifted sinusoidal stress is measured. Storage and loss moduli are extracted from there.

In polymers, a relation between time and temperature dependence of E^* can often be found. Thus the high temperature behavior corresponds to the behavior at low frequency or at long time. Similarly, the behavior at low temperature corresponds to the behavior at high frequency or at short time. This relation between time and temperature is often used to build master curves of the mechanical be-

havior of the polymer (storage and loss moduli) from experiments made at different frequencies or temperatures. This enables, in the end, to get data on a much larger range of temperatures and frequencies. The shift factors on the frequency axis (usually called a_T) for each curves follow specific laws that enable to predict the behavior at higher or lower temperature or frequency. These coefficients are defined as the ratio between the frequency at temperature T and the frequency at the reference temperature T_{ref} (equation 2.3.1).

$$a_T = \frac{\omega_T}{\omega_{T_{ref}}} \tag{2.3.1}$$

Thanks to these shifting coefficients, the storage modulus $E(\omega, T)$ at frequency ω and temperature T can be shifted at the corresponding frequency ω' for the reference temperature T_{ref} with the relation of equation 2.3.2.

$$E(\omega, T) = E(\omega_{T_{ref}}, T_{ref}) = E(\omega/a_T, T_{ref}) \tag{2.3.2}$$

The Arrhenius law is a first example of shifting coefficient law (equation 2.3.3). In this equation R is the universal gas constant and E_a is an activation energy. This type of law can be used for example to describe hydrogen bond dynamics.

$$\ln(a_T) = \frac{E_a}{R}(\frac{1}{T} - \frac{T}{T_{ref}}) \tag{2.3.3}$$

William, Landel and Ferry [14] have shown that in the case of polymers, the time dependence and the temperature dependence are related through the so called WLF law which gives shifting coefficient a_T linking time to temperature at a given reference temperature as:

$$\log(a_T) = \frac{-C_1(T - T_{ref})}{C_2 + T - T_{ref}} \tag{2.3.4}$$

This equation is a semi-empirical relation that *Wiliam et al.* have found from experiments on different polymers. C_1 and C_2 are often said to be universal coefficients. Typical values of these coefficients are $C_1 = 17.4$ and $C_2 = 51.6$°C. However these values do not apply to many other polymers.

Experimental setup

Dynamic mechanical analysis was conducted on a TA Instruments Q800 apparatus. As PVB is a soft thin film, the tension geometry was used (Figure 2.3). Small pieces of precise dimension around 15 mm length and 10 mm width were used. A preload

of 0.01 N is applied to have a straight sample between clamps and prevent buckling due to clamping.

The linear regime extends at least up to 0.5%. In order to always be in the linear regime of strain and to remain at low stresses, the strain in DMA measurements will be kept at a value of 0.01% which will also be used in the rheometer (in which higher strains will induce stresses out of the scope of the rheometer, even at room temperature).

2.3.2 Rheology

DMA measurements can only cover a temperature range over which the material is solid and does not flow. In our case the glass transition temperature being around 25 °C to 35 °C, measurements above 60 °C could not be made and results between 40 °C and 60 °C have to be regarded with great care as they might be subjected to large deviation. In order to compare polymers in a temperature range above the glass transition a rheometer with a parallel plates geometry was used.

The apparatus is an Anton-Paar rheometer (Physica MCR 501). The parallel plates geometry used was made of a small bucket of 5 cm diameter to contain the sample and a disk of the same diameter to apply a controlled oscillatory deformation. In order to get a good measurement three layers of polymer were put inside the small bucket which was used as a mold and kept at 160 °C during 30 min before measurement. The melted layers of polymer then form a single volume of material thick enough to have a measurable value of stress.

Contact between the upper plate of the geometry of the rheometer and the sample was kept by imposing the normal forces to be zero at all time during the experiment (so that contact is not lost if the sample shrinks). The temperature range was 40 °C to 160 °C with 5 °C steps. At each temperature step, a frequency range from 0.1 Hz to 10 Hz was covered. Before doing any measurement the temperature was kept constant (with a precision of 0.2 °C) during at least 10 min.

2.3.3 Uniaxial tension

Uniaxial tension experiments were conducted on a Zwick (Hamsler HC25) hydraulic machine. A force cell of 1 kN was used. Displacements were measured thanks to both the clamp displacement and a video camera Baumer BM20. In order to control the temperature a closed cabinet was used around the clamps. Cooling was obtained by liquid nitrogen and heating by an electric resistance. Thanks to a PID ther-

moregulator 2216L from Eurother Automation, the temperature was kept constant close to a user defined temperature. The homogeneity of the temperature inside the cabinet was checked several times in different places of the cabinet. Humidity was not controlled and it was assumed to be identical to the ambient humidity (in a range from 20 to 50 HR).

Low force measurements were conducted on an Instron machine (Instron 5565) with a load cell of 100 N. Temperature was controlled in a closed cabinet using a 2216L Eurother Automation thermoregulator. Displacement was monitored with a video extensometer: two white dots are placed on the sample and followed automatically by the extensometer.

The tests were conducted at controlled displacement rate on shouldered test bars of controlled dimensions (Figure 2.4).

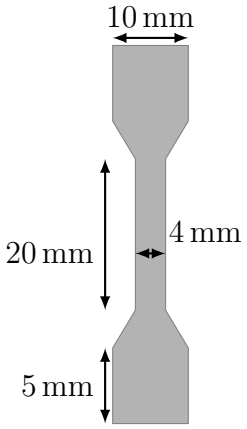

Figure 2.4: Uniaxial tension sample shape

2.4 Different models to describe the constitutive behavior of the interlayer

The complex behavior of the interlayer described later in Chapter 3, is difficult to model as it displays simultaneously a viscoelastic behavior, a hyperelastic behavior and a plastic behavior. We choose to use a Generalized Maxwell description for the viscoelastic part [15] through a Prony's serie. It will model the time and temperature dependence of the material. As the polymer is subjected to large strain, linear elasticity is no longer adapted. The hyperelastic model will also have to take into account of the hardening of the material at really high strains. Thus an Arruda-Boyce model will be used [16]. These different models are described here.

2.4.1 Small strain description: Generalized Maxwell model

In order to model the small strain behavior one can use a generalized Maxwell model and the associated Prony's serie. In this model (Figure 2.5), the material is described by dashpots to represent elastic relaxation with different characteristic times (τ_i) of the material and the associated elasticity with springs (E_i). The springs and dashpots are associated in series for each characteristic time. All the branches are in parallel. A final spring is associated in parallel with these dissipative branches to represent the long term elasticity (E_∞).

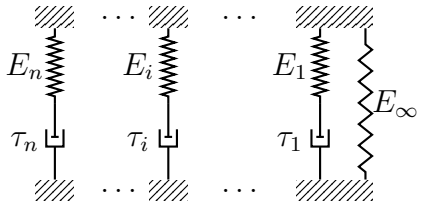

Figure 2.5: The generalized Maxwell rheological model

The global time dependent moduli describing the generalized Maxwell rheological model can be written either in a time or frequency base. In the time base, the relaxation function of the Young modulus can be written as a Prony's serie:

$$E(t) = E_\infty + \sum_{i=1}^{N} E_i . \exp(-t/\tau_i) \tag{2.4.1}$$

In the frequency base the Young modulus can be decomposed in the storage and loss components. In order to do so we will define the instantaneous modulus E_0 which is given by $E_0 = E_\infty + \sum_{i=1}^{N} E_i$ which corresponds to immediate response of the material. The coefficient a_i are also defined as $a_i = E_i/E_0$. Finally the frequency base storage and loss moduli can be defined by the following expressions:

$$\begin{aligned} E'(\omega) &= E_\infty + E_0 \sum_{i=1}^{N} \frac{a_i \tau_i^2 \omega^2}{1 + \tau_i^2 \omega^2} \\ E''(\omega) &= E_\infty + E_0 \sum_{i=1}^{N} \frac{a_i \tau_i \omega}{1 + \tau_i^2 \omega^2} \end{aligned} \tag{2.4.2}$$

2.4.2 Hyperelasticity: Arruda-Boyce model

The Arruda-Boyce model is used to model large strain hyperelasticity including the strain hardening displayed at very large strains. This model is based on a statistical

description of the polymer network. In a uniaxial tension test on an incompressible material, the stress expression is the following:

$$\sigma = 2\mu\left(\lambda - \frac{1}{\lambda^2}\right)\sum_{i=1}^{5}\frac{iC_i I_1^{i-1}}{\lambda_m^{2(i-1)}} \tag{2.4.3}$$

where μ is the shear modulus, λ is the stretch applied on the material and I_1 is the first invariant $I_1 = \lambda_1^2 + \lambda_2^2 + \lambda_3^2$. The C_i are the coefficients of the Langevin function: $C_1 = 1/2$, $C_2 = 1/20$, $C_3 = 11/1050$, $C_4 = 19/7000$ and $C_5 = 519/673750$. λ_m is the maximal chain extensibility. A compilation of several results found in the literature are put together in Appendix B to explain this expression.

2.5 Delamination experiments on laminated glass

2.5.1 Peel test

In order to assess the adhesive properties of the interlayer on the glass, some peel experiments were conducted by *Raphaelle Kulis* [13] during her internship. Special peel samples were prepared. A glass of 5 cm width, 15 cm length and 2 mm thickness were used. The interlayer assembled with the glass was 2 cm width, 20 cm length and 0.76 mm thickness.

The assembly (Figure 2.6) was made as for a classical laminated glass (cleaning and assembly in clean room) but instead of applying a second glass on top of the interlayer a cloth backing was put above the interlayer. A small part of the bottom glass was also covered with Kapton® to make the peeling initiation easier.

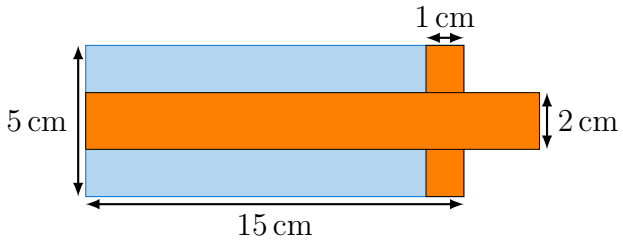

(a) Top view

Figure 2.6: Laminated assembly for peel test [13].

The peel sample was then cured in the autoclave using the standard procedure for laminated glass.

The peel sample was tested on a Zwick Z010 testing machine with a 1 kN load cell. The peeling occurs at 90°. The laminated peel sample is put on rolls which

transform the vertical motion of the upper clamp into a horizontal sliding of the glass (Figure 2.7). The peel angle is constant through the test. The displacement speed is controlled.

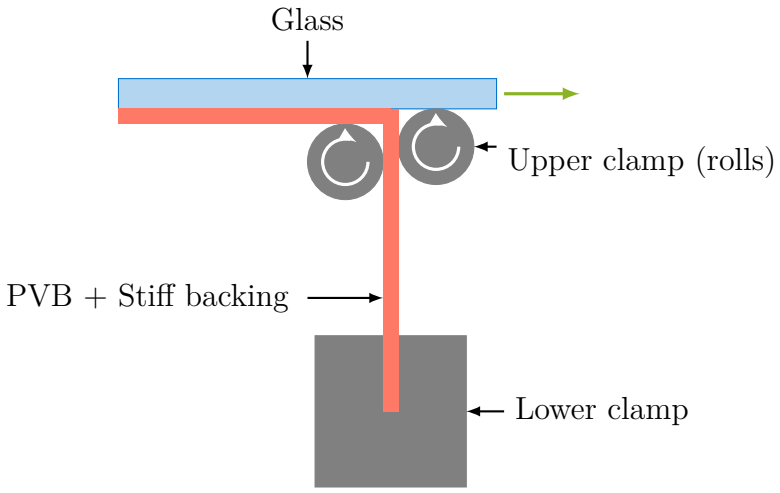

Figure 2.7: Schematic view of the peel setup. Two rolls enable the peel angle to be kept constant through the test equal to 90° [13].

2.5.2 Through crack tensile test

The through crack tensile test is a uniaxial tension test made on a pre-cracked laminated glass (Figure 2.8). The test is conducted on a Zwick Hamsler HC25 hydraulic machine with a 10 kN load cell. The laminated glass sample used for this experiment has a 5 cm width and a 10 cm length. The two glass panes are 2 mm thick and the interlayer thickness is most of the time 0.76 mm. Just before the TCT experiment, the two glasses are cut in their middle through their width. A first scratch is made on the glass along its width thanks to a diamond cutting wheel. Then the laminated sample is subjected to very small bending in order to propagate the crack. The sample is then mounted in the tensile rig and a pressure of 8 MPa is applied in-between the clamps to avoid any sliding of the sample. Finally the cracked laminated glass is subjected to a uniaxial tension experiment. During the experiment, the upper clamp velocity is controlled and the bottom glass is fixed. The interlayer is delaminating from the glass and stretched. The position of the delamination fronts is measured with a Baumer BM20 camera. The environment is controlled as in 2.3.3.

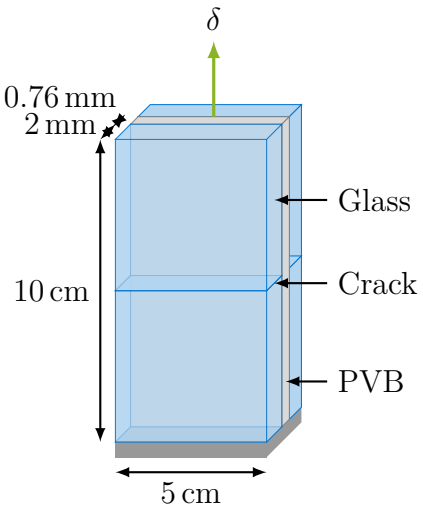

Figure 2.8: Schematic representation of the Through Crack Tensile Test sample. During the test, the displacement δ and the associated velocity $\dot{\delta}$ are controlled.

2.6 Optical methods

2.6.1 Video acquisition

Video acquisition for displacement measurements were conducted with a Baumer BM20 industrial camera. As there was no software to enable movie acquisition a small acquisition software was developed with Matlab. Matlab Video Acquisition toolbox was used to acquire the images and to control the camera. A gui was setup to enable a better usability by other users. The software has been packaged with Matlab App Tools and is available at this address:

`http://www.mathworks.com/matlabcentral/fileexchange/46879-gigeacq-m`

This code is free to use and to distribute under BSD licensing. The code uses two functions provided by Mathwork Central named CalculateFrameRate and CalculatePacketDelay which can be found here:

`http://www.mathworks.com/matlabcentral/answers/uploaded_files/6148/CalculateFrameRate.m`

and there

`http://www.mathworks.com/matlabcentral/answers/uploaded_files/1061/CalculatePacketDelay.m`

A Photon Mini UX100 fastcamera was also used for digital image correlation measurements and for sensitivity purpose in the photoelastic measurements.

2.6.2 Digital image correlation

Digital image correlation was sometimes applied to the TCT test. Ink was sprayed on one side of the PVB interlayer. A second interlayer film was added on top of the first one (Figure 2.9). Thus, the ink was not in contact with the glass to prevent a change in adhesion. Moreover, as the dots are on the middle plane they did not get out of the focal plane during the experiment.

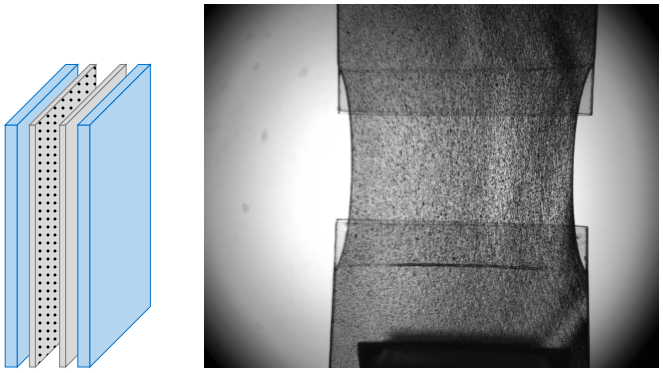

Figure 2.9: Schematic view of the digital image correlation sample (left) and experiment (right). Paint dots are randomly spread to obtain a speckle, in the middle plane of the PVB layer.

The image acquisition focused on a small area on the bottom glass (which is fixed during the experiment 2.5.2). A long range microscope from Questar (Questar Q100) was used.

During the experiment (Figure 2.10) displacements were measured along a vertical line (white line). These displacements are corrected by the average displacement of some points which are supposed to be fixed (white square). This will subtract the rigid body displacement due to unwanted movements of the machine during the test. At some point of the experiment, these reference points start to move and they can no longer be used as reference to correct the machine displacements. Thus a mean value of their displacements during the last 10 frames are used to evaluate future corrections. At the end of the experiment these corrections are less important as the machine displacements are less pronounced.

2.6.3 Photoelasticity

Photoelastic measurements were conducted on both laminated glass samples during the TCT test and the uniaxial tension of the interlayer alone. Two cross polarizers and two quarter wave plates were placed around the sample as described on Figure

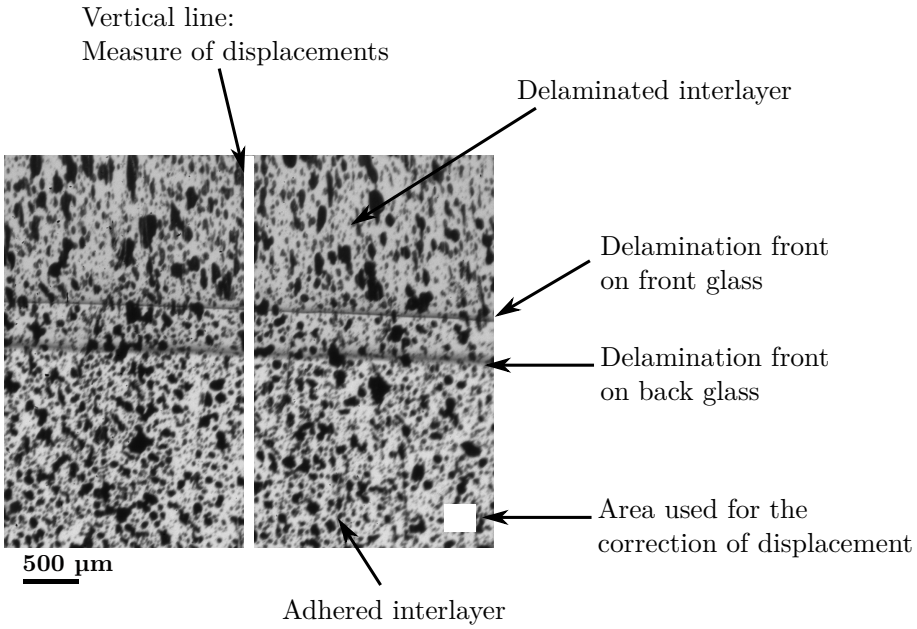

Figure 2.10: Digital image correlation frame. The displacements measured on the vertical white line are corrected by the displacements (supposed to be due to experimental noise) of the white region out of the delaminated area.

2.11. The first polarizer is simply called the polarizer while the second one is referred to as the analyzer.

Some materials exhibit an anisotropy of the refractive indices. These materials are called birefringent. As the optical properties of the material are related to their molecular organization (in particular in polymers to chain alignment), birefringence appears when a stretch is applied to a transparent material.

A simple way to visualize this birefringence is to illuminate with a white light and to put a polarizer and an analyzer on each part of the sample. If the principal optical directions of the polarizer and of the analyzer are crossed at 90° from each

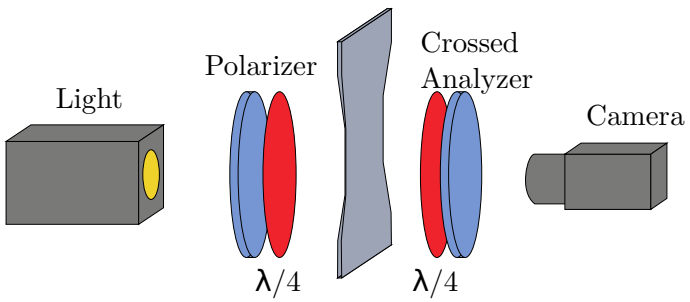

Figure 2.11: Photoelasticity measurement: two cross polarizers and two quarter wave plates were placed around a PVB uniaxial tension sample or laminated glass TCT test sample.

other, one can observe two things (Figure 2.12):

- Some completely dark bands called isoclinic bands
- Some colored bands called isochromatic bands

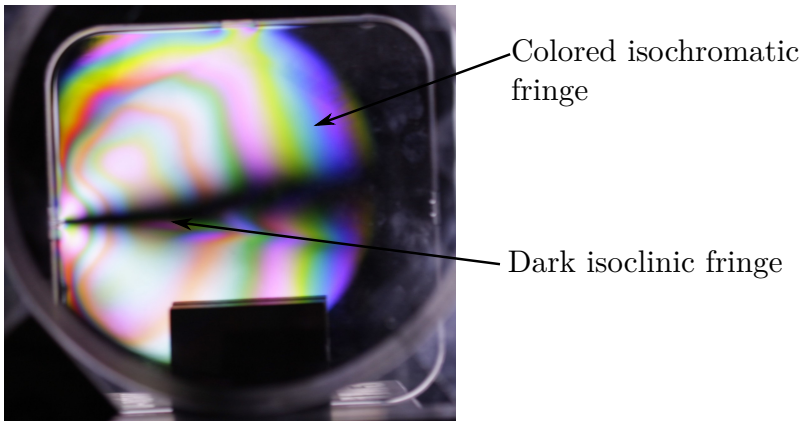

Figure 2.12: A photoelastic pattern observed on a PMMA sample in-between cross polarizers in white light. One isoclinic dark line goes through the sample indicating the principal stress direction. The isochromatic colored bands are regions of identical chain alignment.

The isoclinic bands correspond to the part of the sample where the stretch is aligned with the polarizer and thus polarized light is completely cut off by the analyzer (no matter the wavelength). These bands will be parallel to the principal strain or stress directions. If the crossed polarizer/analyzer are rotated, the position of these line will change. The isochromatic bands corresponds to regions over which the light phase was shifted from a multiplicity of the light time period. For each wavelength, the refraction will be different and one observes a color pattern. Each color bands corresponds to an area where there is an equal amplitude of chain alignment or local strain. Unlike isoclinic bands, the isochromatic bands do not depend on the polarizer/analyzer orientation. Quarter wave plates are used in order to get a circular light polarization. This will remove the isoclinic fringes which do not bring much as the principal stress directions are well known in the uniaxial tension tests that we are conducting. Moreover, monochromatic light is used to only get variation of the light intensity over the sample. The areas with the same intensity present the same amplitude of chain alignment.

In the case of a monochromatic light (wavelength λ_0, the Gaussian network theory description of photoelasticity described by *Treloar* ([17]) gives the intensity variation as a function of the stretch applied to the sample:

$$I \propto \cos^2\left[\frac{2C\pi(n_1 - n_2)t}{\lambda_0}\right] \approx \cos^2\left[\frac{2C'\pi(\sigma_1 - \sigma_2)t}{\lambda_0}\right] \tag{2.6.1}$$

where n_1 and n_2 are the principal optical coefficient, and σ_1 and σ_2 are the corresponding principal stresses. C and C' are constants related to the network properties. t is the interlayer thickness which also changes during the test and that has to be accounted for. In the case of an incompressible material subjected to uniaxial tension this expression leads to:

$$I \propto cos^2\left[\frac{2C'\pi(\lambda^2 - \frac{1}{\lambda})t}{\lambda_0}\right] \tag{2.6.2}$$

Finally, we can get from this equation that a complete light extinction will be observed periodically. The order of the extinction or birefringent order is given by:

$$N = \frac{C(\lambda^2 - \frac{1}{\lambda})}{\lambda_0}t \tag{2.6.3}$$

2.7 Differential Scanning Calorimetry

Differential Scanning Calorimetry experiments were conducted on Q200 apparatus from TA-Instruments in an hermetically closed aluminum pane. Measurements are done with a nitrogen flow of $50\,\mathrm{mm\,min^{-1}}$.

2.8 X-ray scattering

Small angle X-ray scattering experiments were conducted for us by *Quentin Demassieux*. Shouldered test bar samples with an effective length of 20 mm were used. The tests were conducted at the Advanced Photon Source (Argonne National Laboratory) 5ID-D, B run beam. During the scattering exeperiments, the sample was loaded with a Linkam TST350 device which is composed of a traction machine enclosed in a oven equipped with a heating element in contact with the sample to control the temperature. The heating element is transparent to X-rays. The displacement was only measured thanks to clamp displacement as no images could be taken during the test. Samples were subjected to a uniaxial tension at a strain rate of $0.01\,\mathrm{s^{-1}}$. X-ray scattering was recorded during this time. Only SAXS results will be presented here.

The 5ID-D Run B beam has the following properties:

Energy (keV)	Wavelength (nm)	SAXS distance (m)	SAXS range Q (nm^{-1})
9.8	0.127	8.505	0.013–0.78

Table 2.1: Parameters of the beam and detector for the 5ID-D Run B beam.

Chapter 3

A complex structure and rheology

3.1 Introduction

The relationship between the mechanical behavior of the interlayer and its chemical structure is of prime interest in order to understand the dissipation mechanisms occurring during impact. Indeed, the delaminated part of the interlayer will be subjected to large stretch at various strain rates. We will first present here the chemistry of the PVB interlayer. Then the small strain mechanical response of the interlayer is investigated to characterize its time and temperature dependence. The large strain uniaxial cyclic tests provide a better understanding of the dissipation mechanisms at different strain rates and temperatures. Since during the delamination, the interlayer is subjected to a large level of strain, it is necessary to investigate both regimes to build a proper description of the interlayer behavior. Finally, photoelastic measurements will help us to link these dissipation processes to the chemical structure of the interlayer through a simple rheological model.

3.2 Poly(Vinyl Butyral) interlayer

3.2.1 Chemistry

PVB is a random polymer chain made of three monomers (Figure 3.1). The synthesis process goes through three main steps [18]. The first one is the polymerization of vinylacetate in a chain of poly(vinylacetate). This chain is then hydrolyzed which leads to the formation of poly(vinylalcohol). Poly(vinylalcohol) finally reacts with butyraldehyde to form butyral cycles. The final composition of the chain which presents the optimal adhesion and mechanical properties is close to 1 or 2 wt% of

acetate groups, 18 wt% of alcohol groups and 80 wt% of butyral cycles.

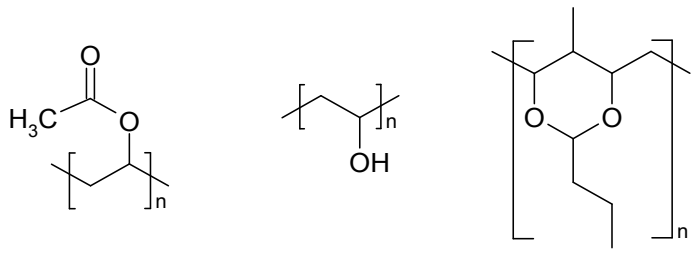

Vinylacetate Vinylalcohol Vinylbutyral

Figure 3.1: The three monomers found in the PVB structure.

The polymer weight found from Size Extrusion Chromatography is of 197 kg mol^{-1} (relative to polystyrene calibration) with a polydispersity index of 1.42.

The industrial product contains also a plasticizing agent which is expected to decrease the glass transition temperature of the polymer from 70 °C to close to ambient temperature. The plasticizer is generally triethylene glycol di-(2-ethylhexanoate) (Figure 3.2). The amount of plasticizer is up to 20wt% leading to a glass transition temperature around 25 °C to 30 °C.

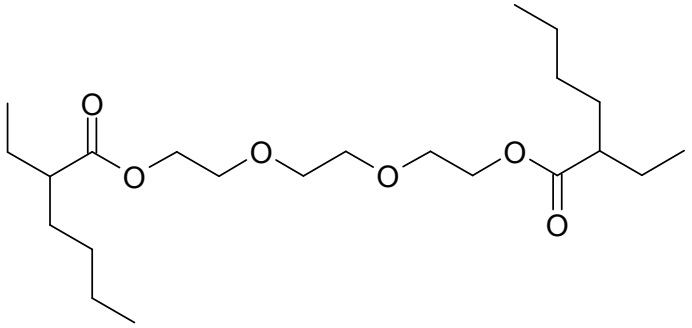

Triethylene glycol bis(2-ethylhexanoate)

Figure 3.2: Plasticizer molecule.

3.2.2 Hydroxyl groups

This polymer contains a certain amount of hydroxyl (OH) groups that are available for bonding to the glass but also for forming inter-chain bonds. Polarized hydrogen atoms are linked to a more electronegative atom such as oxygen. In the case of PVB it can be an hydrogen on the vinylalcohol group, the silanol group at the glass surface or any other OH group. Hydrogen bonds form between this polarized hydrogen and an electronegative atom which can be here the acetate group. This interaction has a

strength around $10\,\mathrm{kJ\,mol^{-1}}$ which has to be compared to the covalent bond which has an energy $> 100\,\mathrm{kJ\,mol^{-1}}$ and the Van der Waals interaction which has an energy around $1\,\mathrm{kJ\,mol^{-1}}$. However, a large number of this relatively weak hydrogen bonds can form strong links. The number of hydroxyl groups and acetate groups are thus very important for the rheology and mechanical behavior of the polymer but also for the adhesion strength. The PVB reference which has been used during this work presents an amount of OH groups around 17-18wt% or 40mol%.

By changing the hydroxyl group content, both adhesion on glass and bulk materials properties are impacted. In previous works made in Saint-Gobain ([19] and [18]), a relationship between interlayer chemistry (and chemical structure) and its mechanical behavior has been studied. In particular it has been shown that the amount of hydroxyl bond has a strong influence on the mechanical behavior of the interlayer. For example Klock ([19]) has shown that the Young modulus of the PVB is strongly affected by the amount of hydroxyl groups (Figure 3.3). In this figure, the amount of hydroxyl groups varies between 40 mol% and 85 mol% and the young modulus increases from 1 MPa to 1 GPa. The plasticizer amount is fixed at 26 mol%. The polymer is going through the glass transition towards the glassy plateau as the amount of hydroxyl groups increases at constant temperature and constant plasticizer content. The hydroxyl group content is also changing adhesion properties. In Figure 3.4, the peeling energy is measured during a 90° peel test at $10\,\mathrm{mm\,min^{-1}}$, at room temperature and shows this large increase.

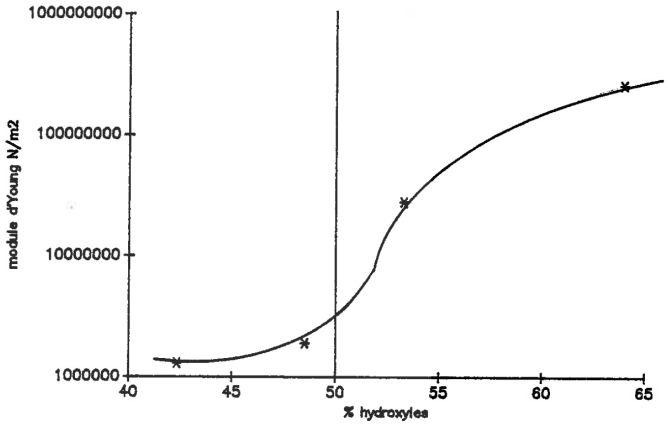

Figure 3.3: Young modulus as a function of the amount of OH groups. The OH groups content impacts the rheological properties of the material [19].

Mertz [18] has also shown that the hydroxyl groups form hydrogen bonds which break as the interlayer is stretched. Indeed he observed by FTIR that the ratio of free hydroxyl groups over hydroxyl groups forming hydrogen bonds, is decreasing as

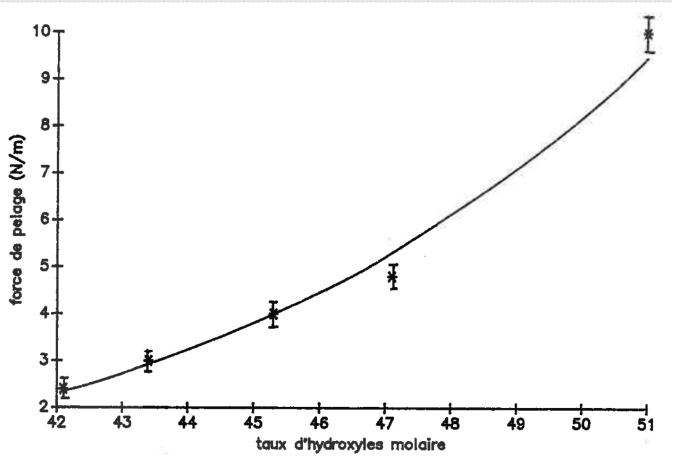

Figure 3.4: The peel energy as a function of the OH group amount. An increased value of the peeling energy is found for higher hydroxyl group content [19]. This increase is highly non linear.

the interlayer is stretched.

Finally, *Mertz* and *Klock* have shown a similar impact on the mechanical behavior of the amount of plasticizer. This plasticizer is supposed to prevent the formation of the hydrogen bonds in between the polymer chain by spacing the chains. Thus as the plasticizer amount increases, the interlayer becomes softer. For a plasticizer amount above 20 mol%, a PVB with a hydroxyl content of 43 mol% is in a rubbery state.

3.3 Rheology of the PVB

In order to study the mechanical behavior of the PVB interlayer, in both linear (small strain) and non-linear (large strain) regimes, rheology experiments (namely DMA and parallel plate rheometer) and uniaxial tension tests were conducted. *Hooper* made similar mechanical tests on the same PVB interlayer [20]. Others, used different PVB but provided complementary insight such as dynamic loading experiments at large strain [21] or large strain cyclic experiments [22]. In the next sections we present our own results which confirm the literature and also provide a new insight in the relationship between the mechanical behavior, the chemical structure and the energy dissipation in the PVB.

3.3.1 Small strain viscoelasticity

In order to investigate the small strain behavior of the interlayer and to get a proper description of the time dependence of its linear behavior, DMA and parallel plate rheology experiments were conducted. The DMA experiments measured the time and temperature dependence of the young modulus in a range of temperature from $-40\,°C$ to $60\,°C$. The rheometer experiments give the dependence on time and temperature of the shear modulus in the range of temperature from $40\,°C$ to $160\,°C$.

We also checked that the autoclaving process and the delamination from glass after the autoclave did not affect the interlayer behavior. Thus, the mechanical behavior of the interlayer can be measured on the PVB film as received (Appendix A).

Dynamical mechanical analysis

DMA experiments were conducted first at a frequency of $1\,Hz$ with a strain amplitude of 0.01%. Temperature increases from $-40\,°C$ to $80\,°C$ at a heating speed of $3\,°C\,min^{-1}$. The glass transition temperature of the plasticized PVB is around $30\,°C$ (Figure 3.5). To compare with other experiment it is important to note that the measured glass transition varies with the heating speed. The polymer displays a glassy behavior for temperatures lower than $20\,°C$. No clear value for the glassy storage modulus can be measured there, as it keeps increasing from $0.3\,GPa$ to $1\,GPa$ as the temperature decreases from $10\,°C$ to $-40\,°C$. On this plateau, the dissipation ratio is low as the loss modulus represents only 10% of the storage modulus. At temperatures higher than $50\,°C$, the polymer exhibits a rubbery behavior. The storage modulus drops to values ranging from $0.8\,MPa$ to $1\,MPa$. Again, the dissipation ratio is low in this regime, where the loss modulus represents only 10% to 20% of the storage modulus. However, during the glass transition, the dissipation ratio is maximal ($\tan(\delta)$ is higher than 1). There seems, as well, to be a slight increase of the dissipation at $70\,°C$ but as the DMA reaches its limits, the result has to be taken with caution.

As we are interested in the time dependence of the PVB behavior, the same DMA experiment is made at different temperatures from $-40\,°C$ to $60\,°C$ but for different oscillation frequencies. Each $5\,°C$, 5 frequencies per decades from $0.1\,Hz$ to $10\,Hz$ are tested (Figure 3.6(a)). Thanks to the time/temperature equivalence principle, a master curve can be obtained by shifting the different curves. A reference temperature of $20\,°C$ was used to build the curve.

In Figure 3.6(c), the storage, the loss and the dissipation ratio master curves are

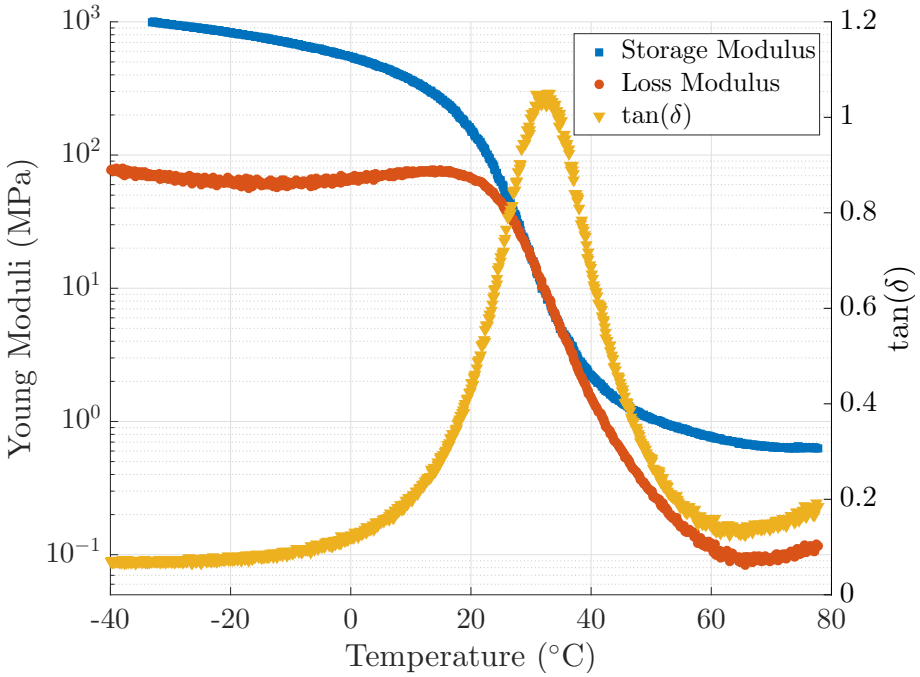

Figure 3.5: DMA experiment on PVB at 1 Hz and 0.01% deformation for temperature ranging from −40 °C to 80 °C.

plotted together. These results are similar to the one found by *Hooper* on the same interlayer [20].

The logarithmic values of the shift coefficients at this temperature can be plotted as a function of the inverse of the temperature (Figure 3.7). This can be used to extract WLF coefficients which are here $C_1 = 81$ and $C_2 = 417\,°C$.

If we want to expand our description of the time dependence of the PVB behavior at higher temperature, DMA is no longer suited as the polymer film becomes too soft and deforms under its own weight in the traction DMA setup. That is why a parallel plate rheometer was used to screen higher temperatures or longer time.

Parallel plate rheology at higher temperatures

Experiments were performed in the parallel plate geometry on three superimposed PVB films. At each 5 °C step for temperatures ranging from 35 °C to 160 °C, frequencies from 0.1 Hz to 10 Hz were screened. A master curve of the shear moduli can be built from these results (Figure 3.8) with a reference temperature of 40 °C and the coefficients are displayed in Figure 3.9. The time/temperature coefficients still follow a WLF law. However large vertical shift coefficients have to be applied away from the glass transition. The WLF coefficients for this master curve are $C_1 = 12$ and $C_2 = 74°C$.

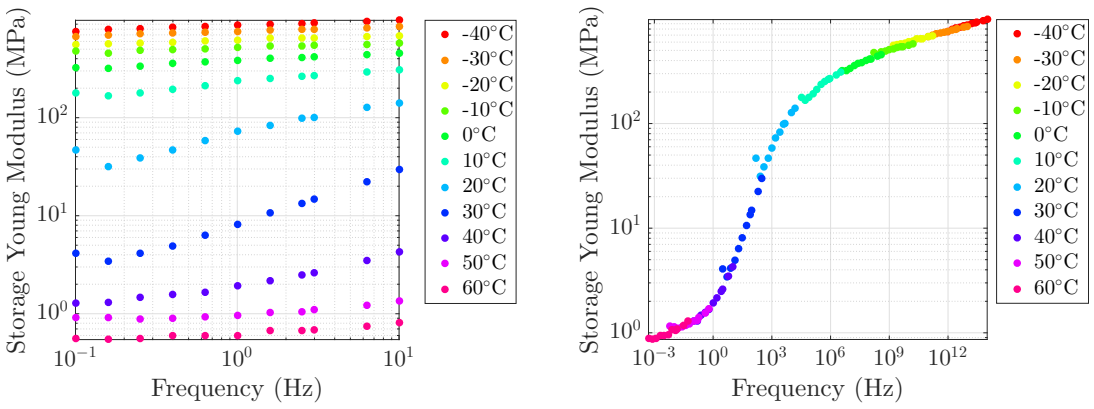

(a) Raw data

(b) Time/temperature superposition

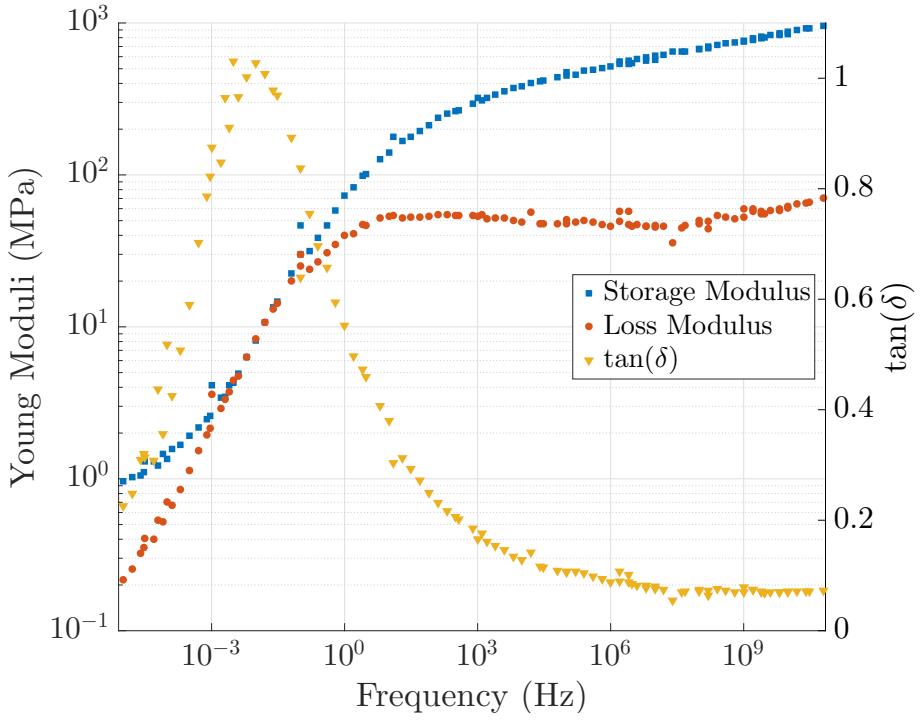

(c) Storage and loss young moduli with the dissipation ratio tanδ at 20 °C

Figure 3.6: DMA experiment on PVB for frequencies ranging from 0.01 Hz to 1 Hz, 0.01% deformation and for temperature ranging from −40 °C to 60 °C. In (a) the raw data concerning the storage modulus. In (b) the Time/Temperature superposition for the storage modulus. The reference temperature was set at 20 °C. In (c), the loss modulus and the dissipation ratio are added. Maximal dissipation occurs at the glass transition between 0.1 Hz and 1 Hz at this temperature.

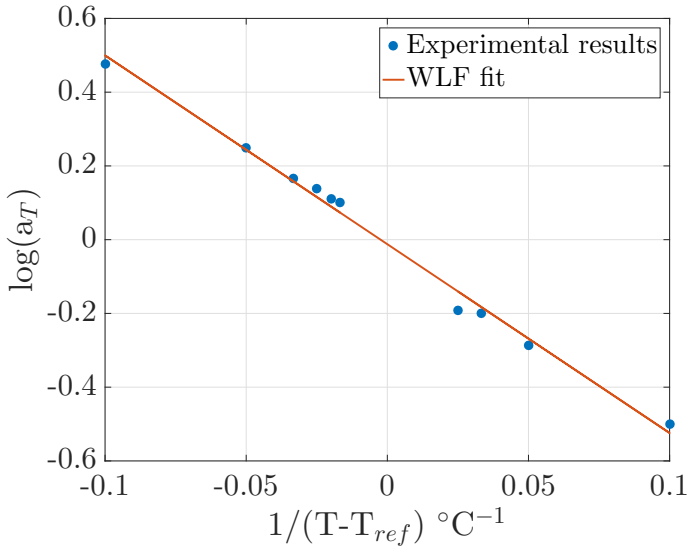

Figure 3.7: DMA shift coefficient at a reference temperature of 40 °C (blue) and WLF law fit with ($C_1 = 19$ and $C_2 = 143$ °C) (red).

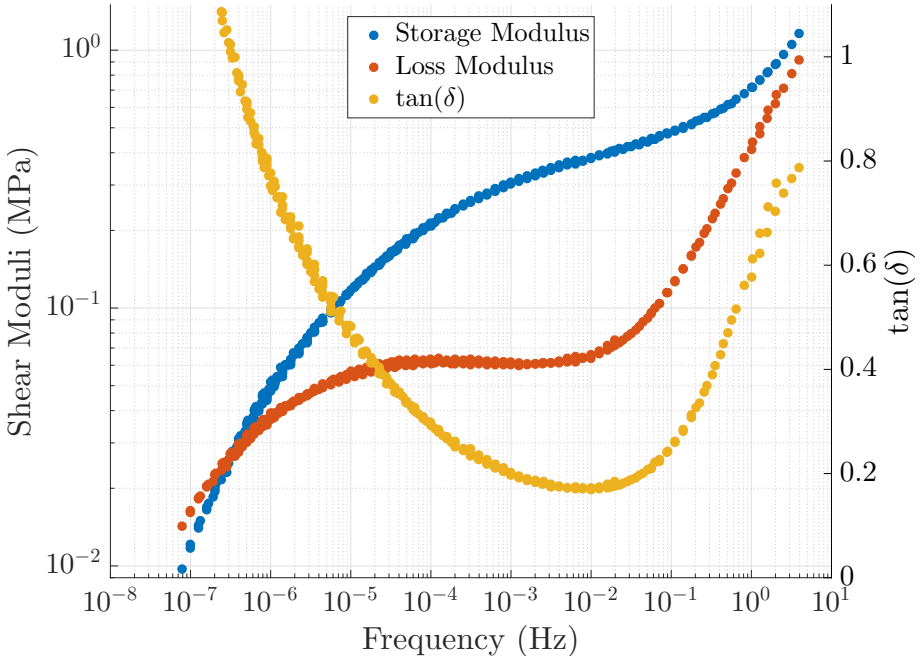

Figure 3.8: Rheometer shear modulus measurements in plane/plane geometry with 0.01% deformation, temperature ranges from 40 °C to 160 °C and frequency from 0.1 Hz to 1 Hz. Reference temperature is 40 °C.

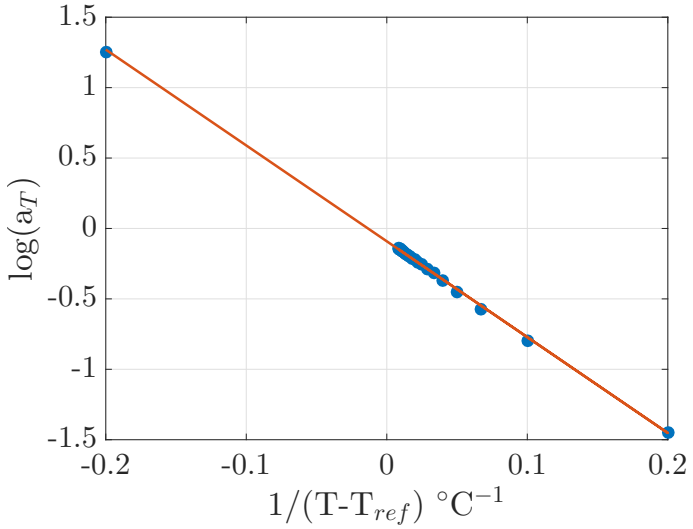

Figure 3.9: Rheometer experiment, shift coefficients following a WLF law for the master curve at 40 °C ($C_1 = 12$ and $C_2 = 74$ °C).

From a time/temperature master curve, the mass between entanglements can be deduced from the value of the storage modulus at the frequency corresponding to the minimum of the loss modulus curve, on the rubbery plateau. The relation between the mass between entanglements M_e and the storage modulus G' is given by:

$$G' = \frac{\rho RT}{M_e} \tag{3.3.1}$$

The material displays a rather large rubbery plateau from which we can extract an order of magnitude of the polymer chain length between entanglements: $M_e = 7\,\mathrm{kg\,mol^{-1}}$ which can be compared to the approximate total chain length $200\,\mathrm{kg\,mol^{-1}}$. This two values give 30 entanglements per chain. This is quite a high amount of entanglements which might also contribute to the difficulties encountered in the time/temperature superposition by the WLF law.

Complete description from -40 °C to 160 °C in small strain

The DMA and rheometer results can be combined in a single curve (Figure 3.10). As the rheometer gives shear modulus and the DMA gives a Young modulus, to combine the two curves, we had to assume that the material is incompressible so that $G = E/3$. As most of our experiments will be done at 20 °C we made this master curve at a reference temperature of 20 °C even if it is a little bit below the glass transition temperature. Note that this temperature is also out of the range

of the rheometer experiment. For the rheometer experiment alone the master curve was previously built at 40 °C and is now shifted at 20 °C for the superposition with DMA experiment.

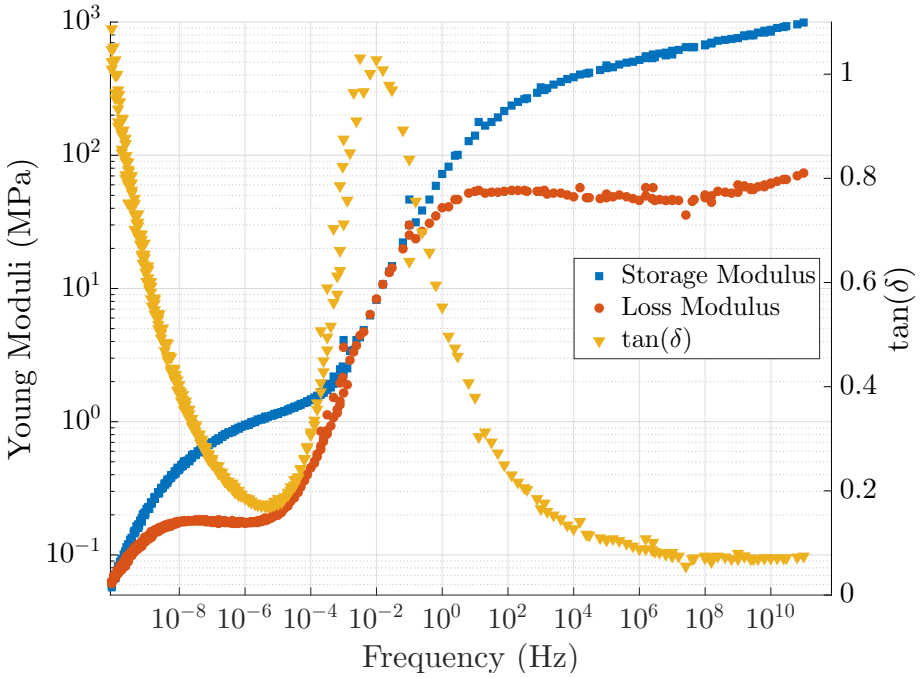

Figure 3.10: DMA and rheometer can be grouped to form a complete small strain description from the pHz to the THz. Reference temperature is 20 °C.

With a generalized Maxwell model, a numerical description of the previous master curves can be used to fit the experimental results (Figure 3.11). A 23 terms Prony series is used. The Prony series coefficients are also given in Table 3.1.

3.3.2 Large strain uniaxial tension

The small strain description of the interlayer behavior is not sufficient to describe the behavior during impact as the interlayer is deformed at strain higher than 100%. Large strain uniaxial tension experiments were conducted.

Very few results were found in the literature giving cyclic experiment on the PVB. Only *Seshadri* [22] made two cyclic experiments on a PVB interlayer (not exactly the same as ours) at two different strain rates. His results are similar to the one we have here. The cyclic uniaxial tension is of utmost importance in this work as it gives an estimation of the dissipated energy when the polymer is stretched to a certain level of deformation. The amount of dissipated energy by the polymer is directly related to the impact performance of the laminated glass as emphasized by

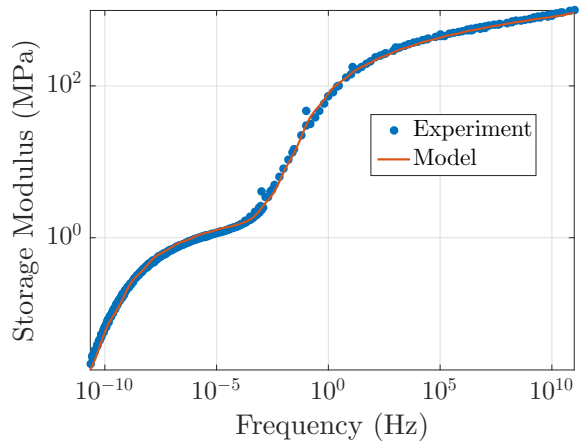

(a) Storage modulus

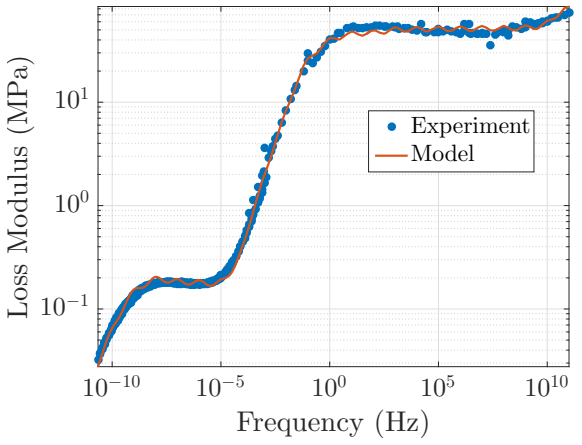

(b) Loss modulus

Figure 3.11: The small strain behavior can be completely described by a 23 terms Prony serie. It will describe both the storage (a) and the loss (b) moduli on these master curves at 20 °C.

a_i	τ_i	a_i	τ_i
1.52e-01	1.00e-11	6.07e-02	1.00e+00
7.59e-02	1.00e-10	3.79e-02	1.00e+01
7.59e-02	1.00e-09	7.59e-03	1.00e+02
7.59e-02	1.00e-08	1.52e-03	1.00e+03
7.59e-02	1.00e-07	2.28e-04	1.00e+04
7.51e-02	1.00e-06	2.28e-04	1.00e+05
7.48e-02	1.00e-05	2.66e-04	1.00e+06
7.44e-02	1.00e-04	2.66e-04	1.00e+07
7.44e-02	1.00e-03	3.04e-04	1.00e+08
6.83e-02	1.00e-02	2.28e-04	1.00e+09
6.83e-02	1.00e-01	7.59e-05	1.00e+10
		1.52e-05	1.00e+11

Table 3.1: The Prony series coefficients for the global DMA/Rheometer master curve at a reference temperature of 20 °C.

Nourry [8].

Effect of time and temperature

Uniaxial tension tests were performed on PVB shouldered samples at different strain rates and five temperatures 10 °C, 20 °C, 30 °C, 50 °C and 70 °C. This set of experiments provides a picture of the large strain behavior from the glassy to the rubbery regime through the glass transition. The different curves can be found in Figure 3.12. In these tests the polymer is stretched to 200% and unloaded at the same strain rate. Different behaviors are observed depending on temperature and applied strain rate:

- At low temperature, 10 °C (3.12(a)) or at the higher strain rates ($1\,s^{-1}$), at 20 °C (3.12(b), the interlayer presents a plastic like behavior. When the strain reaches approximately 10%, the stress is constant up to a strain of 40% as is observed for plastic materials. Moreover, the initial modulus presents a slight increase with the strain rate from 70 MPa to 200 MPa when the strain rate is going from $0.01\,s^{-1}$ to $1\,s^{-1}$ as the material is on the glassy plateau. This behavior is close to the one observed for highly crosslinked polymers.

- At 30 °C, the behavior is close to the one observed for loosely crosslinked polymers. It presents a viscoelastic behavior with a strain hardeing when the strain is higher than 100%. The material is in a rubbery state and presents a soft initial modulus which ranges from 2 MPa to 8 MPa as the strain rate increases from $0.01\,s^{-1}$ to $1\,s^{-1}$.

- At high temperature 50 °C (3.12(d) and 70 °C (3.12(e)), the behavior is still similar to the one observed for loosely crosslinked polymers. However, it is important to notice that at 50 °C the interlayer presents a large permanent deformation (about 20%) which increases at 70 °C (about 50%). This is the result of polymer flow induced at these temperatures by the stretching of the sample. The stress level decreases also a lot: by a factor 4 between 30 °C and 50 °C and a factor 10 between 50 °C and 70 °C. This important change in the stiffness of the material was not observed in the small strain experiments.

- At 20 °C the range of strain rates is large enough to go through the glass transition. Indeed the higher strain rate is similar to the plastic behavior observed at 10 °C and the lower strain rate is close to the rubbery behavior observed at 30 °C.

The different curves present a stiff hardening of the stress when the strain increases above a threshold value (ϵ_m). The threshold value, to this stiff hardening regime, increases with increasing temperatures and decreasing strain rates. At 10 °C the hardening begins around 40% strain. At 20 °C the hardening begins at 50% strain at $1\,s^{-1}$ and only at 100% for the lowest strain rate $0.001\,s^{-1}$. For the higher temperatures (above the glass transition), the hardening starts in between 100% and 150%. For the highest temperatures and slowest strain rates, the hardening is no more visible on the curves.

At high strain rates and low temperatures, the glassy modulus is about 200 MPa and on the opposite side, at low strain rates and high temperatures, the rubbery modulus is around 0.3 MPa. These moduli are comparable to those found in DMA experiments. Moreover, we can build a master curve of the initial modulus found in large strain uniaxial tension by shifting the results found at different temperatures on the reference temperature 20 °C (Figure 3.13). This plot does not display the modulus as a function of the frequency as in the DMA master curves. However, it shows that the glass transition is occurring here at a temperature lower than in DMA. Indeed, at 20 °C, the initial modulus has already decreased more significantly than in the DMA experiment. This result might be explained by the fact that the polymer chain movement is eased by the large strain applied on the material. The glass transition might be shifted to lower temperature by the application of large strains.

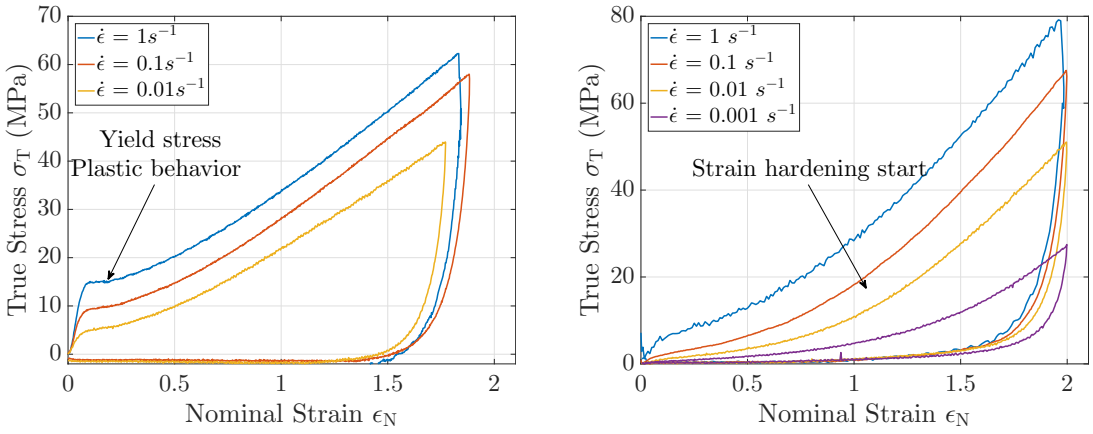

(a) 10 °C

(b) 20 °C

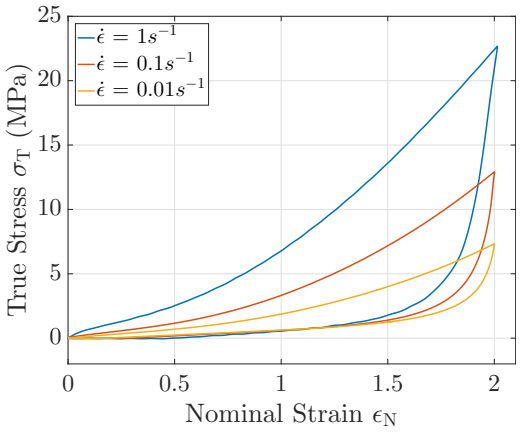

(c) 30 °C

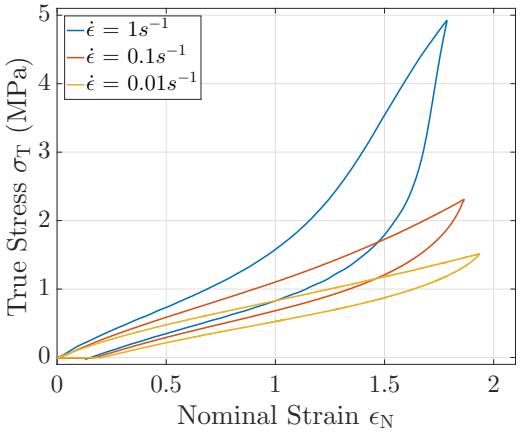

(d) 50 °C

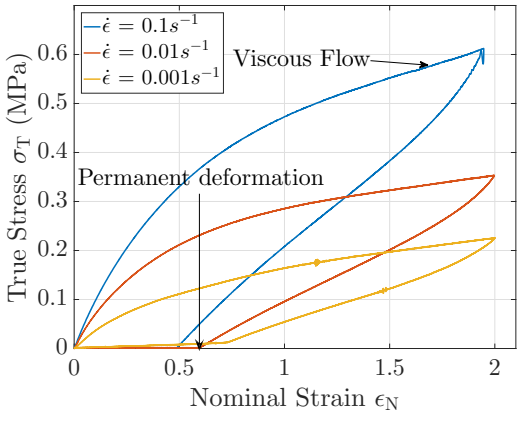

(e) 70 °C

Figure 3.12: Uniaxial tension test at controlled displacement speed and different temperature: 10 °C (a), 20 °C (b), 30 °C (c), 50 °C (d) and 70 °C (e). Up to 150% or 200% of maximal deformation. Loading and unloading are at the same strain rate.

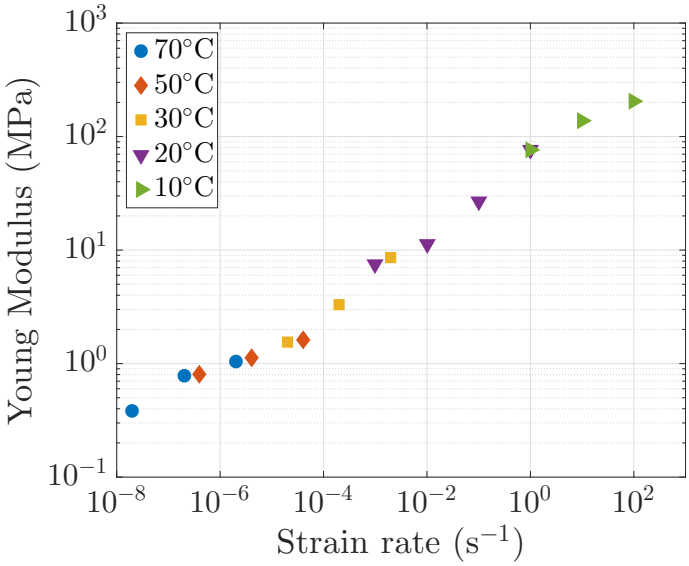

Figure 3.13: The initial modulus measured on the first 5% strain on the different curves for temperatures ranging from 10 °C to 70 °C. Master curve built at 20 °C.

Relaxation experiment

Shift of the glass transition towards lower temperature can be confirmed by the characteristic times found in relaxation experiments. In these tests, the interlayer is stretched up to a certain strain and maintained to this strain value for a certain time. The force is monitored during the loading and constant strain plateau. In Figure 3.14, the relaxation of the stress is plotted as a function of time when the strain is maintained at 50% .This experiment was conducted at 20 °C. The loading strain rate was 1 s^{-1} and the strain was maintained for 1000 s. The stress relaxes very rapidly in less than 10 s.

Characteristic times of the material behavior can be extracted from these results using a Prony series model. These characteristic times are compared to the times found in small strain rheology in Figure 3.15 where the storage modulus calculated with a Prony series model, is plotted as a function of frequency. The reference temperature is 20 °C. The small strain results (in blue) correspond to the characteristic times and moduli found in DMA and rheometer tests (Figure 3.11). The large strain results (in red) corresponds to the previous relaxation experiments (Figure 3.14). At this reference temperature of 20 °C, for large strain the glass transition occurs around 10 Hz whereas for small strain the glass transition occurs around 0.1 Hz. This is similar to the previous result as it implies that the application of large strain on the samples shifts the glass transition temperature towards shorter times or lower temperature. This result means that, in order to model the large

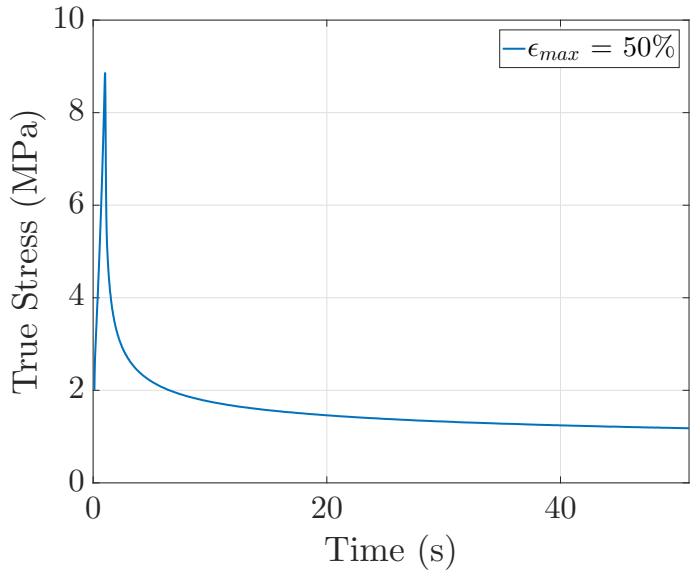

(a) Relaxation during the first 50 s

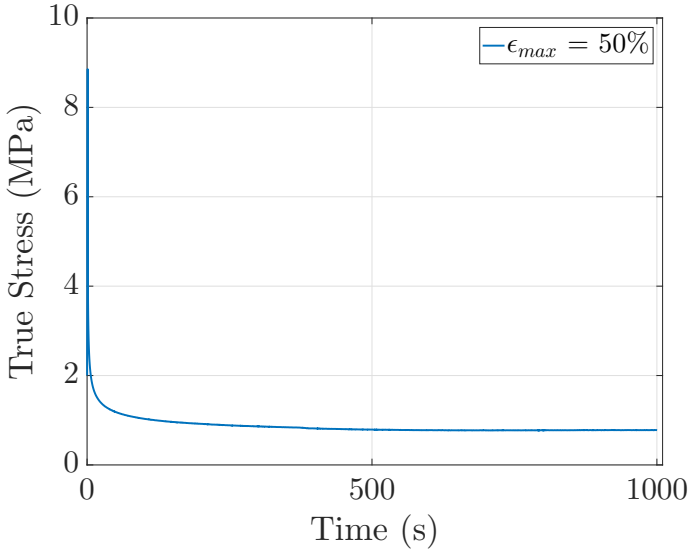

(b) Long term relaxation

Figure 3.14: Relaxation experiments conducted at 20 °C at two different strain level (20 and 50%). Loading strain rate is $1\,s^{-1}$ and relaxation lasts 1000 s.

strain time/temperature dependence of the interlayer, it would be better to rely on the characteristic times found in the large strain relaxation experiments rather than on the ones found in the small strain DMA and rheometer tests.

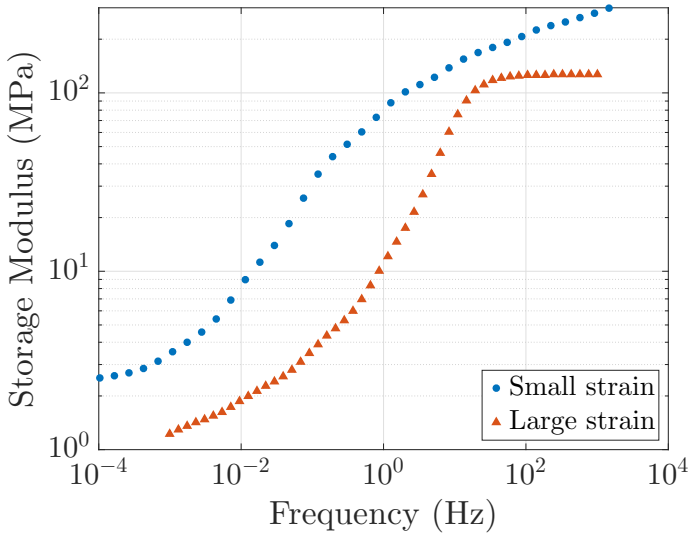

Figure 3.15: Prony series using the characteristic times and moduli found in the relaxation experiment at large strain and in the small strain DMA/Rheometer tests. The reference temperature is 20 °C in both cases. It illustrates the difference induced by the large strain on the time/temperature superimposition.

Dissipated energy: partial conclusion

One of the main targets of this study of the PVB rheology is to determine the dissipated energy during polymer stretching (Figure 3.16). A cyclic uniaxial tension was performed. The area in between the loading and the unloading curve gives the dissipated energy, while the area under the unloading curve gives an approximation of the elastically stored energy that is recovered as the polymer is unloaded. Indeed, during unloading, the thin film of PVB starts to buckle around 100% deformation. Thus the unloading curve has little meaning below this strain. The polymer will recover from this viscoelastic deformation after 1 or 2 minutes.

One can calculate the ratio of dissipated energy over total work provided to stretch the interlayer to 200% strain. This ratio will be denoted R_d. This dissipated energy ratio as a function of strain rate and temperature is given in Figure 3.16. The previous different behaviors are recovered in this graph. At low temperature and high strain rates, the amount of dissipated energy is higher than 80%. This result is similar to the one found by Nourry during impact experiments on laminated glass. He found indeed that about 87% of the impact energy was dissipated,

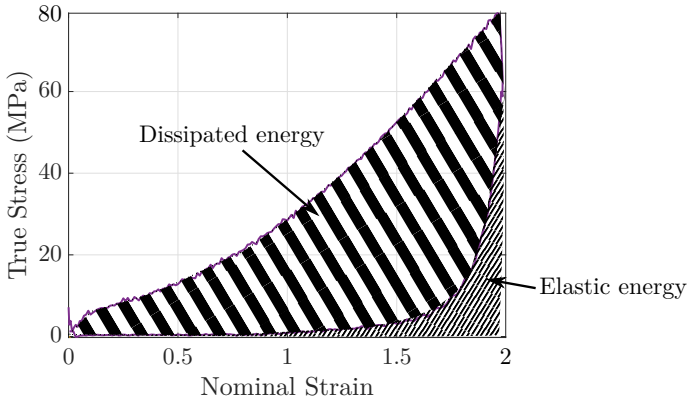

Figure 3.16: Dissipated energy during a traction experiment corresponds to the area in between the loading curve and the unloading curves. The elastic stored energy corresponds to the area under the unloading curve. Here an example on a uniaxial tension test at 20 °C and 1 s^{-1}.

mainly by interlayer deformation, during the impact. This huge amount of dissipated energy is due to the glassy/plastic nature of the PBV. The yield stress and the stiff unloading slope observed in the previous cyclic experiments (Figure 3.12(a)) are indeed similar to the one observed in a plastic material. Other interlayers used for laminated glass such as the SentryGlass ionomer from Dupont, presents similar plastic behavior which lead to large amount of dissipated energy. However, PVB interlayers present also viscoelastic properties which enable full strain recovery and no permanent deformation even at low temperature and high strain rates.

The ratio of dissipated energy strongly decreases as the temperature increases above the glass transition temperature from 30 °C to 50 °C, the polymer gets closer to an elastic rubber. At higher temperature (70 °C), the polymer enters an other dissipation area. The dissipation ratio increases a little bit compared to the one observed for 50 °C. The interlayer behavior, could be assimilated to a viscoelastic fluid in this domain of strain rates and temperatures.

3.4 Strain induced birefringence

Birefringent experiments are used to understand the relationship between the interlayer behavior and its chemical structure. Indeed, the photoelastic signal is related to the local polymer chain orientation which is in some way, related to the mechanical loading. These results will lead to propose a rheological model for the material.

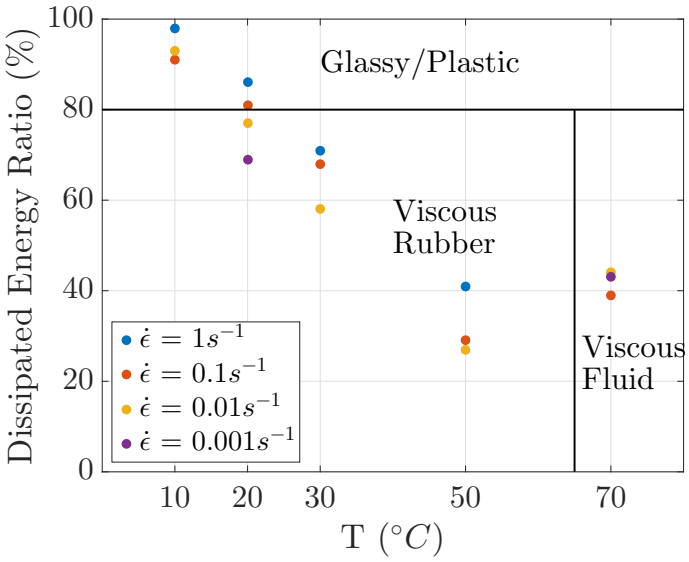

Figure 3.17: Ratio of the elastically stored energy over the dissipated energy as a function of the temperature and loading speed. Different dissipation regimes (Plastic, viscous rubbery and viscous fluid) can be distinguished.

3.4.1 Influence of strain rate and temperature on birefringence

Some photoelastic experiments (see 2.6.3) were performed on the PVB interlayer during uniaxial tension at controlled strain rate and temperature. The experiments were performed with a red filtered light. A typical intensity signal observed during this experiment at 20 °C and 1 s^{-1} is plotted in Figure 3.18. The intensity is a mean value, measured on a square of approximately 10px in the middle of the stretched sample (red square on the frames in Figure 3.18(b)). The intensity oscillates between bright and dark birefringence fringes. When the intensity is maximal the delay introduced by the material in the light propagation results in a polarized wave which is in the same direction as the polarizer (after the quarter wave length plate). The fringe order N is the number of time the received light gets to maximal intensity. The initial intensity being maximal, it corresponds to a fringe order of $N = 0$. In this experiment, the interlayer is stretched up to 100% strain and there are 6 fringes the last one being of $N = 5$th order.

The fringe order also depends on time and temperature (Figure 3.19 and 3.20). At 20 °C, three different strain rates were tested 0.01 s^{-1}, 0.1 s^{-1} and 1 s^{-1} in a uniaxial tension test up to 200%. The result is that the faster the strain the higher the fringe order. Similarly, at 0.1 s^{-1} three temperatures were tested 20 °C, 50 °C and 70 °C in a uniaxial tension test up to 200%. We find that the lower the temperature,

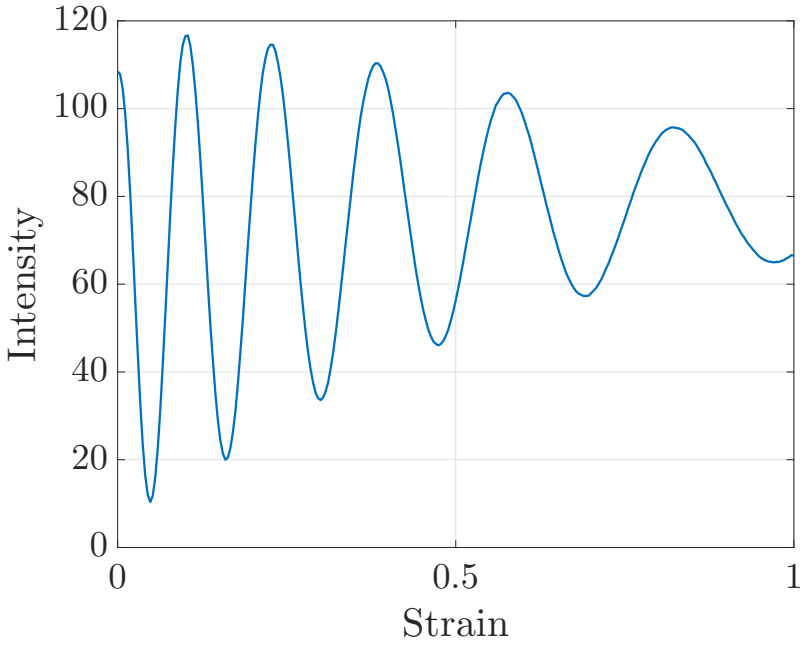

(a) Birefringence normalized intensity

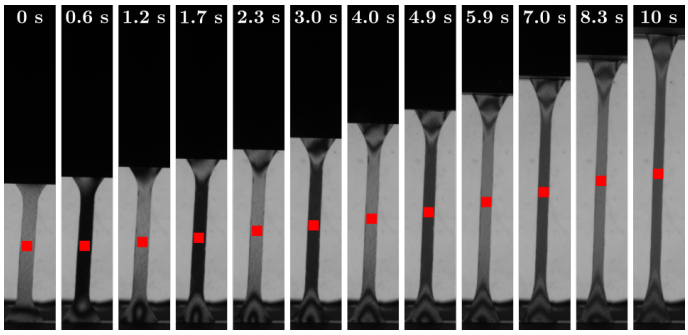

(b) Birefringence experiment

Figure 3.18: Typical birefringence signal during a 20 °C and 1 s^{-1} uniaxial tension test on the PVB interlayer stretched up to 100%.

the higher the fringe order.

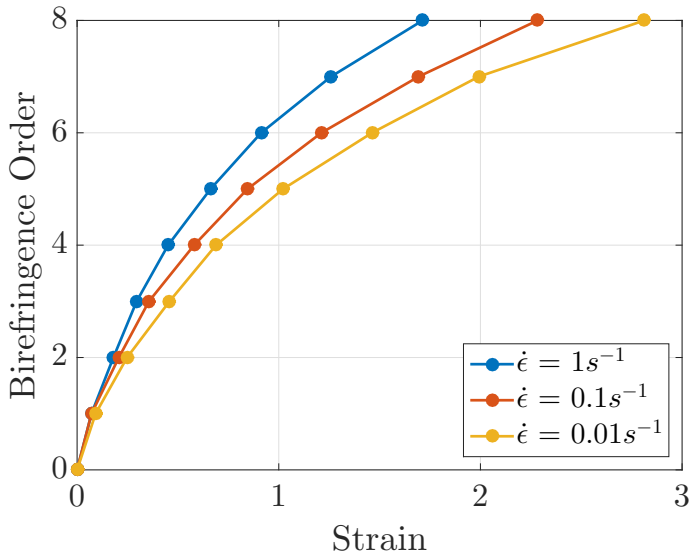

Figure 3.19: Evolution of the birefringence order with strain (up to 200%) as a function of the applied strain rate at 20 °C. Three velocities were compared $0.01\,\mathrm{s}^{-1}$, $0.1\,\mathrm{s}^{-1}$ and $1\,\mathrm{s}^{-1}$.

Moreover, the birefringence is not directly proportional to strain. Considering the Gaussian network as described by Treloar [17], the fringe order is supposed to be proportional to the difference of principal stresses (Equation 2.6.3). However, the non linearities introduced by this simple theory of the polymer network are not sufficient to describe the fringes observed here. Indeed, the same results as in Figure 3.19 are plotted in Figure 3.21, as a function of the Gaussian theory principal stress difference (for an incompressible material in uniaxial tension) and with a corrected value of the interlayer thickness and the relationship diverges from the simple proportionality (that would have been expected) especially at larger strains.

It is also interesting to notice that, after a uniaxial tension test on the interlayer up to 200% deformation, there is no permanent deformation when the sample is removed from the clamps at 20 °C whereas at 50 °C and 70 °C, the remnant deformation described earlier is clearly visible (Figure 3.22).

3.4.2 Birefringence during relaxation experiment

An interesting result arises from a photoelastic measurement during a relaxation test on the PVB interlayer. The interlayer is stretched at 20 °C at $0.1\,\mathrm{s}^{-1}$ up to 200%. The polymer is then maintained at this level of deformation during 1000 s. In figure 3.23, during the loading phase, the usual fringe pattern with 8 fringes (up

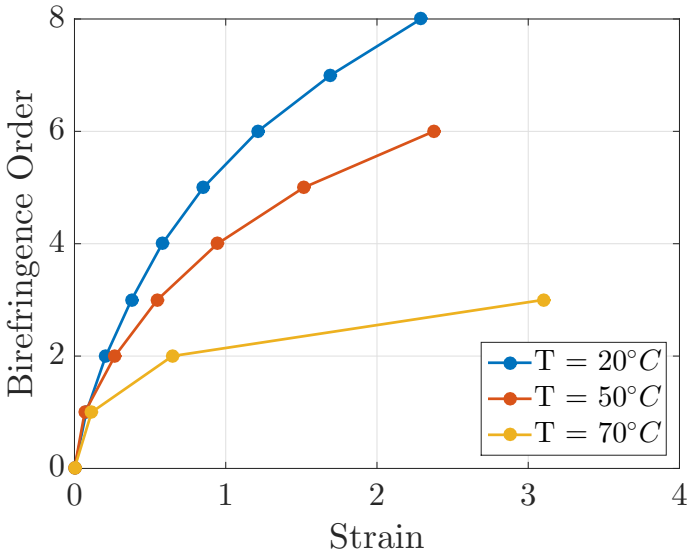

Figure 3.20: Evolution of the birefringence order with strain (up to 200%) as a function of the temperature at $0.1\,\mathrm{s}^{-1}$ applied strain rate. Three temperatures were compared $20\,\mathrm{s}^{-1}$, $50\,\mathrm{s}^{-1}$ and $70\,\mathrm{s}^{-1}$.

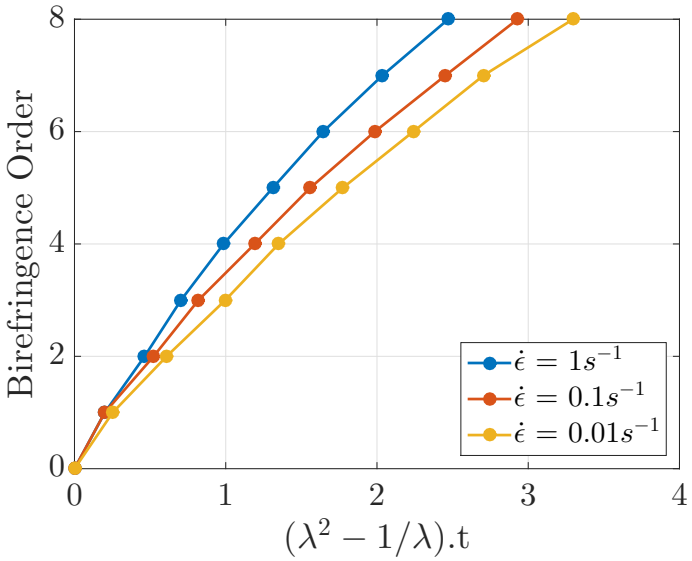

Figure 3.21: Evolution of the birefringence order with Gaussian strain corrected by the calculated thickness t (incompressible material) as a function of the applied strain rate at 20 °C. Three velocities were compared $0.01\,\mathrm{s}^{-1}$, $0.1\,\mathrm{s}^{-1}$ and $1\,\mathrm{s}^{-1}$. λ is the stretch applied onto the interlayer.

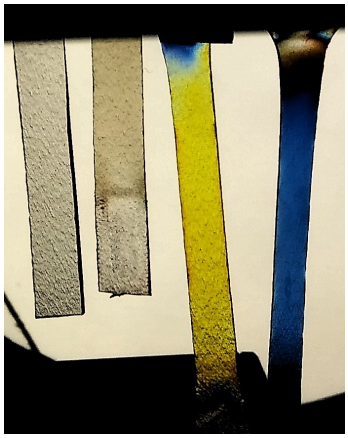

Figure 3.22: Four different samples initially with the same 20 mm length. From left to right: Reference sample in the initial shape, sample stretched at 200% at 20 °C, sample stretched at 200% at 50 °C and sample stretched at 200% at 70 °C. The samples are only clamped by their upper end despite what can be seen from the picture.

to fringe order $N = 7$) is observed. However, during, the relaxation phase, one can see that while the stress relaxes from 180 MPa to 25 MPa in 1000 s (with a very fast decrease down to 80 MPa in the first 10 s), the birefringence signal only varies from half a fringe. The photoelastic signal seems to be quenched by the constant strain imposed on the material.

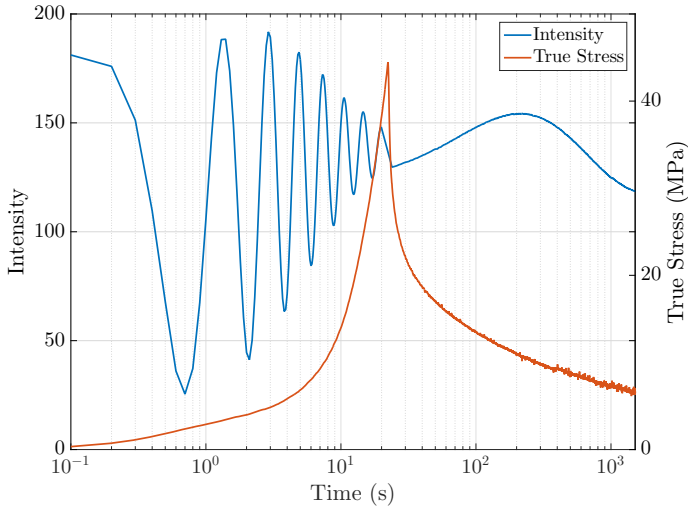

Figure 3.23: Relaxation experiment followed by photoelasticity. Strain increases up to 200% at 0.1 s^{-1} and remains constant for 1000 s. The stress relaxes but the photoelastic signal is not recovered.

The same experiment (loading and relaxation) was made at the same temperature 20 °C and at the same strain rate 0.01 s^{-1}. However, this time the temperature

was increased after 500 s during the relaxation phase (Figure 3.24). In a first experiment the temperature was increased to 50 °C. In a second experiment, the temperature was increased to 70 °C. In both case, the result was completely different from the reference experiment in which the temperature remained constant at 20 °C. During the loading phase, the fringe order goes to $N = 7$. Only half a fringe is recovered at 20 °C. The increase of temperature at 50 °C leads to a partial recovery of the fringe order as four fringes are passing in the reverse direction. At 70 °C, the recovery is more complete as 6 fringes are passing in the reverse direction. Thus the increase in temperature seems to unblock the birefringence mechanisms which can relax at constant macroscopic strain.

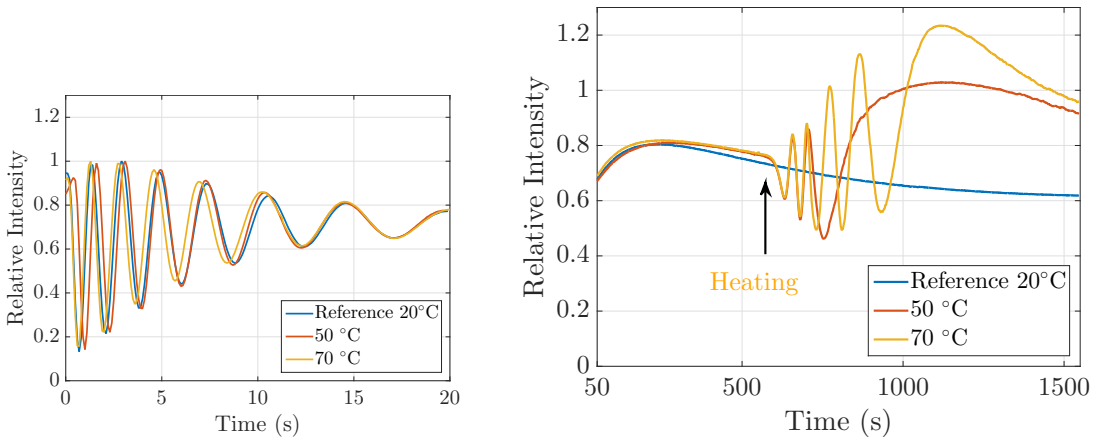

(a) Loading (b) Relaxation

Figure 3.24: Relaxation experiment while heating. A reference at 20 °C is displayed. Two temperatures were tested 50 °C and 70 °C. Loading rate was 0.1 s^{-1} (a). Relaxation lasts 1000 s. Heating start at 500 s after the end of the loading.

3.4.3 Partial conclusion

It is now important to remember that the PVB interlayer is not a crosslinked polymer. The time and temperature dependence of the photoelastic signal can be explained by the viscoelastic properties of an entangled network. However, at constant strain, the stress relaxation observed should also correspond to a simultaneous relaxation of the polymer chain alignment. Indeed, the entangled network which suppors the stress increase during the fast loading should, during the long period of constant strain, relax to its initial randomly organized state. The fact that the photoelastic signal does not evolve significantly a lot during the relaxation of the stress might indicate the existence of distinct phase or of two networks in the material. The fol-

lowing part of this chapter will focus on presenting some evidence of such a second phase. The existence of such a second phase in the PVB has been suggested, from less complete experiments, by *Mertz* [18] and *Schaefer* [23].

3.5 Evidence of a second phase

In order to show the existence of a second phase in the material, DSC experiments were conducted on the PVB. Indeed, *Mertz* [18] in similar experiments found the trace of a second phase. This phase should be more organized than the rest of the polymer network. The DSC results will be confirmed by SAXS experiments made on the PVB during stretching. Finally, from these experimental observations a first picture of the material will arise.

3.5.1 An exothermic signal

During a DSC experiment on the PVB interlayer, two important variations can be observed in the heat capacity. Around 20 °C a faster decrease of the heat capacity corresponds to the glass transition of the polymer. Around 70 °C (from 50 °C to 100 °C) a fusion-like signal is observed which does not correspond to the glass transition as suggested in [24]. After immediate cooling (red curve), a second temperature ramp at 20 °C min^{-1} does not display the same fusion-like signal around 70 °C. However, if during the cooling, a pause of 9 h at 40 °C is observed, the following temperature ramp displays a partial recovery of the fusion-like signal. Thus, the polymer structure leading to this fusion-like signal is not permanently erased but recovers slowly at ambient temperature. This experiment and the observations are identical to the one made by *Mertz* in [18].

The fusion like signal also suggests some form of order to disorder transition. Thus, there might be some regions in the polymer that present a higher level of organization than the rest of the polymer matrix. If this hypothesis is correct, these regions should be visible in other experiment such as Small Angle X-ray Scattering experiments.

3.5.2 Evidence through X-ray scattering

SAXS experiment were performed on the PVB interlayer at two different temperatures (23 °C and 70 °C) during uniaxial tension test at a strain rate of 0.01 s^{-1} up to 300% deformation.

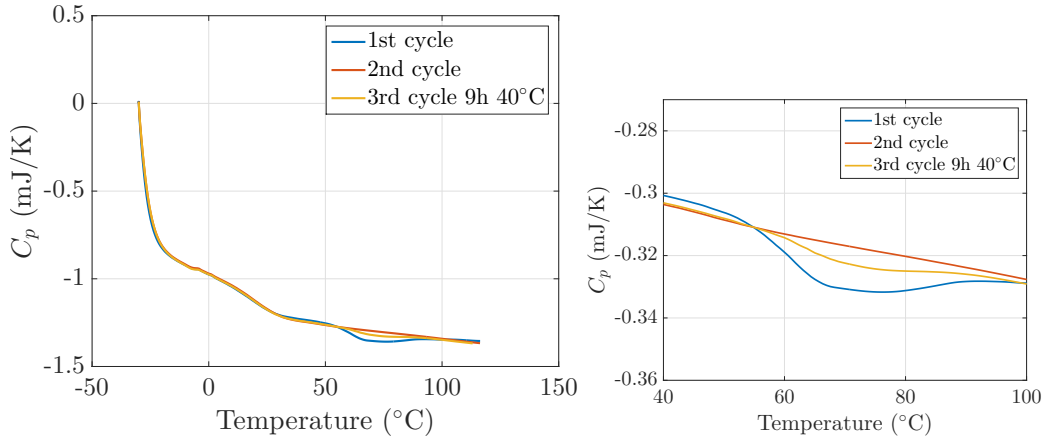

(a) The three heating ramps (b) Zoom

Figure 3.25: Three DSC cycles at 20 °C min^{-1}. First cycle shows an exothermic - fusion like signal around 70 °C. The second cycle after a fast cooling at 20 °C min^{-1} do not display this signal. Finally the third cycle done after 9 h at 40 °C presents a partial recovery of the signal.

At 23 °C in Figure 3.26, there is no change in the SAXS signal in the traction direction (Figure 3.26(a)). In the direction perpendicular to the traction direction however, a signal enters from the small angle while the strain increases (Figure 3.27(b)). This signal is related to the distance between the more organized regions. At 23 °C when the strain increases, this distance decreases in the direction perpendicular to the traction whereas it increases in the traction direction. The distance at 100% strain between these objects is small enough to be detected in SAXS experiment. When the strain is higher than 100%, this distance becomes smaller than d> $\frac{2\pi}{10^{-2}}$ ≈300 nm.

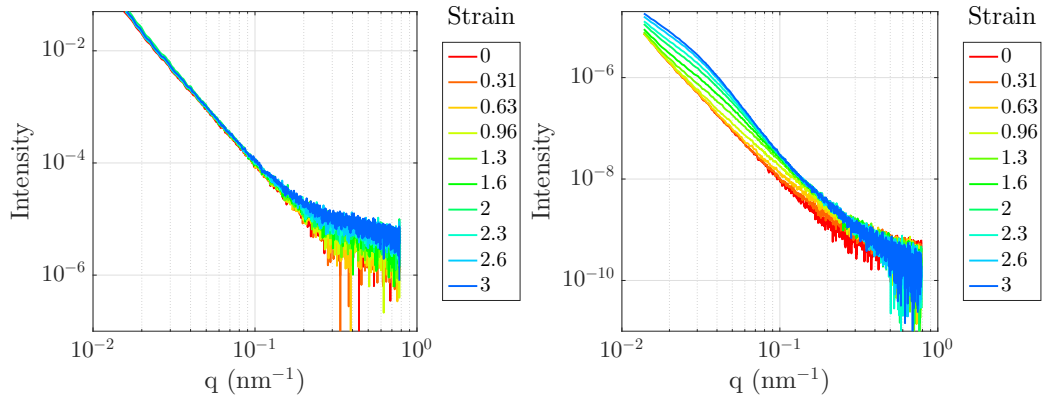

(a) Traction direction (b) Direction perpendicular to traction

Figure 3.26: SAXS experiment at 23 °C during a uniaxial tension experiment.

On the contrary at 70 °C, no signal is visible whatever the direction is (Figure 3.27). This could mean that the distance in between the organized regions is too large to be seen in the SAXS experiment or more probably as suggested by the DSC experiment, that these regions have been partially or totally destroyed.

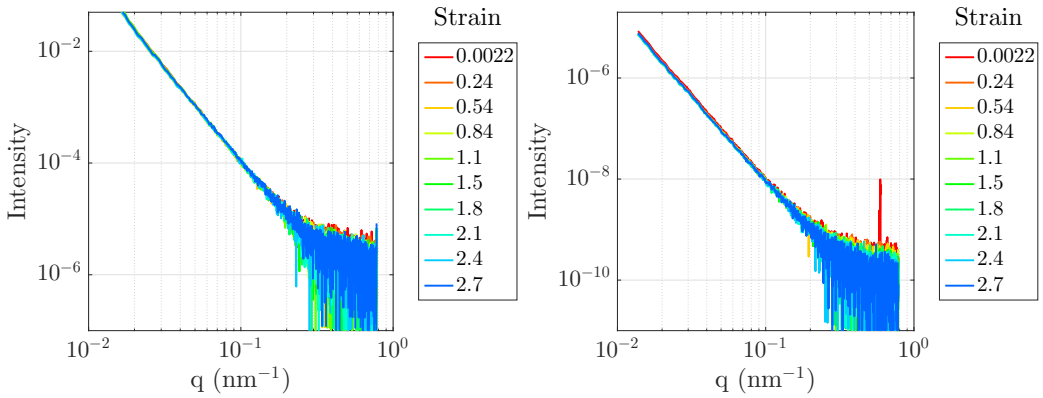

(a) Traction direction (b) Direction perpendicular to traction

Figure 3.27: SAXS experiment at 70 °C during a uniaxial tension experiment.

3.5.3 A schematic model of the structure

From the DSC and SAXS experiments, a model picture of the PVB chain organization can be drawn. The PVB used in our experiment contains about 18wt% of hydroxyl groups and almost 20wt% of plasticizer.

The DSC results suggest that there is a more organized phase in the material bulk which might loose its organization above 70 °C. This phase recovers its organization after several hours at a temperature of 40 °C. At this temperature the molecular motion is sufficient for the region to reorganize. Klock suggested that this second phase, is made out of regions of the polymer chains with higher hydrogen bond concentration [19].

The SAXS experiments show that these more organized regions are at a distance larger than 300 nm from each other. Similar results were obtained by *Schaefer* [23]. In this paper, *Schaefer* used NMR and SANS experiments to show that the material can be viewed as a two phase material: 1. A matrix of diluted polymer chain with a high concentration of plasticizer. 2. Stiffer nodules with a lower plasticizer concentration. According to the author, these nodules are based on strong hydrogen bond interaction between hydroxyl groups of different polymer chains. According to his results, these nodules are about 10 nm to 50 nm large.

Both *Mertz* and *Schaefer* point out that more plasticizer results in a higher segregation of these two phases in the PVB structure.

From these results and from the literature, the image presented in Figure 3.28 can be made. The polymer chains are not chemically crosslinked. However, they are entangled and physically connected by hydrogen bonds. These physical bonds can be made between the hydroxyl groups of the same polymer chain (intra chain H bonds) or with another chain (inter chain H bonds). Moreover, the hydrogen bonds tend to form strong nodules in which the chains are connected to one another through multiple hydrogen bonds. The polymer chain connected to the nodules (in red) are constrained by the other chains in the vicinity of the hydrogen bond cluster. Thus, these regions are more organized and stiffer than the surrounding matrix. In this matrix, the chains which are not involved in the nodules (in green), constitute a softer phase. The plasticizer increases the chain movement in the soft matrix. The PVB structure can be seen as two mixed chain networks: the first one is not connected directly to the cluster while the second one is physically crosslinked by the hydrogen bond nodules.

The existence of these two networks and of the H bond nodules, in the material, should be related to its rheology. In the final part of this chapter we will try to derive a rheological model from the PVB structure.

3.6 A rheological model: two dissipation mechanisms

We have seen here that the PVB interlayer presents a time/temperature dependent behavior. This behavior can be described by a generalized Maxwell model at small strain. At larger strains, this model no longer describes the PVB behavior, which presents different types of dissipation mechanisms depending on strain rate and temperature. At temperatures lower than the glass transition temperature 30 °C or at high strain rate, the material is glassy and plastic. At temperature above the glass transition temperature, the material behaves as a viscoelastic rubber. At temperature higher than 70 °C, the behavior changes into a highly viscous fluid. We are going to provide a rheological model that captures these different regimes and is compatible with the different experimental observations in the photoelastic measurement and in the DSC and SAXS experiments.

First we will consider the polymer chains alone. Their response can be described

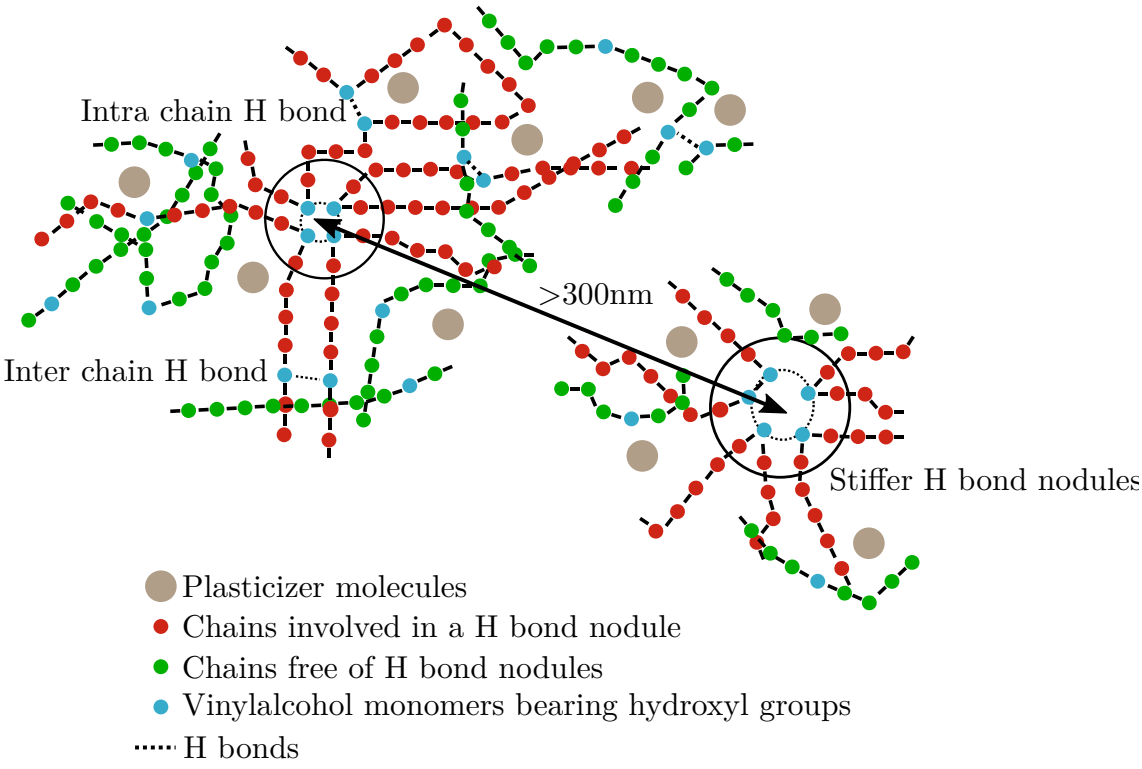

Figure 3.28: A schematic view of the two phases in the PVB. A soft PVB matrix surrounds stiffer and more organized H bonds nodules. These nodules are at a distance greater than 300 nm from each other.

by a Maxwell spring/dashpot model modified to capture the large deformation (Figure 3.29). The spring in this model will not present a linear elastic response but a non linear response such as the one described in the Arruda-Boyce model (See 2.4.2). The long term response corresponds of a spring with a shear modulus μ_∞ and a limit chain extension λ_m. The other characteristic times τ_i are modeled by a dashpot with a similar Arruda-Boyce spring attached (μ_i). Here for the sake of simplicity only one characteristic time is represented.

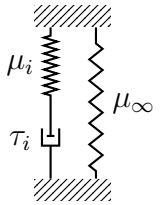

Figure 3.29: PVB chain rheological model.

This model will properly describe a time dependent non linear material. However, this model is not sufficient to explain some results which have been previously described.

First at high strain rate and low temperature, a plastic like behavior has been observed. The dissipated energy does not decrease as the temperature decreases. On the contrary, in this model, as soon as the material is far enough below the glass transition, it will recover an elastic behavior with little dissipation.

Secondly, the birefringence order increases during a traction experiment but it does not change significantly during a relaxation experiment. The birefringence order is also higher at a given strain for faster strain rates and lower temperature. In the model, if the birefringent spring is associated to a short time dashpot, the signal will be more important at high strain rate and low temperature but it will relax rapidly with the stress. On the contrary, the birefringent signal could be associated to a long term dashpot, in order to block it during the relaxation. In this case the birefringent signal will not be more important at low temperature and high strain rates than at high temperature and low strain rates, which again is in contradiction with some of the data.

In order to properly model the birefringent behavior along with the plastic like behavior at low temperature and high strain rate, an other branch has to be added in parallel of the previous model (Figure 3.30). This second branch will be responsible for most of the photoelastic signal. The time dependence and the elasticity related to this branch are, similarly to the previous branches, described by a dashpot with

a characteristic time τ_γ and a non linear Arruda-Boyce spring with a modulus μ_γ^0. In serie of this dashpot and this spring, another block enables the increase of the photoelastic signal at short time and its conservation at constant strain level. This block is constituted of a slider with a threshold stress σ_γ and a spring with a modulus μ_γ. The slider is only activated if the stress increases above a threshold stress. Thus during the loading the birefringence signal changes. During the relaxation test, the slider will be blocked and the birefringence signal in the spring μ_γ will not change while the stress stored in the spring μ_γ^0 is free to relax.

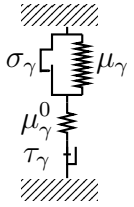

Figure 3.30: Plastic part of the rheological model of the PVB

The resulting final model is represented in Figure 3.31. This rheological model will also explain the different dissipation regimes observed in the large strain experiments. At temperatures above the glass transition temperature, the plastic part of the model will not be triggered because the stress remains below threshold; the material will be a viscoelastic rubber. At lower temperature or higher strain rate, this second plastic branch will be activated when the stress reaches the critical σ_γ leading to plastic dissipation. This model is close to the Bergström-Boyce model [25] in which two parallel mechanisms are used to describe the mechanical behavior of the interlayer. A first channel is hyper-elastic while the second one introduces dissipation in a purely plastic manner. The model has been extended with the introduction of a second viscoelastic dissipation mechanism in the hyper-elastic branch of the model [26].

Finally, PVB presents hydroxyl groups which are able to form stiffer nodules and we have seen that two networks can be used to describe the polymer structure. The two dissipative branches in the rheological model could also be understood as representative of these two networks. The chains which are not involved in the nodules are modeled by the visco-hyperelastic part of the model whereas the chains involved in the H bond nodules are modeled by the plastic part of the model.

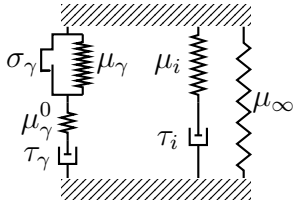

Figure 3.31: A rheological model for the interlayer. Two dissipation mechanisms are present in this model.

Main results

- Rheological study in small and large strain regimes.
- High level of dissipation at large strain.
- Birefringent behavior:
  - Photoelastic signal dependent on the strain rate and temperature.
  - Relaxation of stress is not correlated to a recovery of the photoelastic signal.
- PVB structure:
  - H bonds nodules: stiffer and more organized.
  - Two networks: Chain involved in nodules vs. Chain free of nodules.
- A rheological model: two branches of dissipation (plastic and visco-hyperelastic).

Chapter 4

Model delamination experiment

4.1 Introduction

The previous chapter 3, has shown the origin of the dissipation of energy in the polymer structure. The model experiment will now be used to explore the loading of the interlayer during its delamination from glass. The rheology of the PVB interlayer in uniaxial tension displays different dissipation mechanisms. They are activated at different strain rates and temperatures. In an impact test, the interlayer is subjected to different mechanical loadings mainly uniaxial tension and shear. It might also encounter different strain rates regimes as it delaminates from the glass. Our purpose is to identify the different zones of stretching and strain rates encountered by the interlayer in these zones. This will enable a direct link between the rheology of the PVB and the calculation of the energy dissipated during the delamination process. Due to the extreme complexity of an impact test, we decided to introduce a model experiment, which focuses only on a single type of mechanical loading occurring during the impact. Different geometries have been used in previous studies to characterize the interlayer/glass delamination mechanisms.

A peel test can be used to study the glass/interlayer adhesion. *Pelfrene* [27] used such a peel experiment. A rigid back is attached to the interlayer to prevent the stretching of the free arm during the delamination. In this test, the peeling force was measured and used to build a finite element model of the experiment. Using cohesive elements to represent the interface and a linear viscoelastic model for the interlayer rheology, they showed that most of the energy is dissipated by the interlayer deformation in the close vicinity of the crack tip. The linear viscoelastic modeling of the interlayer in this region was found to be no longer appropriate due to the large deformation involved (300%).

In [28], *Seshadri* presented a different testing geometry. The compressive shear strength (CSS) test consists in a shear and compression combined loading on a laminated glass sample (Figure 4.1). The laminated sample is at 45° from the loading direction. The polymer is confined in between the two glass plates and is free to deform in between. This loading might be more representative of the shear applied on the interlayer. Thanks to this test and a finite element model, they were able to extract a value for the apparent fracture energy.

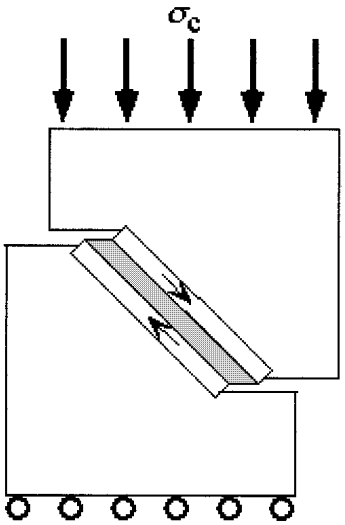

Figure 4.1: Schematic view of the CSS test in which the interlayer in between the two glass plates is subjected to both shear and compression.

However, both these tests did not describe the bridging of the glass parts by the stretched interlayer described by *Seshadri* in [12] and [29]. In order to do so *Seshadri* used the Through Crack Tensile Test (Figure 4.2). It consists of a uniaxial tension applied on a pre-cracked laminated glass sample. This experiment has been also used in other studies on laminated glass ([30], [31], [32], [33], [34]). This geometry focuses on the second phase of the impact (Figure 1.3) during which the plate goes into a macroscopic bending. During this step, the glass parts still stick to the interlayer and are going away from each other. This leads to the delamination of the interlayer and its stretching in between the delamination fronts. Due to the large curvature of the flexed structure, the local mechanical loading in between the glass parts can be assimilated to a uniaxial tension. This model test reproduces a mode I stretching of the delaminated interlayer. Apart from *Delince* [33], all these studies found that there can be a stable delamination growth. In this regime, the polymer is stretched to a high level of deformation leading to a large amount of dissipated energy.

In this chapter, we will show that in the TCT test, there is a limited range

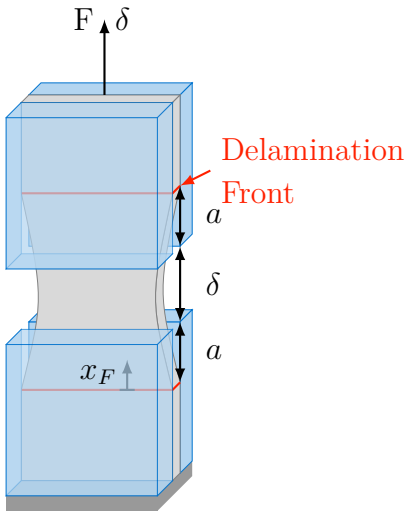

Figure 4.2: Through Crack Tensile Test (TCT Test), model experiment. A uniaxial tension test is conducted on a pre-cracked laminated glass sample. The interlayer is stretched in between the delamination fronts which propagate in opposite directions.

of temperature and applied velocity in which the delamination is steady and the delamination fronts straight. We will show, that inside this stable delamination regime, the polymer stretching from 0% strain to a high strain value, occurs on a characteristic length scale close to the interlayer thickness.

4.2 Description of a typical Through Crack Tensile Test

The TCT Test has been described in 2.5.2. Experiments were conducted at various temperatures 5 °C, 20 °C and 50 °C and with different applied velocities ranging from $0.03\,\mathrm{mm\,s^{-1}}$ to $100\,\mathrm{mm\,s^{-1}}$.

During a typical TCT Test at 20 °C and $10\,\mathrm{mm\,s^{-1}}$ four delamination fronts propagate at a constant pace in two opposite directions. In between these fronts the interlayer is stretched (Figure 4.3).

As found by [30], [12] and [31], a steady state delamination is observed. The delamination force F_{TCT} reaches a plateau which mean value F^0_{TCT} is approximately 500 N after a first overshoot (Figure 4.4).

During the experiment, the upper glass edge velocity $\dot{\delta}$ is controlled. The position of the fronts relative to the glass edge a is recorded. From this measurement, the stretch (λ_{TCT}) can be determined as the ratio of the delaminated interlayer length ($\delta + 2a$) over the initial length occupied by this part of the delaminated interlayer

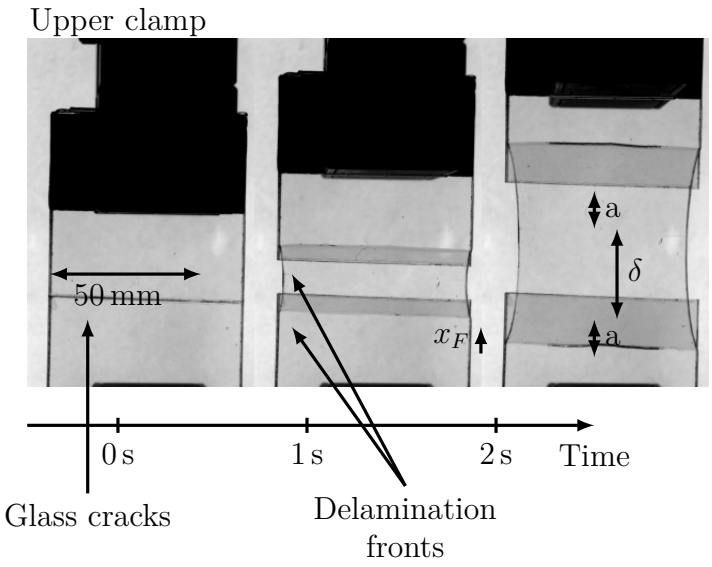

Figure 4.3: A typical TCT experiment at 20 °C and 10 mm s^{-1}. Sample width is 50 mm. δ is the upper clamp/upper glass displacement. a will denote the position of the delamination front relative to the glass edge. x_f will be the distance of a given point to the point at the vertical of the delamination front.

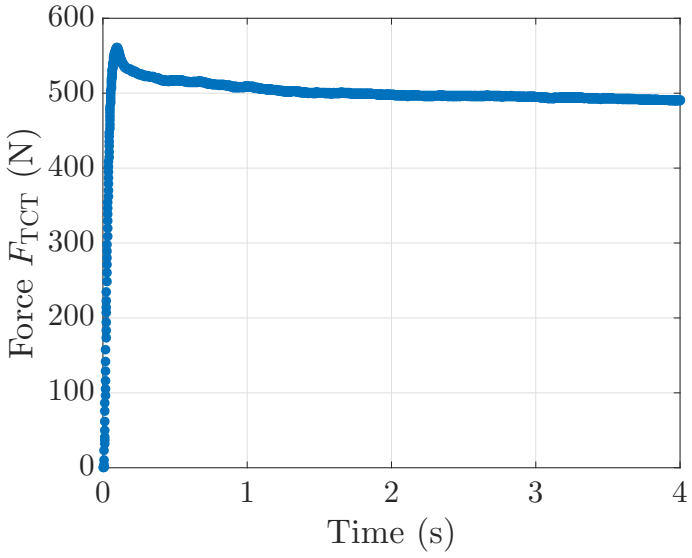

Figure 4.4: Delamination forces F_{TCT} reaches a steady state which mean value is $F^0_{\mathrm{TCT}} = 500$ N during a TCT experiment at 20 °C and 10 mm s^{-1}.

$(2a)$ which is the length between the delamination fronts and the glass edge (Figure 4.2): $\lambda_{\mathrm{TCT}} = \frac{\delta+2a}{2a}$. The nominal strain is then defined as $\epsilon_{\mathrm{TCT}} = \lambda_{\mathrm{TCT}} - 1 = \frac{\delta}{2a}$. In Figure 4.5, the upper glass displacement δ is plotted as a function of the delaminated length $2a$. As the fronts propagate symmetrically the slope of the curve gives us a mean value of the strain $\epsilon^0_{\mathrm{TCT}}$ close to 1.4. As shown on Figure 4.6, the strain is also constant through the whole test. This underlines the fact that the front propagation occurs at a velocity close to $3.5\,\mathrm{mm\,s^{-1}}$ which is proportional to the applied displacement velocity ($\dot{\delta} = 2\epsilon\dot{a}$).

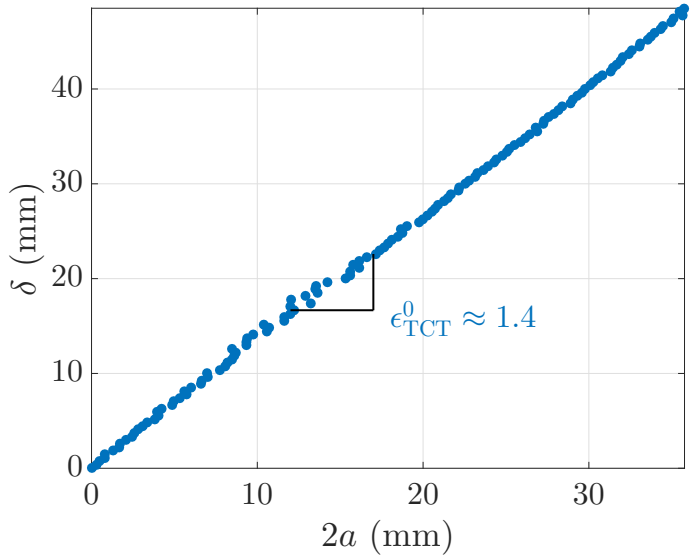

Figure 4.5: In the 20 °C and $10\,\mathrm{mm\,s^{-1}}$ TCT Test, the symmetric delamination of the fronts occurs at a constant velocity close to $3.5\,\mathrm{mm\,s^{-1}}$ proportional to the applied displacement velocity. Thus the delamination length $2a$ is proportional to the displacement applied on the glass δ.

4.3 Influence of velocity and temperature on delamination: phase diagram

4.3.1 Results

The steady state delamination described in the previous part, is not observed for all temperatures and velocities. At a given temperature, there is an intermediate velocity regime in which the delamination occurs in a symmetric and steady manner as described before. At lower imposed velocities, the delamination fronts are no longer straight and start to undulate. Propagation often stops after some time

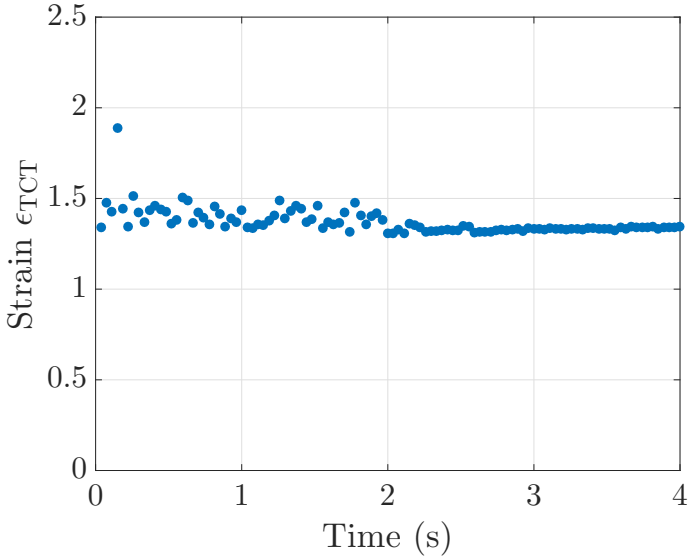

Figure 4.6: In this 20 °C and 10 mm s^{-1} TCT Test, the nominal strain ϵ_{TCT} reaches a steady state plateau which mean value is $\epsilon^0_{TCT} = 1.4$ and that is related to the symmetric delamination of the fronts at a constant velocity.

leading to the rupture of the interlayer (Figure 4.7(a)). Finally at higher pace, even if the delamination occurs as in the steady state delamination regime, the interlayer toughness is not sufficient which often leads to a brittle fracture of the interlayer (Figure 4.7(a)). It is worth noticing that the brittle rupture of the interlayer in the high velocity regime is different from the one in the low velocity regime, in which the crack tip is largely blunted. Measurements could only be made in the steady state regime as it was not possible to obtain a stable delamination in the lower or higher velocity regimes.

In Figure 4.8, the mean delamination force F^0_{TCT} is plotted for all the displacement rates and temperatures investigated. There are strong variations of the force which increases as the velocity increases or as the temperature decreases. On the same figure, the delamination behavior is divided in three regimes. The limits displayed here are roughly estimated.

In Figure 4.9, the average nominal strain ϵ^0_{TCT} is presented as a function of applied velocity and temperature. There is a significant dependence of the strain with the temperature. Indeed at 5 °C, the strain is in a range from 1.05 to 1.3, at 20 °C it ranges from 1.1 to 1.6 and at 50 °C the strain goes from 1.8 to 2.05 for the different velocities. In the steady state delamination regime, the strain is slightly increasing with the velocity at 5 °C. This nominal strain increase is more important at 20 °C. At 50 °C the strain is almost constant with the applied velocity. The large error bars observed at 20 °C for the highest velocities correspond to cases where the

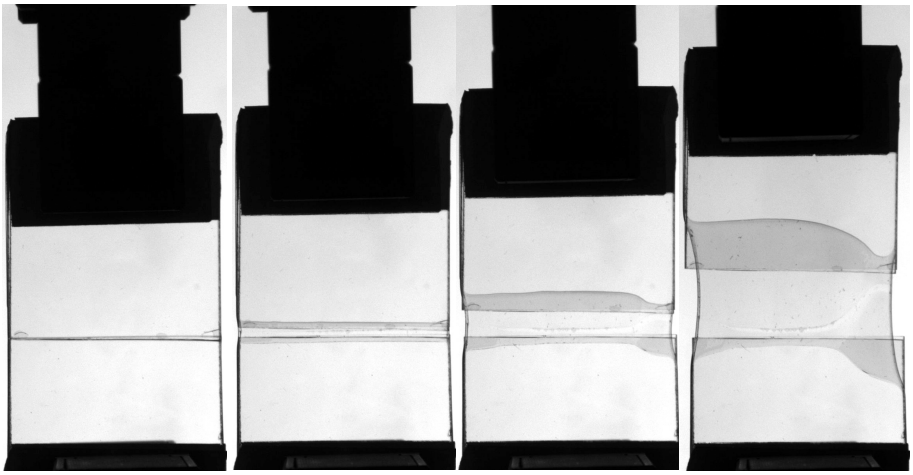

(a) TCT test at 20 °C and 0.01 mm s^{-1} in the low velocities/high temperatures regime.

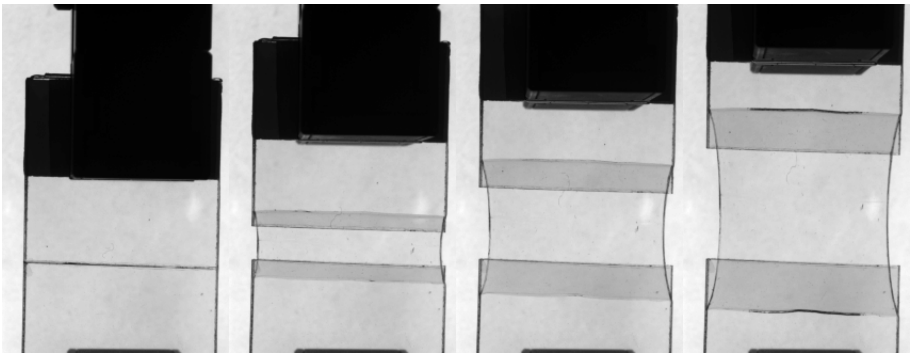

(b) TCT test at 20 °C and 10 mm s^{-1} in the steady state regime.

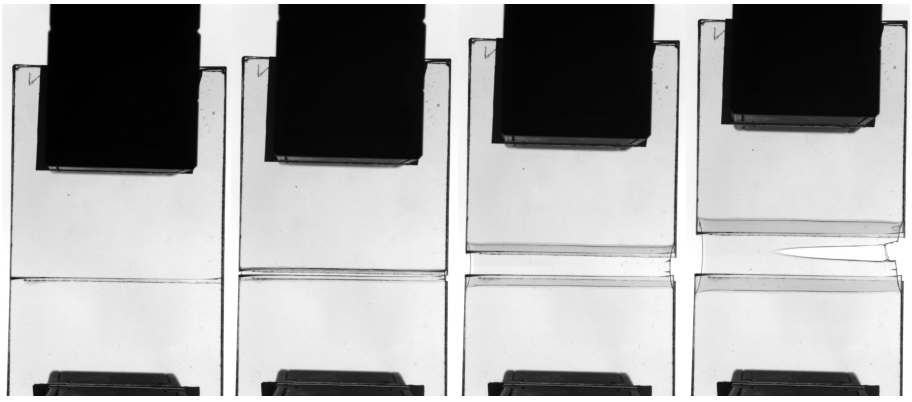

(c) TCT test at 5 °C and 10 mm s^{-1} at the limit of the high velocities/low temperatures regime.

Figure 4.7: Out of the steady state delamination regime, two different behaviors are observed. (a) At low velocities or high temperatures, the delamination fronts undulate and stop sometimes leading to the interlayer fracture. (b) In the steady state regime. (c) At high velocities or low temperatures, the delamination propagates symmetrically but the interlayer breaks rapidly in a brittle manner.

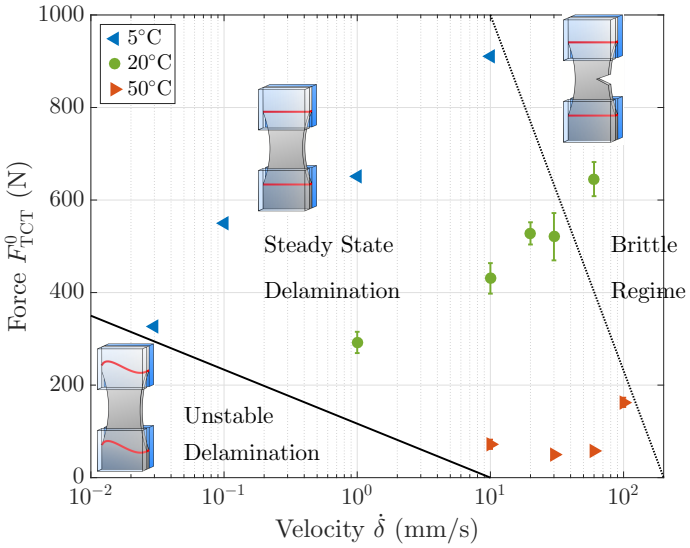

Figure 4.8: The mean steady state delamination force F^0_{TCT} increases with velocity $\dot{\delta}$ and decreases with temperature. The dark lines arbitrary delimit the three delamination regimes. Measurements were only possible in the intermediate regime where no buckling of the front (low velocities and high temperatures) or brittle nature of the interlayer (high velocities and low temperatures) are observed.

interlayer ruptured after a small delamination.

4.3.2 Comparison with previous studies

It has been pointed out in previous studies such as the one conducted by *Butchart* [35] or *Delincé* [33] that the stable delamination regime is not trivial to obtain. Even if the PVB grades used in these studies are, in some cases, different from the one we use here, this might reflect the fact that their experiments were conducted at low imposed velocities and ambient temperature. They observed, as we did, the same unpredictable behavior of the delamination fronts which stop after a small delamination length leading to the rupture of the interlayer. Our observations might give a key to determine if the delamination in the TCT test is going to occur in a steady state manner.

Furthermore, it appears that the temperature control is critical, as the PVB glass transition is broad and spans from 20 °C to 30 °C. Thus around the room temperature a small variation of the temperature might lead to a dramatic change in the interlayer behavior leading to a large shift in the stable delamination regime. This aspect of the problem is not tackled in all the previous studies.

Faster TCT experiments were done by *Ferretti* in [36]. They reach a stable delamination regime and conclude, as we do, that the applied velocity is related

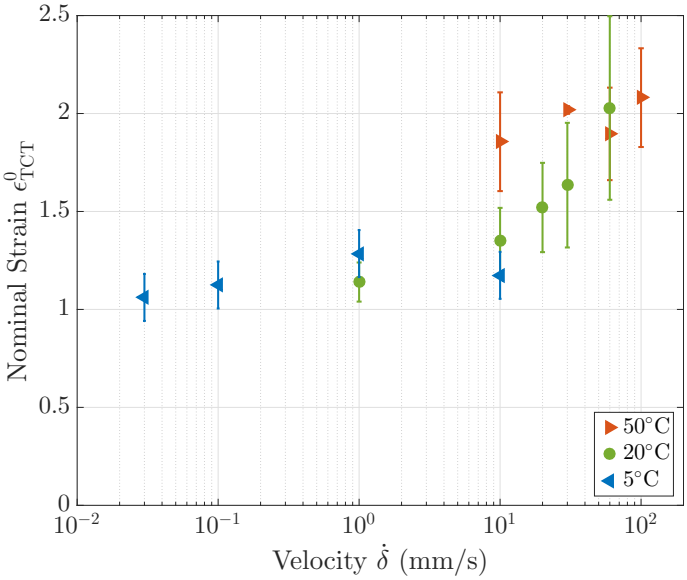

Figure 4.9: Dependence of the mean nominal strain ϵ^0_{TCT} with velocity and temperature. The dependence with the applied velocities is blurred by large error bars. This large error in the strain measurement at 20 °C for the highest strain rates is due to early rupture of the interlayer after a small delamination and to the small amount of data that results of a low video frame rate.

to the delamination stability. Furthermore, they add that this stability is related to the more important stiffness of the interlayer at higher strain rates. It could be related to the instabilities we observed at lower strain rates. An hypothesis could be that, in a softer interlayer, the stress can not be transmitted uniformly along the front which might lead to its undulation.

4.4 Distribution of the deformation of the interlayer in the TCT test

The point of this chapter is to evaluate how the interlayer is loaded as it delaminates from the glass during impact. This information is not easily accessible during the impact test (see 1.2.2). The TCT test was used in the previous measurements to show that the nominal strain during steady state delamination, reaches a constant average value. As the interlayer behavior is highly dependent on the strain rate it is also important to determine the length over which the interlayer is stretched from 0 to the average value ϵ^0_{TCT} from which the strain rate involved in this region can be deduced. That would be essential to understand the dissipating mechanisms which will be studied in the next chapters.

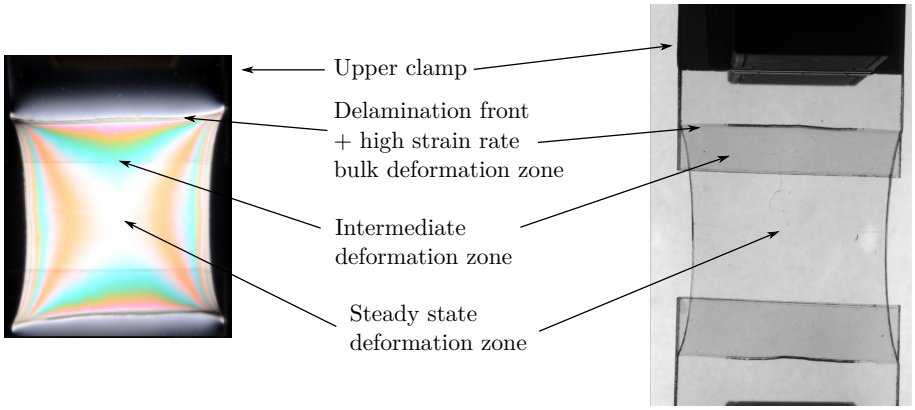

Figure 4.10: A photoelastic experiment conducted on a laminated glass sample during a TCT experiment at 20 °C and 10 mm s^{-1}. Different deformation zones are visible on this picture. The strain is homogeneous far from the delamination front.

By taking a macroscopic snapshot, in a photoelastic setup, it is possible to observe the variations of the strain field (Figure 4.10). The vertical fringes correspond to edge effects. In these regions, the strain might be spatially not homogeneous but it does not involve high strain rates as the fronts are propagating in a direction orthogonal to the fringes. The different zones on which the interlayer is stretched can be seen on this picture by looking at the horizontal fringes. Close to the delamination front, the high fringe concentration might be related to a high strain rate region. A second region is observed over a length scale similar to the sample width, in which the strain might evolve more slowly. Finally, far from the delamination front and from the sample edges, the strain seems to be constant and rather homogeneous. In order to measure more precisely the length of these stretching zones, digital image correlation and more quantitative photoelastic experiments were performed.

4.4.1 Deformation zone measured by photoelasticity

The size of the fast stretching zone close to the moving delamination fronts can been observed in photoelastic measurements performed during the through crack tensile test. Figure 4.11 shows the results of the TCT test conducted at 20 °C and 10 mm s^{-1}, on three samples with different interlayer thicknesses 0.38 mm, 0.76 mm and 1.52 mm. The photoelastic signal was measured on a zone of approximately 4 mm length, on a vertical line, in the middle of sample. As delamination occurs in a steady state, the complete spatial signal was reconstructed by shifting the different curves obtained at different times, using the front velocity.

The birefringence fringes are all concentrated in a zone with a length close to

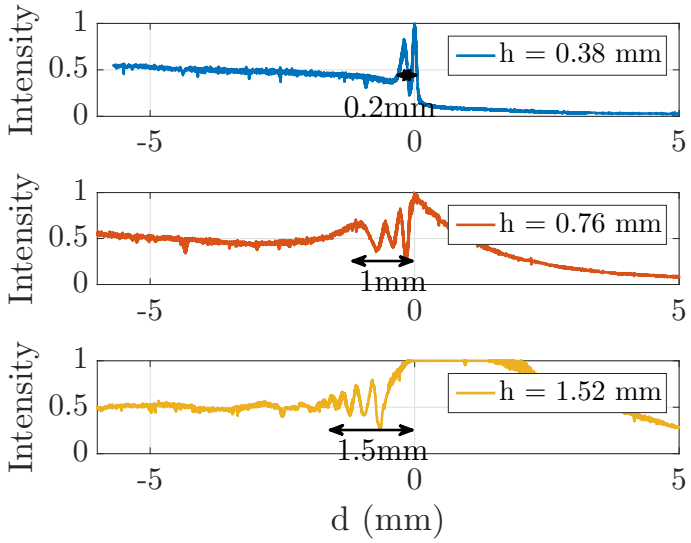

Figure 4.11: Photoelastic measurement conducted close to the delamination front during a TCT experiment at 20 °C and 10 mm s^{-1}.

the interlayer thickness. Thus, most of the stretch occurs over this length scale. Furthermore one can see that the number of fringes is increasing when the thickness of the interlayer increases. However, it is difficult from this experiment alone to tell if this is due to an increase in the stretch or to the change in thickness. In order to get a more quantitative measurement of the strain profile in this fast stretching zone, digital image correlation measurements were performed.

4.4.2 Fast stretching zone measured in DIC

A TCT experiment has been conducted at 10 mm s^{-1} and 20 °C, in the steady state regime. Two interlayer thicknesses were tested: 0.76 mm and 1.52 mm. The delamination front velocity was found to be almost identical for both thicknesses (3 mm s^{-1} and 4 mm s^{-1} for the 0.76 mm and 1.52 mm thickness respectively). Far front the delamination front, the interlayer is stretched to a maximal value close to ϵ^0_{TCT}.

Using digital image correlation, the displacements field is recorded while the delamination occurs. From these displacements, the interlayer nominal strain is deduced along a vertical line in the middle of the sample. The strain ϵ_{DIC} is normalized by the mean constant strain value ϵ^0_{TCT} previously measured. The distance to a point upright the delamination front position x_F (Figure 4.2) is normalized by the interlayer thickness h. In Figure 4.12, the normalized strain along the central vertical line is displayed as a function of the normalized delamination front position for two different thicknesses.

The interlayer deforms from 0% to 60% of $\epsilon^0_{\mathrm{TCT}}$ over a length close to the interlayer thickness (Part A of the curve). From the delamination front velocity, one can deduce that the average strain rate in this region is approximately $3\,\mathrm{s}^{-1}$. After this sharp increase of the strain, the polymer reaches the steady state strain at a much slower pace with a strain rate being close to $0.5\,\mathrm{s}^{-1}$. We know from our previous results that eventually, far from the delamination front, the polymer reaches a constant strain of the order of the mean value $\epsilon^0_{\mathrm{TCT}} = 1.4$. In this zone, no more energy will be dissipated. This region is not easily accessible, with the same spatial resolution. A zoom out will be required to measure the strain using DIC, far from the delamination fronts.

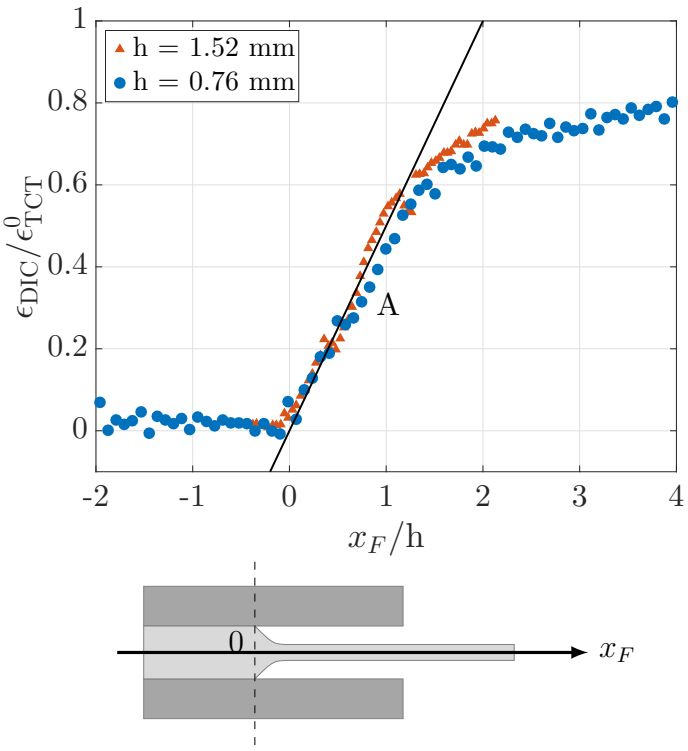

Figure 4.12: Local strain measurement through digital image correlation at 20 °C and $10\,\mathrm{mm\,s}^{-1}$. Two thicknesses h were tested. x_F is the position to the point upright the delamination front. Two strain rate regimes are identified ahead of the position uprigth the delamination front $x_F/h = 0$. The first regime spans over a length close to the interlayer thickness.

4.4.3 Dependence of the fast stretching zone length on applied velocity and temperature

The same DIC experiment can be conducted at different velocities and different temperatures.

The experiment has first been conducted at 20 °C for three different velocities 10 mm s^{-1}, 30 mm s^{-1} and 60 mm s^{-1}. As the imposed velocity increases, the delamination front velocity also increases. Thus we found three different delamination front velocities 4 mm s^{-1}, 10 mm s^{-1} and 19 mm s^{-1}. The local strain was plotted as a function of the delamination front distance in Figure 4.13(a). The amplitude of the strain seems to be identical in each case leading to the same ϵ_{TCT} far from the delamination front. This could mean that the mean constant strain ϵ_{TCT} does not change with the velocity at 20 °C unlike what was seen in the previous part 4.9, where the strain seemed to increase with the applied velocity from 1.2 to 2. The deformation occurs on the same length, which is approximately the thickness of the interlayer as described before. This implies that the deformation of the interlayer occurs at different strain rates. In Figure 4.13(b) the local strain is now plotted as a function of time. The continuous lines have a slope close to the theoretical values calculated by $\dot{\epsilon} = \epsilon^0_{\mathrm{TCT}}/h.V_{front}$. The different strain rates found here are 3 s^{-1}, 4 s^{-1} and 5.2 s^{-1} for the different imposed velocities respectively.

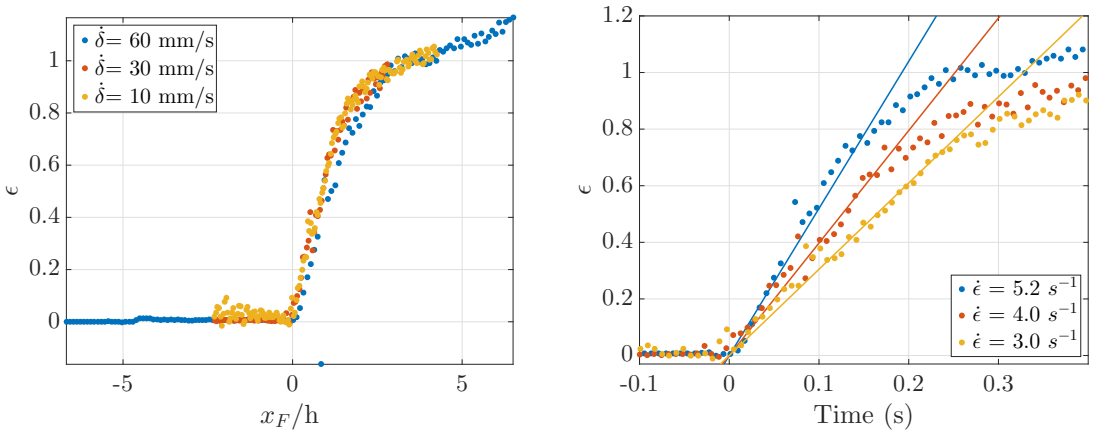

(a) (b)

Figure 4.13: DIC experiment conducted during a TCT test at 20 °C and three different imposed velocities 10 mm s^{-1}, 30 mm s^{-1} and 60 mm s^{-1}. (a) The deformation length does not depend on the imposed velocity. (b) The strain rate increases as the imposed velocity is increasing.

The DIC experiment was also performed for different temperatures: 5 °C, 20 °C and 50 °C at 30 mm s^{-1}. As the steady state delamination regime is highly affected

by the temperature it was hard to find a velocity at which the delamination was stable for the three temperatures. The following results have to be taken with care and more experiments might be required to validate this result. In Figure 4.14 the strain is plotted as a function of the distance to the delamination front. At 50 °C, a transient negative strain is observed in the front neighborhood. This effect has been observed twice at this temperature on two different specimens. As this region corresponds to the passage of the dark line of the delamination fronts, it could either be an artifact from the image correlation process or due to the undulation of the fronts.

Nevertheless, it can be seen that the deformation length scale is equal to the interlayer thickness at 20 °C and 50 °C. At 5 °C, this length is closer to twice the interlayer thickness.

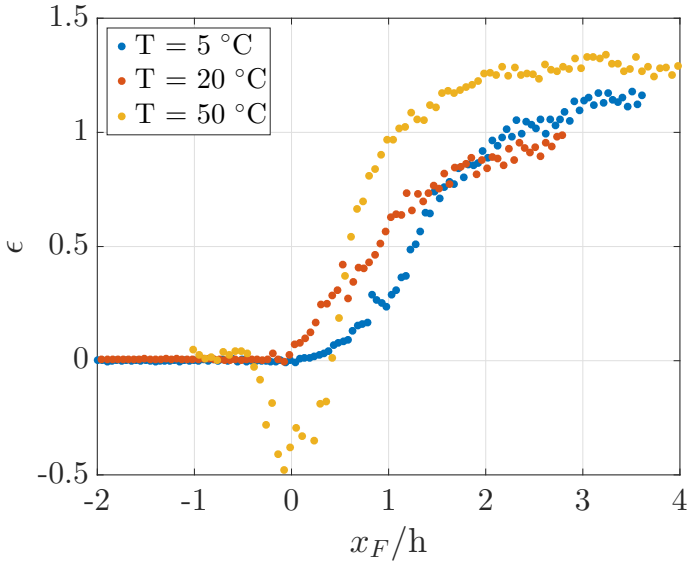

Figure 4.14: Local strain measurements at 30 mm s^{-1} and three different temperatures 5 °C, 20 °C and 50 °C.

4.5 Conclusion

During the delamination of the interlayer from glass, a steady state regime can be reached in a certain range of temperature and velocity. In this regime, the delamination force and strain reach a constant value both in time and space far from the delamination front. At lower temperatures or higher velocities, the interlayer is more susceptible to failure and displays a brittle behavior. At higher temperatures or lower velocities the delamination is unstable and the front starts to undulate.

The plateau values reached by both the delamination force and strain are related to a complex combined effect of the interlayer rheology and of the adhesion. The increase of the delamination force with the increasing velocity or decreasing temperature is similar to the increase in force observed in the rheology of viscoelastic polymers. The variations displayed by the interlayer strain are more counter intuitive. It can not be directly related to the interlayer behavior. Indeed, the strain seems to increase with the applied velocity but it also increases with the temperature which is not a common behavior for polymer materials. The strain level might be related to a combination of a change in adhesion with the temperature and the variations of the strain hardening presented by the interlayer at large strains (Section 3.3.2).

Finally, we have seen that the deformation of the interlayer is occurring over a length which is approximately its thickness. On this length it undergoes a deformation from 0 to 60% of the constant nominal strain value $\epsilon^0_{\mathrm{TCT}}$. This length does not depend on the imposed velocity and seems to be stable with the temperature (though this last result has to be confirmed). Thus, the strain rate can be determined knowing the delamination front velocity, the mean nominal strain $\epsilon^0_{\mathrm{TCT}}$ (two parameters that depend on the velocity and the temperature) and the interlayer thickness. Here we have found strain rates ranging from $3\,\mathrm{s}^{-1}$ to $5.2\,\mathrm{s}^{-1}$ for applied velocities in between $10\,\mathrm{mm\,s}^{-1}$ and $60\,\mathrm{mm\,s}^{-1}$.

We are now going to use these results to evaluate the dissipated energy during the delamination.

Main results

- Steady state delamination regime.
  - At intermediate velocity and temperature: symmetric and steady delamination
  - At high velocity or low temperature: symmetric delamination but brittle interlayer.
  - At low velocity or high temperature: unstable delamination and fronts undulates.
- The interlayer is stretched from 0% to $\approx \epsilon^0_{\mathrm{TCT}}$:
  - In a *fast stretching zone*, which length is close to the interlayer thickness, the interlayer is stretched to 60% of $\epsilon^0_{\mathrm{TCT}}$.
  - In an intermediate zone, the interlayer is stretched more slowly to the maximal nominal strain
  - The interlayer reaches a constant nominal strain value far from the delamination front where the strain rate is null

Chapter 5

Energy dissipation during delamination

5.1 Introduction

During the delamination, we have seen that the interlayer deforms over a length equal to its thickness equal at 0.76 mm. At 20 °C, the fronts propagate at high velocities of about $3\,\mathrm{mm\,s^{-1}}$ and the interlayer is stretched up to 140% nominal strain. Consequently, the strain rates that are applied on the polymer are about $3\,\mathrm{s^{-1}}$. These high strain rates, on a 0.76 mm thick volume, could involve a large amount of dissipated energy despite the weak hydrogen bonded interface.

In the literature, this large amount of dissipated energy during the propagation of a crack inside a viscoelastic material or at the interface between a viscoelastic polymer and a rigid substrate has been a long time puzzling problem. During the fracture of a viscoelastic material, even if the rupture of chemical or physical bonds only requires $0.01\,\mathrm{J\,m^{-2}}$ to $0.1\,\mathrm{J\,m^{-2}}$, huge macroscopic fracture energy of the order of $1\,\mathrm{kJ\,m^{-2}}$ are generally recorded. *Schapery* describes the crack tip has a region in which the interlayer behavior is strongly non-linear and viscoelastic [37]. *De Gennes* [38] suggested in his trumpet model that because of the time dependence of the polymer behavior, there were different dissipation zones ahead of the crack tip. Later *Saulnier et al.* in [39] have shown that this simple linear viscoelastic description of the material can explain the large enhancement of the dissipated energy observed during the crack propagation. However, Gent [40] used the same viscoelastic time dependence for the energy release rate to show that it leads to a dissipation zone at the crack tip with an unrealistic size, close to 1 Å. As explained

by *Barthel et al.* in [41] the coupling between the remote loading and the crack tip dissipation phenomenon is done through an intermediate viscous/large strain dissipation zone. According to *Creton et al.* [42], this could explain both the high level of dissipation and a larger crack tip process zone. *Newby* [43] and *Amouroux* [44] have shown that for weak interfaces, energy dissipation is low and dominated by interfacial slippage. A strong enough interface is required to stretch the polymer and dissipate large amounts of energy.

First, the delamination experiment results will be used to determine the macroscopic work of fracture. Then we will see how this work is related to the stretching of the interlayer. Finally, we will provide a model of the delamination and the stretching of the interlayer, which will enable a calculation of the dissipated energy.

5.2 Macroscopic work of fracture

The interlayer is stretched to large nominal strains ranging from 100 to 200% during the delamination. We have seen that a large amount of the work provided to stretch the interlayer is dissipated (see 3.3.2). The macroscopic work of fracture provided during the delamination experiment is either stored elastically in the debonded interlayer or dissipated when this part of the interlayer is stretched. Finally, only a small amount of energy will reach the delamination front to break the interface.

Using the previous measurements at different temperatures and different applied velocities, one can first evaluate the macroscopic work of fracture provided in the TCT test. The total macroscopic work of fracture is defined by:

$$G_{m,total} = \frac{1}{w}\frac{\mathrm{d}W_{\mathrm{TCT}}}{\mathrm{d}a} = \frac{1}{w}F_{\mathrm{TCT}^0}\frac{\mathrm{d}\delta}{\mathrm{d}a} = \frac{1}{w}2F_{\mathrm{TCT}^0}\epsilon_{\mathrm{TCT}^0} \tag{5.2.1}$$

where W_{TCT} is the work provided to the system during the delamination.

For symmetry reasons we are only interested in half the sample. Thus we will define the macroscopic work of fracture during the steady state delamination as:

$$G_m = \frac{F^0_{\mathrm{TCT}}}{w}\epsilon_{\mathrm{TCT}^0} \tag{5.2.2}$$

Using the data from Figure 4.8 and Figure 4.9 G_m has been calculated (Figure 5.1). It is found to increase with increasing loading speed and decrease with increasing temperature. More specifically, as the velocity increases from $1\,\mathrm{mm\,s^{-1}}$ to $60\,\mathrm{mm\,s^{-1}}$, G_m increases from $7\,\mathrm{kJ\,m^{-2}}$ to $26\,\mathrm{kJ\,m^{-2}}$ at $20\,^{\circ}\mathrm{C}$. The increase in

temperature from 5 °C to 50 °C at 10 mm s^{-1} leads to a dramatic decrease in G_m from 22 kJ m^{-2} to 3 kJ m^{-2}.

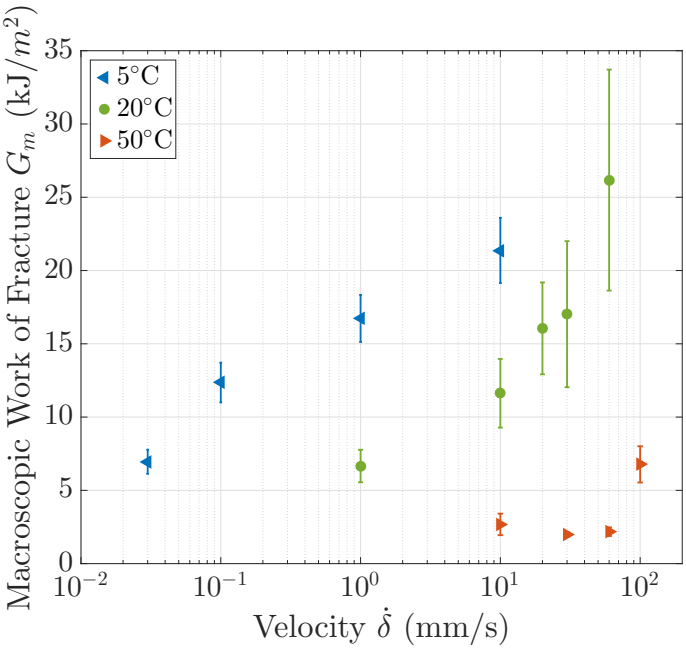

Figure 5.1: Impact of the velocity and temperature on the macroscopic work of fracture.

5.3 Impact of the interlayer thickness

The steady state value of the nominal strain found in previous experiments (see section 4.4.1 and following), was shown to be reached rapidly over a length scale equal to the interlayer thickness. The influence of this thickness on the TCT Test response was studied. Four different interlayer thicknesses were used: 0.38 mm, 0.76 mm, 1.14 mm and 1.52 mm. A TCT Test was conducted on each of them at T =20 °C and $\dot{\delta}$ =10 mm s^{-1} in the steady state delamination regime. The increase in the interlayer thickness leads to a proportional increase in the measured force (F^0_{TCT}) from 220 N to 710 N, while the interlayer strain ($\epsilon^0_{\mathrm{TCT}}$) decreases slightly from 1.4 to 1.2 (Figure 5.2).

The dissipated energy is thus increasing from 7 kJ m^{-2} to 16 kJ m^{-2} as the thickness increases from 0.38 mm to 1.52 mm (Figure 5.3). This increase is linear with a slope Π_{bulk} equal to 8 MJ m^{-3} and a non-null intercept $2\Gamma_{crack}$ equal to 4 kJ m^{-2}.

i

This interlayer thickness dependence also reflects that the initial transient regime during which the force and strain increase, only lasts the time for a length equivalent

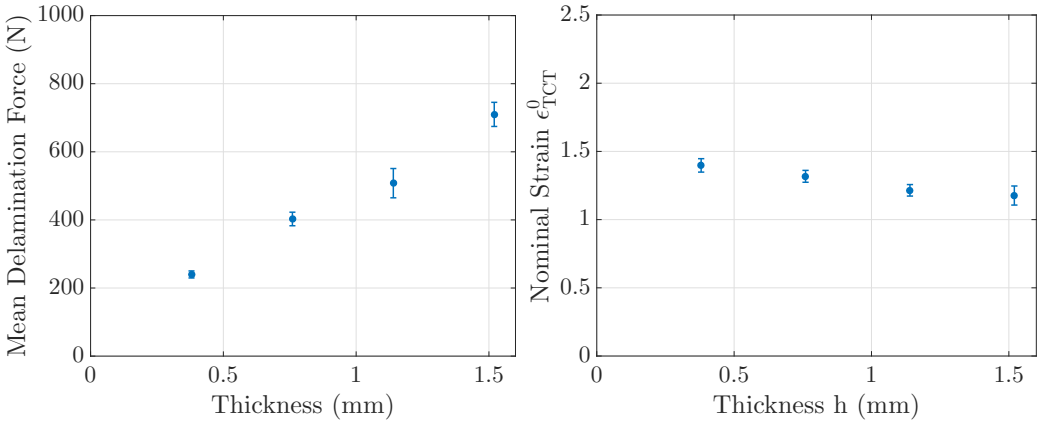

(a) Delamination force (b) Delamination Strain

Figure 5.2: Impact on the delamination force and the interlayer stretch of the interlayer thickness. Four thicknesses were tested 0.38 mm, 0.76 mm, 1.14 mm and 1.52 mm.

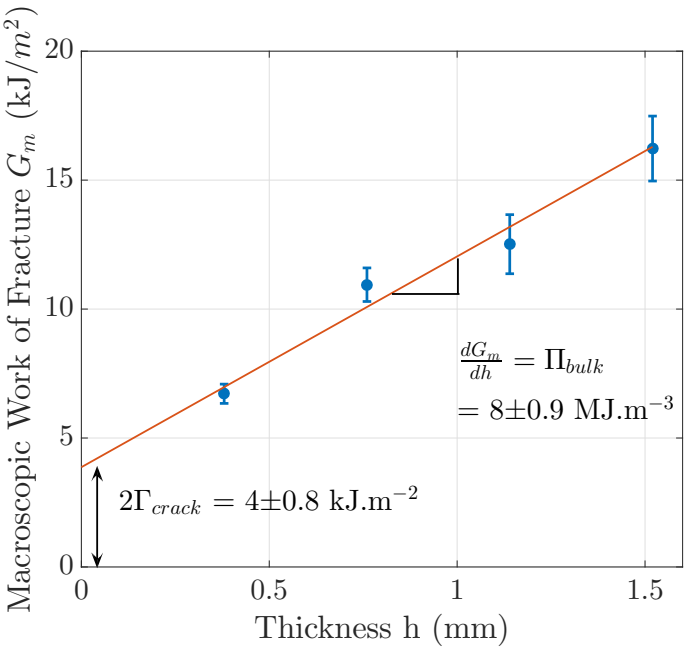

Figure 5.3: Effect of the interlayer thickness on the macroscopic work of fracture.

to the interlayer thickness to be delaminated. This can be seen in Figure 5.4 where the delamination force is plotted as a function of the delamination length normalized by the interlayer thickness. The steady state starts for the same normalized length 1 for the four thicknesses.

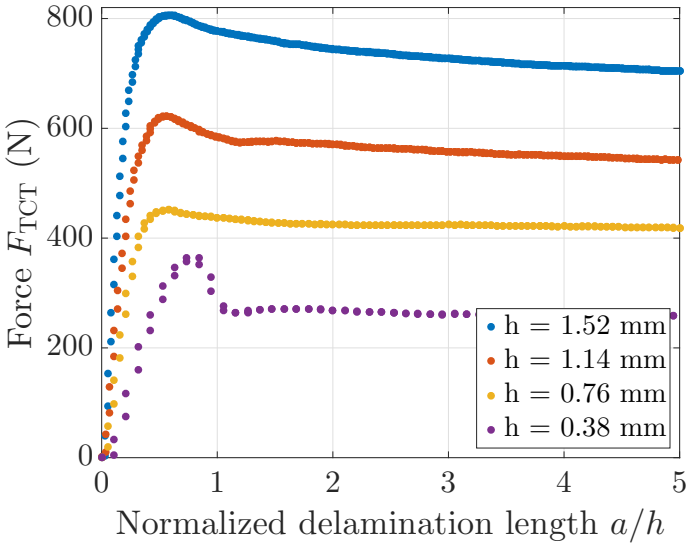

Figure 5.4: The force is plotted as a function of the delamination length normalized by the interlayer thickness. The transitory regime only last until a length equal to the interlayer thickness is delaminated.

5.4 Different zones of dissipation

The dissipation processes leading to the large macroscopic work of fracture are not homogeneous in the interlayer. G_m was found to be an increasing linear function of the interlayer thickness (Figure 5.3).

In analogy with the method of the Essential Work of Fracture [45], we can tentatively separate the bulk stretching work due to the deformation of the interlayer from a near crack work of fracture, which includes the interfacial bond rupture between the interlayer and the glass and the dissipation due to the stretching of the interlayer close to the delamination front. The Near crack work of fracture will depend on the loading mode mixity and on the interlayer confinement, but in the explored range of interlayer thickness, it does not depend on the thickness (equation 5.4.1). Hence, on Figure 5.3 the slope of the line gives the volumic dissipation density (Π_{bulk}) related to the bulk stretching mechanisms: $\Gamma_{bulk} = \Pi_{bulk} h$. The intercept gives near crack work of fracture: Γ_{crack} (per unit area). For half a sample we can write:

$$G_m = 2\Gamma_{crack} + \Pi_{bulk} h \tag{5.4.1}$$

After the fast stretching zone, the polymer undergoes some deformation at a much slower pace. Because of the lower strain rate and of the smaller strain amplitude in this third deformation phase, this contribution to the macroscopic work of fracture should be much smaller than in the previous zones. Eventually, far from the delamination front the polymer finally reaches a constant level of nominal strain. In this last zone, the energy is only stored elastically and its volume density is constant, no energy will be dissipated.

Hence in the steady state delamination regime we have shown that there is several dissipation zones (Figure 5.5):

- Close to the delamination front, a near crack dissipation zone. This zone is experimentally out of our reach because of its small size.

- Ahead of this zone, we have found a fast stretching zone the length of which is equal to the interlayer thickness. The polymer undergoes a large change of strain at high strain rate leading to a large amount of dissipated energy.

- An intermediate zone, in which the interlayer is stretched up to the steady state value of strain at a much slower pace, leading to lower energy dissipation.

- Finally far from the delamination fronts, there is a constant nominal strain zone where no energy is dissipated.

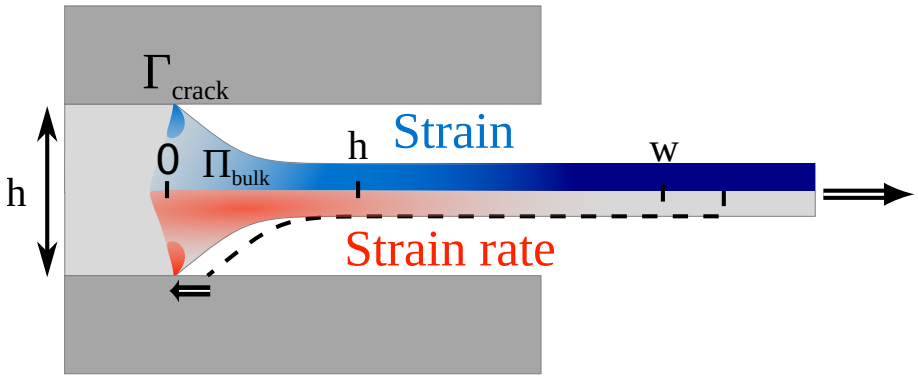

Figure 5.5: Far field/Delamination front link and energy dissipation

5.5 Modeling the bulk stretching of the interlayer

An important part of the work occurs in the fast stretching zone. In this region, the interlayer is stretched mainly in uniaxial tension. Thus, a uniaxial tension test at the appropriate strain rate could be an easy way to estimate the amount of dissipated energy in the TCT test. This final part of the discussion will focus on modeling the fast stretching zone.

The volume of polymer involved in the stretching of the interlayer as the front advances a distance da has to be evaluated in order to estimate the amount of energy dissipated during the delamination. The remote displacement dδ is applied with a constant loading velocity $\dot{\delta}$ that corresponds to a constant measured force F^0_{TCT} while the four fronts will simultaneously move a distance da. As described before, the delamination fronts are moving at a constant velocity and the following relationship can be written:

$$\mathrm{d}a = V_{\mathrm{front}}\mathrm{d}t \approx \frac{2}{\epsilon_{\mathrm{TCT}}}\mathrm{d}\delta \tag{5.5.1}$$

where V_{front} is the delamination front velocity and dt is a small time increment.

The interlayer in the volume $wh\mathrm{d}a$ will first pass above the delamination fronts and then will overcome the large deformation process in the fast stretching zone. Thus, in a steady state regime for all the fronts to advance by da, the total macroscopic energy is:

$$\mathcal{E}_{tot} = 2G_m w\mathrm{d}a = 2\left(2\Gamma_{crack} w\mathrm{d}a + \Pi_{bulk} wh\mathrm{d}a\right) \tag{5.5.2}$$

It is possible to estimate the volumic density of the bulk stretching work from a simple uniaxial tension curve. In this zone the polymer is stretched from 0 to a strain of 0.8 (60% of 1.4 see 4.12) at $3\,\mathrm{s}^{-1}$. Hence, the bulk stretching work density is given:

$$\Pi_{calculated} \approx \int_0^{f_{\mathrm{TCT}}*\epsilon_{\mathrm{TCT}}} \sigma_{\mathrm{T}}\ d\epsilon_{\mathrm{T}} \tag{5.5.3}$$

With σ_T and ϵ_T the stress and strain values measured during the uniaxial tension test. f_{TCT} is the fraction of the constant mean nominal strain value ϵ_{TCT} reached by the interlayer in the fast stretching zone. Here f_{TCT} is about 60% of ϵ_{TCT}.

This yields $\Pi_{calculated} \approx 9\,\mathrm{MJ\,m^{-3}}$ which is comparable to the value of $8\,\mathrm{MJ\,m^{-3}}$ found by our previous measurements in Figure 5.3.

5.6 Dissipated energy

The interlayer stretching, in the fast stretching zone, is approximately a uniaxial tension. The dissipated energy can be evaluated from the macroscopic work of fracture as if the delamination was a uniaxial tension test. In section 3.3.2, we have defined a dissipated energy ratio R_d for the uniaxial tension test. This ratio can be applied to the macroscopic work of fracture to estimate the dissipated energy:

$$G_{diss} = R_d * G_m = R_d * \frac{F_{\mathrm{TCT}}}{w}\epsilon_{\mathrm{TCT}} \tag{5.6.1}$$

However, this ratio depends both on velocity and temperature as displayed in Figure 3.17. The strain rate in the TCT test was found to be about $3\,\mathrm{s}^{-1}$ in the fast stretching zone. This strain rate is higher than the faster strain rate reached during the uniaxial cyclic traction tests. Thus, in order to estimate the dissipated energy in the TCT test, the R_d ratio for the $1\,\mathrm{s}^{-1}$ at each temperature will be used. This will lead to an underestimate of the dissipated energy. At 20 °C, the dissipation ratio will be R_d =85%. Obviously, this high value reflects the fact that most of the macroscopic work of fracture is used to overcome the visco/plastic dissipation in the stretching of the interlayer. The value of R_d is close to 90% at 10 °C but drops at 40% at 50 °C.

5.7 Influence of the temperature and applied velocity on the dissipation mechanism

In order to look at the influence of the applied velocity and temperature on the near crack work of fracture and on the bulk stretching work, the TCT test was conducted with four different interlayer thicknesses 0.38 mm, 0.76 mm, 1.14 mm and 1.52 mm in different conditions. At 20 °C, four applied velocities $1\,\mathrm{mm\,s}^{-1}$, $10\,\mathrm{mm\,s}^{-1}$, $20\,\mathrm{mm\,s}^{-1}$ and $30\,\mathrm{mm\,s}^{-1}$ were used (Figure 5.6(a)). Similarly at $10\,\mathrm{mm\,s}^{-1}$, four different temperatures 10 °C, 20 °C, 30 °C and 50 °C were tested (Figure 5.6(b)).

The raw data displayed in 5.6 are difficult to read. However in every case, the increase of the macroscopic work of fracture with the interlayer thickness is linear. Thus the slope and the extrapolated intercept at zero thickness can be extracted from the raw data for a better visualization (Figure 5.7). The results at 30 °C and $10\,\mathrm{mm\,s}^{-1}$ are subjected, for an unknown reason, to large error bars. It is possible that sample preparation was affected by some spurious effect. These experiment

should be repeated before full conclusions can be reached. Thus the slope and the non-zero intercept extracted from these results do not give the same trends as the others.

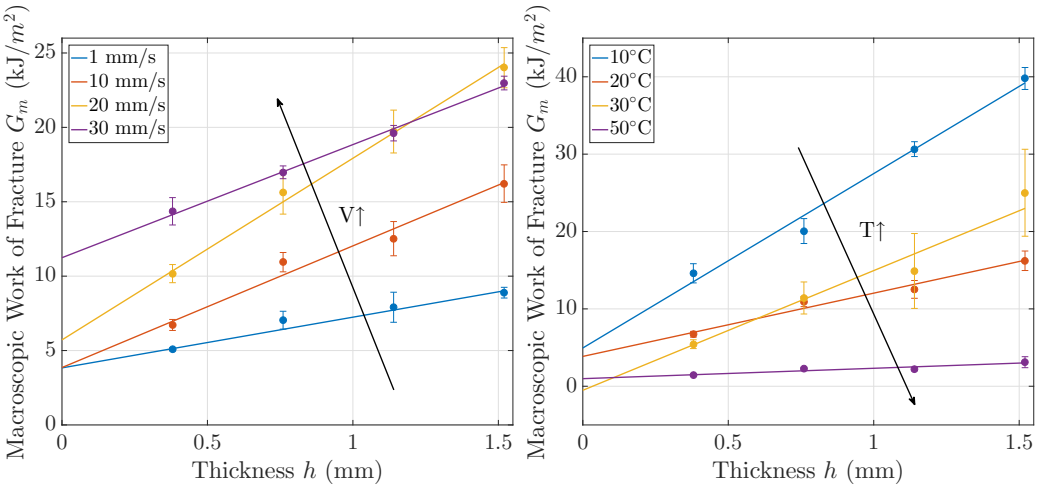

(a) Effect of the velocity (b) Effect of the temperature

Figure 5.6: Effect of the velocity and the temperature on the macroscopic work of fracture with the interlayer thickness. (a) Four temperatures 10 °C, 20 °C, 30 °C and 50 °C were tested for a given velocity of 10 mm s^{-1}. (b) Four velocities 1 mm s^{-1}, 10 mm s^{-1}, 20 mm s^{-1} and 30 mm s^{-1} were tested at 20 °C.

In Figure 5.7(a), $2\Gamma_{crack}$ increases from 4 kJ m^{-2} to 11.5 kJ m^{-2} when the applied velocity increases at 20 °C. At low speed however, the intercept reaches a plateau value of 4 kJ m^{-2}. Similarly $2\Gamma_{crack}$ seems to increase from 1 kJ m^{-2} to 5 kJ m^{-2} when the temperature decreases from 50 °C to 10 °C at a given velocity of 10 mm s^{-1} (the non physical negative result found for 30 °C is discarded).

In Figure 5.7(b), Π_{bulk} is increasing first with applied velocity at 20 °C from 3.5 MJ m^{-3} to 10 MJ m^{-3}, but decreases to 8 MJ m^{-3} for the higher velocity. Finally, the slope displays a global increase from 1 MJ m^{-3} to 23 MJ m^{-3} when the temperature decreases from 50 °C to 10 °C at a given velocity 10 mm s^{-1}. Again, Π_{bulk} is higher at 30 °C than at 20 °C.

Due to the difficult reproducibility of some of these experiments, we only discuss their global trends. We can conclude that the near crack work of fracture increases when the velocity increases and when the temperature decreases. The same trends are observed for the volume density of the bulk stretching work.

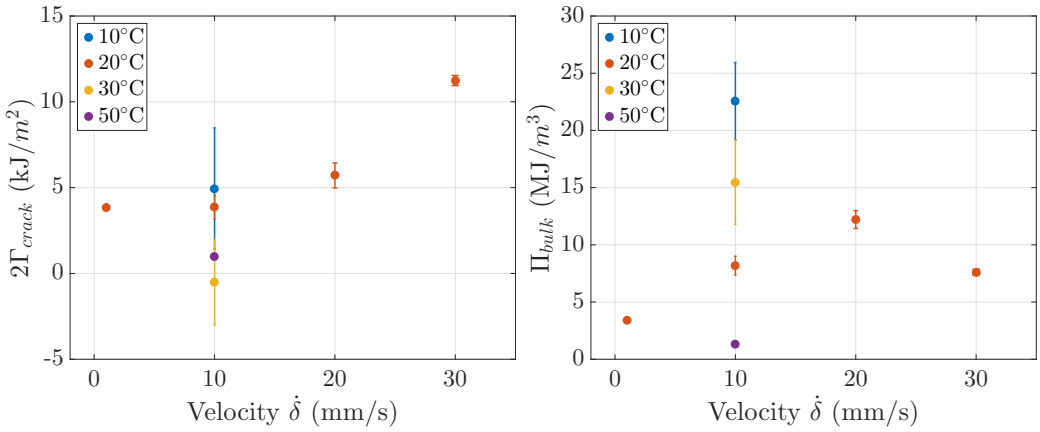

(a) Near crack work of fracture

(b) Bulk stretching work density

Figure 5.7: Effect of the velocity and temperature on (a) the near crack work of fracture $2\Gamma_{crack}$ and (b) the bulk stretching work density Π_{bulk}.

5.8 Discussion and Conclusion

We have shown that the macroscopic work of fracture provided during delamination is used to stretch the interlayer up to a mean nominal strain ϵ^0_{TCT}. This stretching results in a stored elastic energy in the delaminated part of the interlayer but also involves a large amount of dissipation. We have shown that the energy dissipation occurs in two main zones. In the fast stretching zone, the interlayer is stretched up to 60% of ϵ^0_{TCT} over a length equal to the interlayer thickness. We have shown that this fast stretching region can be modeled by a uniaxial tension test on the interlayer alone. This test can be used to estimate the volume density of the bulk stretching work Π_{bulk}. This rough evauation gives a value ($9\,\mathrm{MJ\,m^{-3}}$ at $20\,^\circ\mathrm{C}$ and $1\,\mathrm{s^{-1}}$) which compares favorably with the experimental results ($8\,\mathrm{MJ\,m^{-2}}$ at $20\,^\circ\mathrm{C}$ and $10\,\mathrm{mm\,s^{-1}}$). The remaining energy goes to the near crack region where a non negligible amount of energy is also dissipated Γ_{crack}. This energy corresponds to a local deformation of the interlayer and to the rupture of the interfacial bonds. This zone can not be reached experimentally due to its small size. However, the large amount of dissipated energy in this zone could be related to the large strain and strain rates that are expected to be found close to the crack tip. This hypothesis will be studied thanks to a finite element model in the final part of this study.

The description of the problem that arises at this point enables us to understand qualitatively the variation of the delamination force observed during the TCT test. Indeed, the delamination can be related to a uniaxial tension test. Moreover, at a given temperature, the strain $\epsilon^0_{\mathrm{TCT}}$ is constant with the applied velocity (Figure

4.9). Thus, the delamination force increases with applied velocity as observed in the rheology of the interlayer (Figure 3.12). However, to predict the level of strain reached by the interlayer the coupling between the stretch region and the near crack region must be considered. This will question be tackled in the next chapters.

We might also be able to explain the different delamination regimes, described in Chapter 4. At high temperatures and low velocities, the macroscopic work of fracture is much smaller as the polymer is softer. Moreover, as the relaxation time of the polymer are closer to the experimental time, the polymer can relax between the remote loading point and the delamination front. This means that both the energy needed for the front to propagate and the stress to break the interface, are smaller. This could explain why the front buckles and that its propagation stops leading to failure. At higher velocity, even if the delamination conditions are fulfilled, the polymer becomes more brittle and more sensitive to initiation of defects resulting from the sample preparation or clamp misalignment. However, in this high velocity regime, the delamination process should not be different from the ones described in the intermediate regime.

The estimation of the dissipated energy that can be done using the ratio of dissipated energy from the cyclic uniaxial tension experiments is of great interest in order to predict, the laminated glass resistance to impact. Considering this ratio is close to 1 at 20 °C and for strain rates higher than $1\,s^{-1}$, the values of the macroscopic work of fracture already give a good approximation of the dissipated energy.

Finally, the variations displayed by the near crack work of fracture and bulk stretching work density with the temperature and the applied velocity require more experiments to confirm the trends described previously.

Main results

- The macroscopic work of fracture can be divided in different components:
  - A bulk stretching work which is:
    - For a small part, stored as elastic energy in the stretched interlayer
    - For the main part, dissipated in the fast stretching zone
  - A near crack work of fracture which corresponds to dissipated energy due to the deformation of the interlayer in the delamination front vicinity
  - A separation work which corresponds to the energy required to break the hydrogen bonds at the interface
- The bulk dissipation in the fast stretching zone can be modeled thanks to a uniaxial tension test at the appropriate strain rate.

Chapter 6

Interface modification – Preliminary results

6.1 Introduction

In the previous parts, a description of the delamination mechanisms was provided. A steady state delamination regime was identified in a certain range of temperature and applied velocity. Two different dissipation energies were measured in this regime. In order to push further our understanding of the near crack dissipation mechanisms and in the bulk of the interlayer during delamination, the impact of the interface on these processes is investigated.

In order to change the work of separation, namely the molecular adhesion of the interlayer onto glass, without altering its rheological properties, silanization of the glass surface was used. This work has been conducted together with *Raphaelle Kulis*. The silanization process will not be discussed here. It has been thoroughly described by *R. Kulis* in her report [13]. The effect of silanization was first quantified by peel experiments. Then, the weaker and stronger interfaces were tested in the TCT experiment. We show that a change in adhesion affects the steady state delamination regime. In the case of the stronger interface no delamination is observed whereas for the weaker interface, it is possible to find a range of temperature and applied velocity in which the delamination occurred in a steady state manner. This enabled to study the effect of a decrease in the adhesion on the macroscopic work of fracture and its different components.

6.2 Impact of silanization on the interface and on the peel work of fracture

In order to get a weaker and stronger interface without changing the bulk properties of the interlayer (see section 3.3.2), two silanes were used: (3-aminopropyl) triethoxysilane (APTS) was used to enhance molecular adhesion while triethoxy(octyl)silane (OTES) was used to reduce it (see 2.2). APTS is known to increase the molecular adhesion between glass and PVB [46] due to its amphiphilic nature. Indeed, the silanol group can attach on the glass surface (through a complex mix of hydrogen bonds, electrostatic interactions and covalent bonds) and the amino group can form bonds with the hydroxyl groups of the PVB interlayer. On the other hand, OTES can similarly attach to the glass surface by mainly covalent bonds with the glass silanols, but the long hydrophobic chain will reduce interactions with the PVB interlayer, thus decreasing adhesion [47] [48]. We will refer to these treated glass samples as OTES treated and APTS treated samples. The laminated glass samples without any surface treatment used previously will be referred to as non-treated samples and used as reference.

The impact of silanization on the interface was evaluated through 90° peel tests. A stiff backing is used on top of the PVB layer to prevent bulk stretching during the tests. These tests were performed at room temperature and two different traction velocities of $5\,\mathrm{mm\,min^{-1}}$ and $50\,\mathrm{mm\,min^{-1}}$. During the peel test, a constant force was measured (Figure 6.1). From this force level, the peel work of fracture was calculated: $G_c = \frac{F}{w}$. This work corresponds to both the rupture of the molecular bonds at the interface and to the stretching of the PVB near the crack tip. This peel work of fracture is plotted in Figure 6.2. From these two figures it appears clearly that the APTS and OTES treatments result in the expected changes of the interfacial adhesion.

At $5\,\mathrm{mm\,min^{-1}}$, APTS treatment leads to an increase in the mean peel force from $20\pm4\,\mathrm{N}$ to $71\pm8\,\mathrm{N}$ which corresponds, for a sample width of 2 cm, to an increase in the peel work of fracture from $0.97\pm0.2\,\mathrm{kJ\,m^{-2}}$ to $3.5\pm0.4\,\mathrm{kJ\,m^{-2}}$. At $50\,\mathrm{mm\,min^{-1}}$, the force increases from $41\pm5\,\mathrm{N}$ to $97\pm4\,\mathrm{N}$ which corresponds to an increase in the peel work of fracture of $2.1\pm0.25\,\mathrm{kJ\,m^{-2}}$ and $4.9\pm0.2\,\mathrm{kJ\,m^{-2}}$.

On the other way, OTES treatment leads to a decrease in peel force. At $5\,\mathrm{mm\,min^{-1}}$ the peel force decreases from $20\pm4\,\mathrm{N}$ to $3\pm1\,\mathrm{N}$. At $50\,\mathrm{mm\,min^{-1}}$ the peel force decreases from $20\pm4\,\mathrm{N}$ to $5\pm2\,\mathrm{N}$. This corresponds to lower values of the energy release rate of $0.17\pm0.05\,\mathrm{kJ\,m^{-2}}$ and $0.26\pm0.1\,\mathrm{kJ\,m^{-2}}$ respectively.

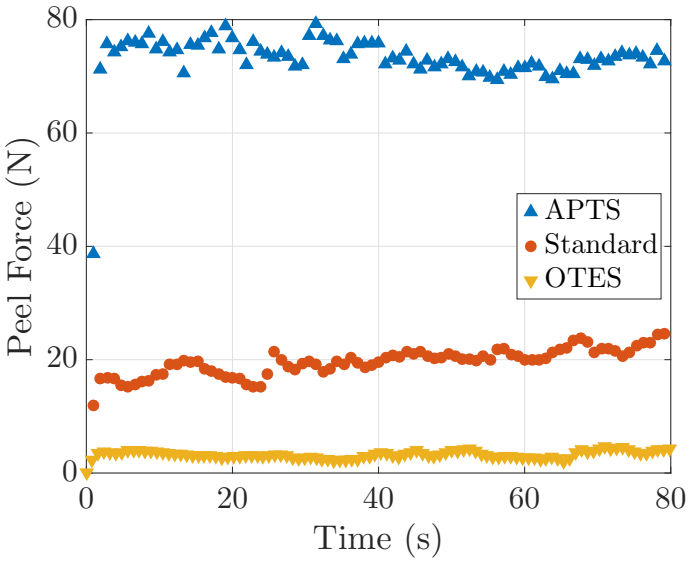

Figure 6.1: Peel force measured at 5 mm min^{-1}, at room temperature on non-treated PVB/Glass sample (without silane modification of the interface), on APTS treated sample (enhanced adhesion) and OTES treated sample (reduced adhesion).

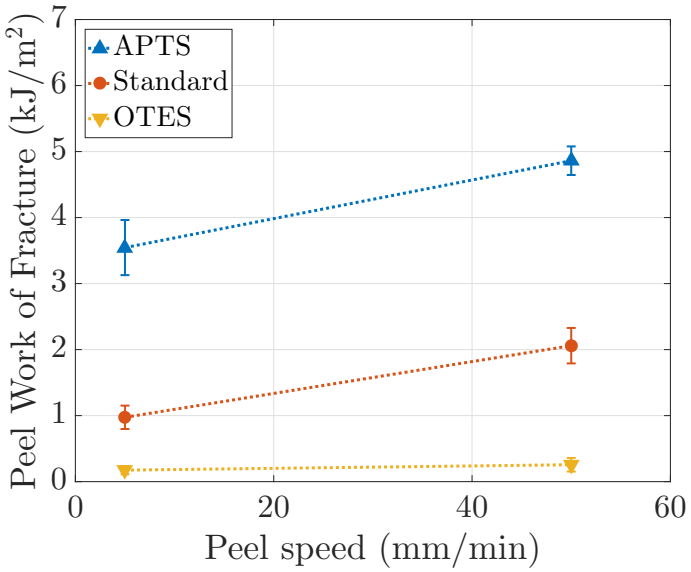

Figure 6.2: Peel work of fracture found in the peel test at two velocities 5 mm min^{-1} and 50 mm min^{-1} for the non-treated, OTES treated and APTS treated samples.

6.3 Impact of an interface modification on the TCT test response

6.3.1 Different steady state delamination regimes

Impact of the two silane treatments on adhesion being established, the modified surface were assembled with PVB interlayer and tested in TCT geometry. The samples with modified adhesion were first tested in the steady state regime found for the non-treated surface at 20 °C and 10 mm s^{-1}. We observed qualitatively different behaviors.

On APTS treated samples, no delamination was observed and the interlayer broke immediately (Figure 6.3(a)). On OTES treated samples, delamination was observed initially but the delamination front undulated and presented an unstable behavior. The delamination stopped and the polymer ruptured (Figure 6.3(c)). This behavior was similar to the one observed at high temperature or lower imposed velocities on the non-treated TCT sample.

For the OTES treated samples, the steady state delamination regime was recovered at higher velocities or at lower temperatures. It has been found at 20 °C for velocities higher than 30 mm s^{-1} that the delamination was stable. At 10 °C all the velocities tested in between 10 mm s^{-1} and 100 mm s^{-1} displayed stable delamination.

On the contrary, for the APTS treated samples, no delamination was observed for any of the temperature and the velocities applied.

Thus it appears that a weaker interface shifts the steady state delamination regime towards the lower temperature and higher velocities. Here, the increase in adhesion was too large to observe any delamination. A possible hypothesis is that the non-treated sample is already close to the upper limit of adhesion and that a small change of the interface results in the rupture of the interlayer prior to any delamination. This hypothesis could be tested by using different concentrations of the APTS solution or by using silane mixtures.

6.3.2 Steady state delamination for the lower adhesion

For the weaker interface the steady state delamination regime was tested for different velocities and temperatures.

Some general observations can be made first. The delamination fronts on the back glass and on the front glass were often not propagating at the same velocity.

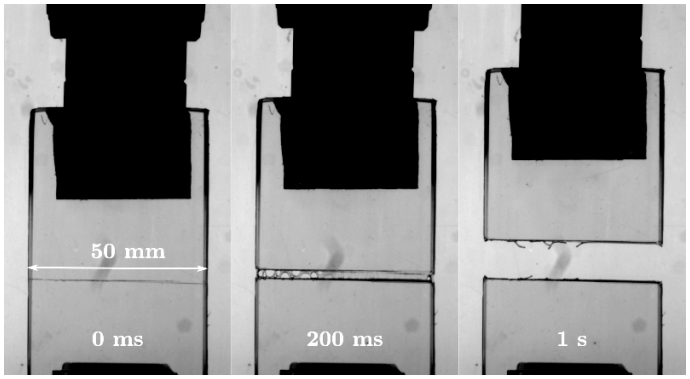

(a) APTS

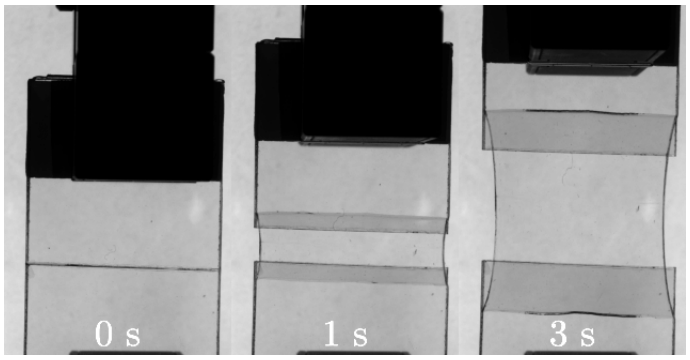

(b) Not treated

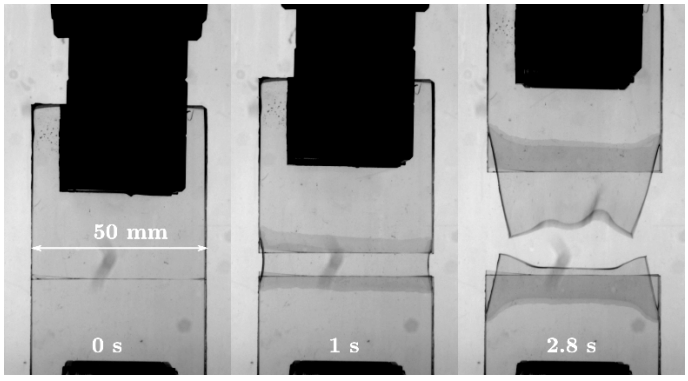

(c) OTES

Figure 6.3: The different behaviors observed during the TCT experiment at 20 °C and 10 mm s^{-1}. The APTS displays an immediate brittle rupture with no delamination, while the OTES shows delamination with unstable and undulating fronts before rupture.

Thus the two delamination fronts are visible as displayed in Figure 6.4. Furthermore, in some cases, an abrupt delamination occurred on one glass pane followed by a stable and steady state delamination on the other glass. At 10 °C and for an applied velocity of 20 mm s^{-1}, the abrupt delamination occurs at a velocity close to 200 mm s^{-1} and the slower delamination at a velocity about 30 mm s^{-1}. In the case where an abrupt delamination is observed, only the steady state delamination front was recorded and the measured strains and delamination forces were similar to steady state delaminations. The experiments conducted at 10 °C on the OTES samples are more reproducible than those conducted at 20 °C.

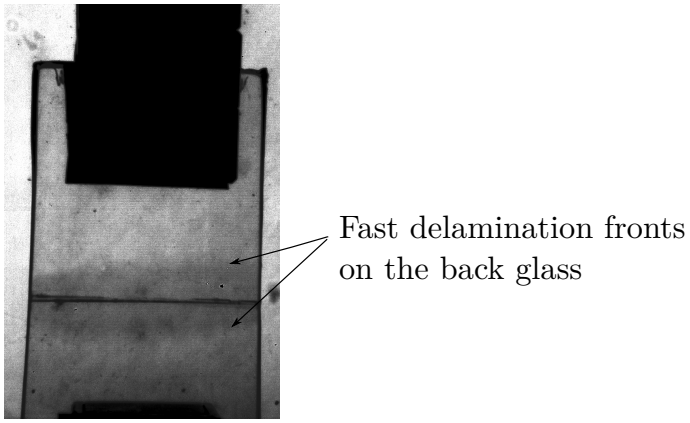

(a) Propagation after 25 ms

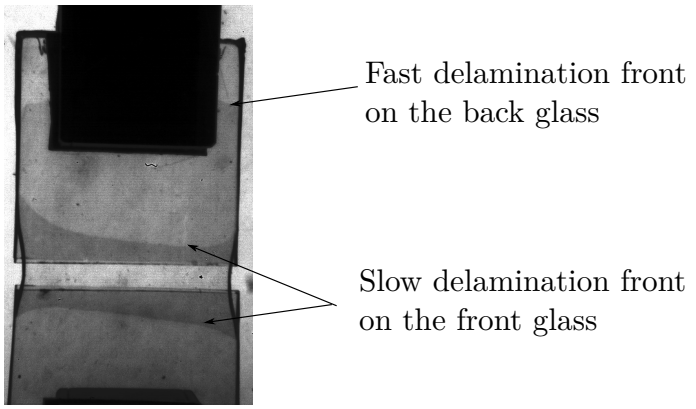

(b) Propagation after 850 ms

Figure 6.4: TCT test on an OTES treated sample at 20 mm s^{-1} and 10 °C. Sample width is 50 mm (a) Abrupt delamination on the back glass at a velocity close to 200 mm s^{-1}. (b) The second front propagates more "slowly" at a velocity about 20 mm s^{-1}.

In Figure 6.5, the delamination velocity, force and strain found for the different temperatures and velocities for the OTES samples are compared to the non-treated reference. First of all, the delamination occurs at a much faster velocity for the

OTES samples than for the non treated ones. The strain is found to be much lower for the OTES treated sample than for the non treated ones at a 20 °C for a given velocity. The force is similar at 20 °C for both the OTES and the non treated samples at 30 mm s^{-1} and 60 mm s^{-1}.

Similarly to what has been found for the non-treated samples (see Section 4.3), the force increases with the applied velocity and decreases with the temperature for the OTES samples. At 20 °C the force increases from 450 N to 600 N between 30 mm s^{-1} and 60 mm s^{-1}. The experiment at 100 mm s^{-1} can be questioned due to the fast breaking of the interlayer after a small stable delamination. At 10 °C the increase in force is clearer from 547 N to 847 N when the velocity increases from 10 mm s^{-1} to 100 mm s^{-1}. The strain does not display the same behavior as for the non treated sample. Indeed, if the strain increases with the velocity from 0.9 to 1.4, these values are not changing with the temperature unlike what we have observed for the non-treated sample strain (see Section 4.3). The delamination velocity displays the same trends. It increases from 5 mm s^{-1} to 32 mm s^{-1} at 20 °C as the applied velocity increases from 10 mm s^{-1} to 100 mm s^{-1} but it does not change much as the temperature decreases at 10 °C.

Due to the decrease of the strain, the macroscopic work of fracture is lower in the case of the weak adhesion at 20 °C. This effect is more visible as the velocity increases (Figure 6.6).

6.3.3 A change in the dissipated energies

The OTES treated glass can also be tested in the TCT test with different interlayer thicknesses. In Figure 6.7, three different thicknesses were tested in a reproducible manner (0.38 mm, 0.76 mm and 1.14 mm) at 10 °C and 30 mm s^{-1}. These conditions were chosen because they lie in the steady state delamination regime. However, the test is still difficult to perform as at this temperature and velocity the interlayer is sensitive to any experimental defect. Thus, only one point has been retrieved for the 1.52 mm thickness and one could argue that this result is not reproducible. If the first three points only are considered, the macroscopic work of fracture is found to be linear with the interlayer thickness as it was found for non treated sample. At this temperature and for this applied velocity, $2\Gamma_{crack}$ is about 9 kJ m^{-2} and Π_{bulk} about 5.2 MJ m^{-3}.

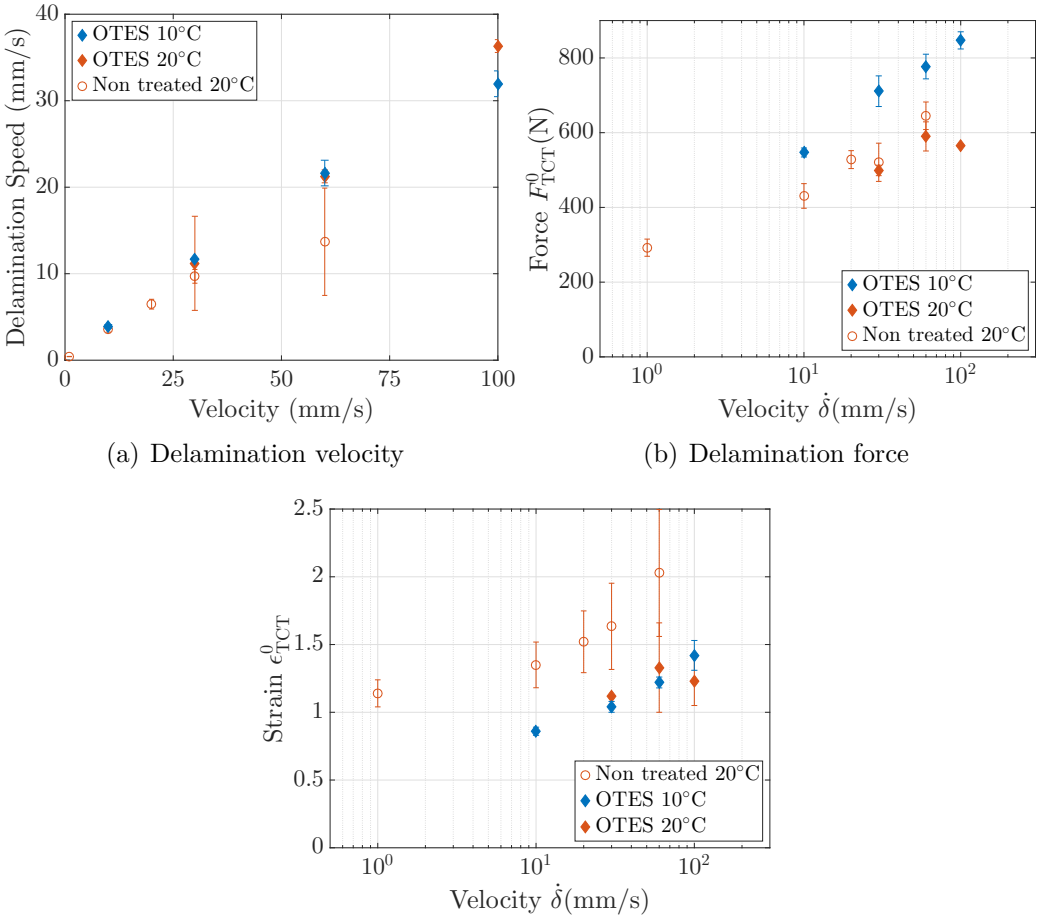

(a) Delamination velocity

(b) Delamination force

(c) Strain

Figure 6.5: The delamination velocity, force and strain measured during the TCT tests performed on the OTES treated samples at 10 °C and 20 °C compared, for different velocities, to the non-treated samples results found at 20 °C.

.

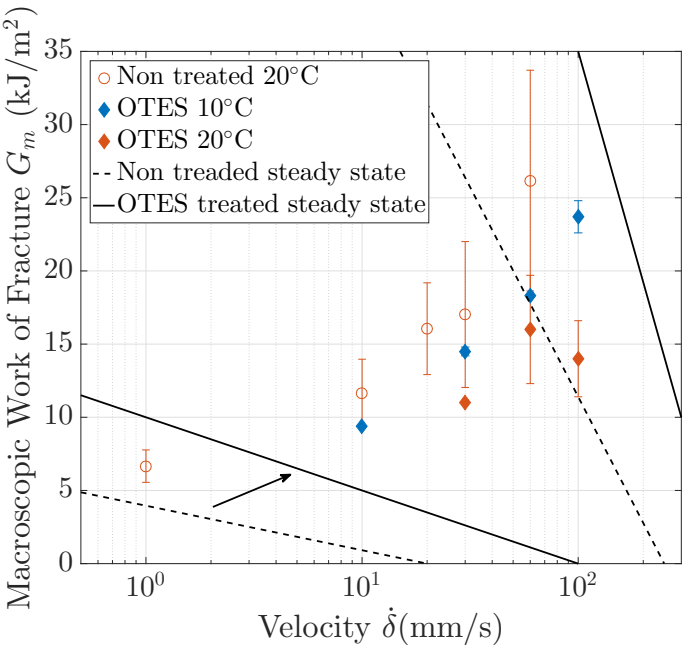

Figure 6.6: The macroscopic work of fracture during the TCT tests performed on the OTES treated samples at 10 °C and 20 °C compared, for different velocities, to the non-treated samples results found at 20 °C. The steady state delamination regime is shifted towards higher velocities and lower temperatures as the interface is weaker.

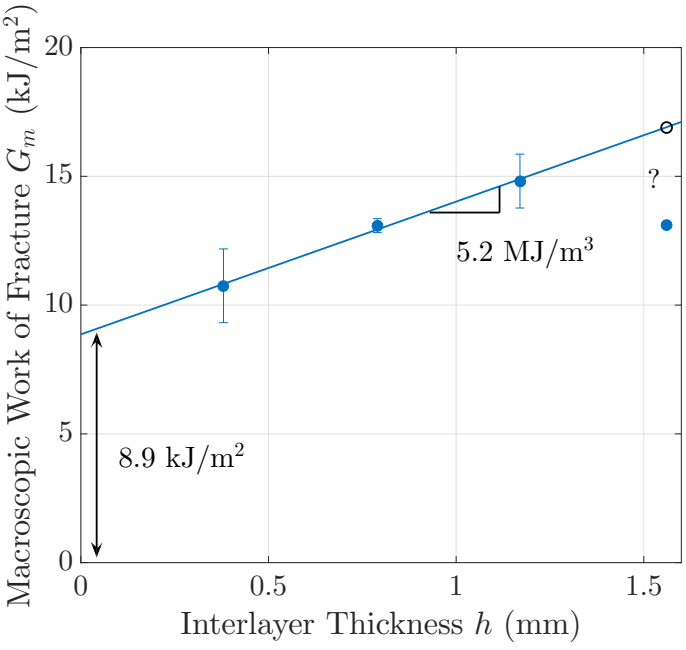

Figure 6.7: Dependence of the macroscopic work of fracture on the interlayer thickness during a TCT test performed on an OTES treated laminated glass at 10 °C and 30 mm s^{-1}.

6.4 Discussion

A change of the interface leads to a shift of the steady state delamination conditions as displayed in Figure 6.6. More specifically it was found that a weaker interface leads to a shift of the steady state delamination regime towards lower temperatures and higher velocities. One could assume that an increase of toughness will shift the steady state delamination regime towards higher temperatures and lower imposed velocities. However, this assumption has still to be verified. The increase of adhesion provided by the APTS treatment is too large to allow any delamination. One could reduce the APTS concentration to limit the increase in adhesion.

The decrease of the glass/interlayer adhesion due to the OTES treatment was compared to the previous results found on the non-treated samples in terms of force and strain during the delamination. It leads to the conclusion that a weaker interface is responsible for a lower macroscopic work of fracture due to the smaller strain necessary to delaminate the polymer. The variation of the macroscopic work of fracture with the interlayer thickness enables us to push forward this comparison. The result found at 10 °C and 30 mm s^{-1} on the OTES treated sample can be compared with the ones found at 10 °C and 10 mm s^{-1} on the non treated sample (see Section 5.7).

The volume density of the bulk stretching work is lower for the OTES treated sample (5 MJ m^{-3}) than the one found on the non-treated sample (22 MJ m^{-3}) (Figure 6.7). Moreover, the OTES treated sample was tested at a higher imposed velocity of 30 mm s^{-1} and Π_{bulk} tends to increase with the applied velocity. Thus we might conclude that a weaker adhesion induces a decrease of the bulk stretching work. This can be related to the lower mean nominal strain found previously. The interlayer being less stretched, the dissipation associated to this stretch is lower even if the strain rate could be more important.

The near crack work of fracture, $\Gamma_{crack} = 9\,\mathrm{kJ\,m^{-2}}$, was found to be higher for the OTES treated sample than the one one found on the non-treated sample at a lower velocity (5 kJ m^{-2}). As the near crack work of fracture tends to increase with applied velocity, it is difficult to tell if there is a significant difference with the non treated sample. However, it is interesting to see that despite the weaker interface, Γ_{crack} is not highly reduced. This can be explained by the faster front propagation observed on the OTES treated samples (Figure 6.5(a)), which might lead to higher strain rates that can compensate the lower stain level reached by the interlayer in this zone.

Another set of experiments at 10 °C and 30 mm s^{-1} has to be conducted on the

non-treated samples with different interlayer thicknesses to quantify the bulk and close to the front dissipation and to confirm these results. It is however interesting to notice that results similar to the one displayed by the OTES treated sample seems to arise from TCT experiments conducted on samples with a nano meter scale metallic oxyde multilayer in-between the glass and the PVB. This metallic oxide multilayer, is more brittle than the non-treated interface and the rupture occurs inside the metallic layer. This other preliminary results suggest that the observations made during this study can be extended to other systems.

6.5 Conclusion

These preliminary results have shown that interface modification affects the steady state delamination of the interlayer. Especially, for a weaker interface, a faster front velocity and a lower mean nominal strain have been recorded. A steady state delamination regime has been identified at higher velocities and lower temperatures compare to the non treated reference. This lower adhesion level also affects the bulk stretching work and the near crack work of fracture. However more experiments are required to compare these results with the non treated reference samples. For example, the effect of the interlayer thickness on the macroscopic work of fracture has to be checked. APTS treatment has induced an increase in adhesion for which no steady state delamination has been observed. Using lower concentrated APTS solution or silanes mixtures could be a way to mitigate the increase in adhesion. Finally, the effect of interface modification on laminated glass response during impact should be investigated.

Main results

- Silane treatments resulted in the expected changes of adhesion: the OTES treatment reduces it while the APTS treatment increases it.
- A change at the interface affects the range of the stable delamination regime:
  - When the adhesion increase was too large, no steady state delamination was observed for any of the tested velocities and temperatures. A more moderate increase should be considered.
  - The decrease in adhesion shifts the steady state regime towards higher velocities and lower temperatures.
- Compared to the non-treated reference sample, the lower adhesion level displays:
  - A lower constant mean nominal strain ϵ_{TCT}.
  - A higher delamination front velocity.
- As a result the decrease in the macroscopic work of fracture is mainly to be found in the bulk dissipation:

Chapter 7

Finite element modeling description

7.1 Introduction

In the previous chapters we have described the delamination process of the interlayer and the associated dissipation of energy (see chapters 4 and 5). Especially, we have shown that the stretching of the interlayer dissipates a large part of the total dissipated energy in two zones: a fast stretching zone and a near crack area (5.3). We have experimentally been able to study the fast stretching zone but the vicinity of the delamination front is, mainly due to its size, out of reach. Moreover, it is also difficult by the experiment to understand how these different zones are connected together and to the remote loading. Thus a finite element model of the TCT test has been developed to answer these different questions. It can also be a useful tool to confirm and study the effect of several parameters such as applied velocity, adhesion, interlayer behavior and sample geometry on the delamination response.

In this chapter, after a brief introduction of the cohesive zone model used to represent the interfacial rupture between the interlayer and the glass, a complete description of the model is given. This finite element model is then used to reproduce qualitatively the experimental results. The existence of the two dissipation zones will be confirmed and the processes near the crack will be more closely studied. Finally, the effect of viscoelastic relaxation times and adhesion parameters will be observed.

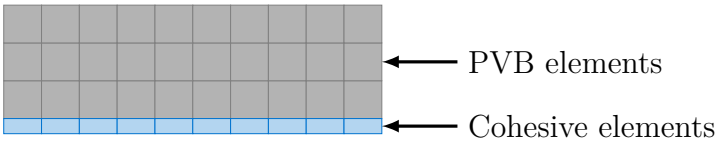

Figure 7.1: Cohesive zone layer of elements representing the interface. The size of the cohesive elements (10^{-3}) is much smaller than the size of the PVB layer above (1).

7.2 Cohesive zone model for the interfacial rupture

Cohesive zone models have been used in several papers dealing with fracture in bulk polymers or at the interface between a soft polymer and a rigid substrate [49] and more specifically between glass and PVB ([50] or [12]). These cohesive zone models are used to describe the work of separation of the interface at the molecular scale.

One model to describe the adhesion at an interface is the Dugdale and Barenblatt cohesive zone model [51]. It is a simple model to describe adhesion. The stress σ is supposed to be constant equal to σ_0 in the cohesive zone while the distance between the two surfaces Δ remains smaller than a critical separation distance Δ_s:

$$\sigma = \sigma_0 \text{ if } \Delta < \Delta_s \tag{7.2.1}$$

When Δ reaches Δ_s the interface fails and $\sigma = 0$:

$$\sigma = 0 \; if \; \Delta \geq \Delta_s \tag{7.2.2}$$

More complex models taking account mode mixity (while the original Dugdale model is only for mode I opening) were developed such as in [52] or [53]. The model implemented in ABAQUS was developed by [54]. It implements irreversible damage of a layer of elements representing the interface (Figure 7.1). Moreover it takes into account mixed mode loading. The following explanation is based on the one presented by *Barthel and coworkers* [55].

In this model, the cohesive elements sustain a certain amount of deformation with an elastic stiffness K as shown in equation 7.2.3 where the stress $\overline{T}$ and displacement $\overline{\Delta}$ can be decomposed in a normal component (T_{22} and Δ_{22}) and a tangential component (T_{11} and Δ_{11}).

$$\overline{T} = K\overline{\Delta} \tag{7.2.3}$$

The combined action of normal (direction 2) and tangential (direction 1) loading in mixed mode loadings can lead to the initiation of rupture below the uniaxial tension level. To take this effect into account, a quadratic rupture initiation criterion is defined. T_{11}^0 and T_{22}^0 are parameters of the cohesive zone that have to be chosen.

The peak stress $\overline{T^0}$ is then the solution of:

$$\left(\frac{T_{22}}{T_{22}^0}\right)^2 + \left(\frac{T_{11}}{T_{11}^0}\right)^2 = 1 \tag{7.2.4}$$

In the case where equation 7.2.4 is verified, the mode mixity angle is defined by:

$$\tan(\psi) = \left(\frac{T_{11}}{T_{22}}\right) \tag{7.2.5}$$

This enables the definition of the work of separation as a function of ψ (equation 7.2.6 with η defined by $\Gamma_s^{II} = \Gamma_s^I(1 + \tan^2(\eta\pi/2))$).

$$\Gamma_s(\psi) = \Gamma_s^I(1 + \tan^2(\eta\psi)) \tag{7.2.6}$$

This elastic behavior holds up to the peak stress $\overline{T^0}$ (corresponding to $\overline{\Delta_0}$). After this peak is reached, damage takes place which decreases the stiffness of the cohesive elements (equation 7.2.7).

$$\overline{T} = K(1-d)\overline{\Delta} \tag{7.2.7}$$

d is the damage parameter which is defined by equation 7.2.8. $\Delta = \sqrt{\Delta_1^2 + \Delta_2^2}$ is the scalar displacement, Δ_0 is the scalar displacement at the maximum stress and Δ_s is the scalar critical displacement.

$$d = \frac{\Delta_s}{\Delta}\frac{\Delta - \Delta_0}{\Delta_s - \Delta_0} \tag{7.2.8}$$

Above the critical displacement Δ_s the crack opens. This critical displacement is defined by equation 7.2.9.

$$\Gamma_s(\psi) = \frac{1}{2}\Delta_s T^0 \tag{7.2.9}$$

In other words, different parameters have to be defined in ABAQUS:

- the stiffnesses K_{11} and K_{22}.
- T_{11}^0 and T_{22}^0 which define the traction separation criterion

- the work of separation Γ_s or the critical opening displacement Δ_s. This value can be defined for different mode mixity angles ψ.

7.3 Model description

In this part we are going to describe the conditions and parameters applied on the TCT geometry. Only one quarter of the geometry is modeled due to symmetries of the problem (Figure 7.2). In order to keep the notation understandable and compatible with the ABAQUS notation, the horizontal direction will be referred to as direction 1 and the vertical direction will be referred to as direction 2.

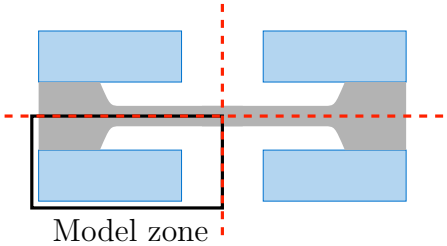

Figure 7.2: Due to symmetries of the problem only a quarter of the TCT sample is modeled.

The model units are taken in order to get proper dimensionless numbers. The distance are all in mm. Hence all moduli and stresses are in MPa. Finally all times are in s.

Geometry

The model geometry is presented in Figure 7.3. First the length of the sample has to be sufficiently long so a steady state delamination regime can be observed. This is obtained for a length larger than the sample thickness. As we choose here $h/2 = 1$ this stable delamination regime will be obtained for a length larger than 2. Moreover, in order to avoid interference between the crack tip field and the left boundary the sample is 15 long. The cohesive zone height has no theoretical meaning as cohesive elements are 1 dimensional elements. However, it has been found that cohesive elements should not deform too much for the calculation to converge without issues. Thus a thickness of 10^{-2} was used. Finally, as the cohesive elements are not designed to model crack initiation a small initial crack was inserted in the model. This crack length is 1. This length will be discussed in the next part.

In order to avoid contact definition problems in-between the cohesive zone and the PVB interlayer, a single part was drawn. This part was then cut into two "materials".

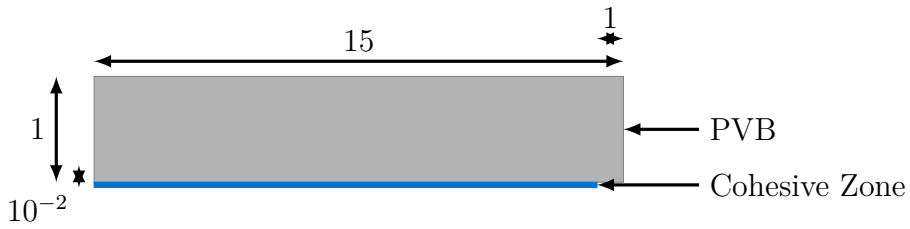

Figure 7.3: Dimensions of the finite elements geometry.

Boundary conditions

The loading and boundary conditions applied on the previous geometry are displayed in Figure 7.4. The displacement on the left part of the interlayer are blocked so that no delamination is observed on this part of the interlayer (except when the delamination fronts reach it). The top part of the geometry corresponds to the middle plane of the TCT test sample. Thus, a plannar symmetry along direction 1 is applied on this border. It corresponds to no displacement in direction 2 and no rotations. On the bottom of the cohesive zone, all displacements and rotations are banned. We assume indeed that the glass is rigid and does not move nor bend during the experiment. This is also the reason why we do not model the glass. Finally, a displacement is applied on the right part of the interlayer. The maximal displacement and the overall loading time are defined. In the viscoelastic models this time will define the applied velocity.

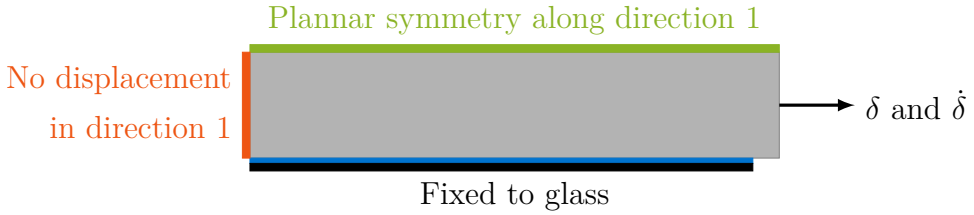

Figure 7.4: Boundary and loading conditions

The initial crack length is in close relationship with this boundary conditions. As we are pulling on the right hand side of the interlayer, if the initial crack length was null, the initial pulling will be pure mode II. In this case, the interlayer elements, close to the cohesive zone, deform too much and convergence fails. This is why

the initial crack length should be long enough so the mode mixity of the initial pulling does not lead to a critical deformation of the these elements. However, as this free interlayer length will be deformed prior to any extension of the cohesive zone elements, the first steps of the calculation consist in some sense in an uniaxial tension test. The initial crack length will define the strain rate applied on this interlayer free part. Hence, because of the viscoelastic response of the interlayer, if this crack length is too large, the strain rate will be too small to reach the critical stress for the cohesive zone to break, which in turn will lead to a severe overshoot in the steady state strain.

In conclusion, the initial crack length has to be short enough to reach the critical stress for the cohesive elements to break at a reasonable strain and long enough so the mode mixity is far from pure mode II. We have found that a length equal to half the interlayer thickness is adequate.

Meshing

The mesh was chosen so the mesh size is small close to the cohesive zone and large far from it. Each edge of the model is seeded with the proper mesh size and the ABAQUS meshing software was used to compose the mesh on the whole part.

The cohesive zone mesh is made from a single layer of quadratic elements COH2D4. These elements have a width of 0.007 and a thickness equal to the cohesive zone thickness 10^{-2}. There is one cohesive element below each PVB element.

The PVB elements are quadratic plane strain elements CPE4RH. The PVB layer is divided in two parts. A first band, just above the cohesive zone, is finely meshed with elements of width 0.007. This layer has a height equal to 1/25 and there is six PVB elements layers in this fine mesh band. Above this first zone the meshing gets progressively looser as it goes away from the interface. A gradient of mesh is imposed vertically from 0.007 to 0.01. On the top edge of the interlayer a seed of size 0.1 is imposed.

The different components of this mesh are presented in Figure 7.5.

The mesh dependence was tested by doing the same calculation with different mesh sizes. In Figure 7.6, the results for the crack tip position and the strain applied far from this crack tip are given for four calculation with different mesh sizes: the standard mesh corresponds to the one described above, the sizes of all elements were multiplied by 2 and 4 respectively for larger mesh sizes and divided by two for a finer mesh size. When the mesh size increases, a significant difference in the result can be seen. The larger the mesh is, the larger the difference is. When the mesh

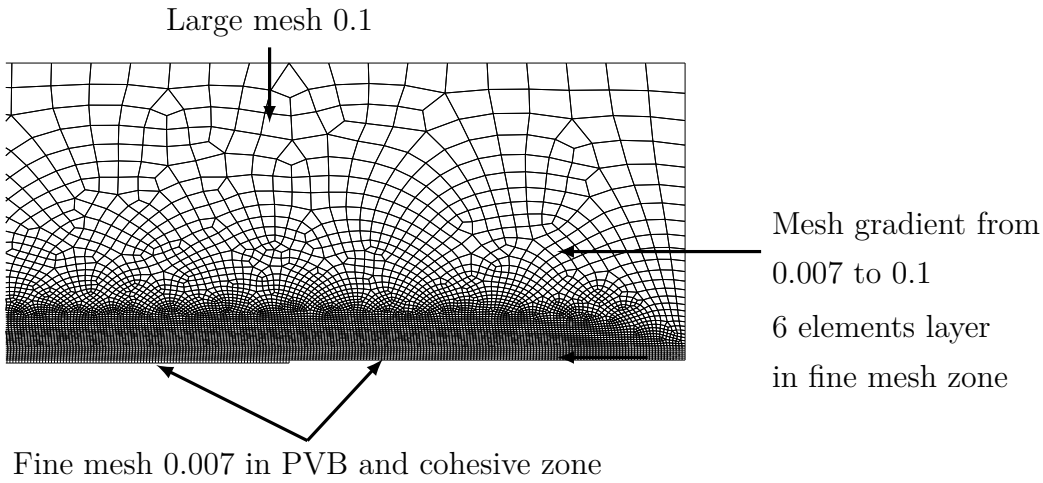

Figure 7.5: Standard mesh used in the TCT test finite elements simulation

size is twice smaller, no difference was seen in the result, but the calculation time increased greatly. Thus, it was found, that the standard mesh size presented just before was the larger which enabled good precision with minimal calculation time.

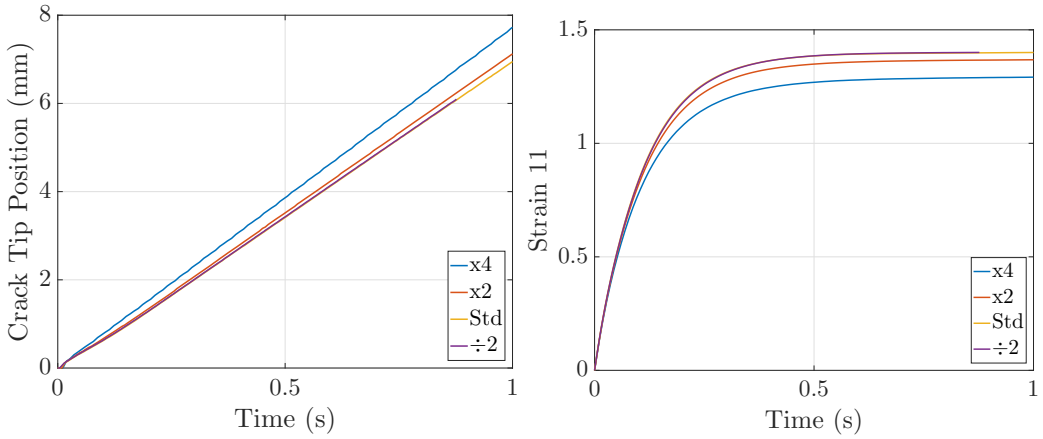

(a) The crack tip position (b) The strain applied far from the crack tip

Figure 7.6: Variation of the results of the FEM calculation depending on mesh size

Convergence problems: artificial dissipation

Even if the interlayer is dissipating energy through viscoelasticity it was found necessary to use an artificial dissipation inside the cohesive zone elements. This artificial viscosity η helps the convergence of the calculation by adding a relaxation time for these elements (see Abaqus Documentation Viscous regularization in Abaqus/Standard Section 32.5.6). As explained by *Gao* [56], this viscosity will regularize the

stress path followed during the damage of a cohesive element. Thus the energy dissipation in the cohesive zone is no longer the static energy release rate Γ_s but an effective adhesion energy Γ_s^* which will have to be evaluated.

Another convergence problem has often arisen when the strain gradient is too large on some elements. This problem especially arises during the first part of the experiment were the initial crack part of the interlayer is loaded up to the point were the crack initiates. To solve this problem two actions have been taken.

First, the tolerance value on the strain has been defined high enough for the convergence to occur. The CETOL parameter has thus been defined at 10^{-2}. This error on strain was defined as suggested in the ABAQUS documentation by considering a admissible stress error and a typical elastic modulus. The modulus of the material is about 10 MPa. This gives an error on stress about 10^{-1}MPa. Stresses during the calculation are of the order of 10 MPa. The error was thus considered to be acceptable. Moreover, the documentation states that in the case of a viscoelastic mode a higher value for the CETOL parameter can be chosen.

Secondly, in order to facilitate the initiation steps, an adhesion gradient was defined at the beginning of the cohesive zone. On a distance of 0.1 mm, the adhesion increases up to the chosen value of adhesion. All the cohesive zone parameters including the initial stiffness K^0 and the maximal stress T^0 are changing along the gradient which is defined with a hyperbolic tangent function: $f(x) = \tan(x/0.1)$. On the rest of the cohesive zone part the adhesion is constant. The gradient distance is chosen so the change in adhesion is steep enough not to affect the results and long enough to ease the initiation convergence issues.

Materials

Now that we have defined the geometry and the mesh plus several other parameters concerning the elements, we will define the material parameters used in this system.

Typical parameters of the cohesive zone are chosen with no mode mixity difference thus these quantities are defined similarly in direction 1 and 2. First a maximal deformation of the cohesive element before rupture was chosen equal to 100%, which means that the maximal displacement of the cohesive element is $\Delta_s = 10^{-2}$ (mm). Then we choose the work of separation equal to $38\,\mathrm{J\,m^{-2}}$. In our sets of units Γ_s is thus 0.038 (MPa mm). This value has been ajusted so the stretching of the interlayer and the delamination velocity are comparable to the experimental values for an applied displacement speed of $10\,\mathrm{mm\,s^{-1}}$ and at 20 °C.

The total energy dissipated by the cohesive element deformation before breakage is however affected by the viscosity introduced in the cohesive zone elements. This viscosity is set to η =0.001 s^{-1}. The effective energy required to stretch and separate the cohesive elements Γ_s^*, will be determined from the calculation results.

The critical stress is set to $T^0 = T_{11}^0 = T_{22}^0$ equal to 7.5 (MPa). Note that the normal direction is direction 2 while the tangent direction is direction 1. In order to get a stiff element without convergence problem it is commonly admitted that damage should begin for a displacement value Δ_0 such that $\Delta_0 = \Delta_s/100 = 10^{-4}$. This leads to $K^0 = K_{11} = K_{22} = 7.5.10^4$ (MPa mm^{-1}). The effective values of T^0 and K^0, respectively T^* and K^*, are also determined for every calculation.

Concerning the interlayer, we have seen how complex its behavior is in Chapter 3. Here we will use a simple model which will keep some of the main features of the interlayer behavior. The time dependence of the material behavior will be described using linear viscoelasticity combined with a non-linear hyperelastic model: a generalized Maxwell model of the viscoelasticity and an Arruda-Boyce model of the hyperelasticity. We will only use one relaxation time for the viscoelastic part. To use such a simple model will, in a first time, help us assess the finite element modeling while qualitatively retrieving some of the experimental observations.

The viscoelastic model is defined through the shear modulus relaxation function:

$$\mu(t) = \mu_0 \left[1 + \sum_{i=1}^{N} \alpha_i (\exp(-t/\tau_i) - 1)\right] \tag{7.3.1}$$

where μ_0 is the instantaneous modulus, τ_i are the relaxation relaxation times and α_i the associated coefficients. Here we use a single relaxation time (Zener Model) τ_1 = 0.01 s and α_1 =0.9. The instantaneous modulus is μ_0 =10 MPa. Using these material parameters, the storage and loss modulus as well as $\tan\delta$ ratio are plotted in Figure 7.7. This shows that there is a ratio of 10 in between the relaxed and instantaneous modulus and that the dissipation is maximal around 0.01 s^{-1}. The relaxation of the shear modulus, is also plotted in Figure 7.8. This model qualitatively represents the behavior observed in DMA experiments (Figure 3.6).

The hyperelastic Arruda Boyce model is defined by:

$$\sigma(t) = 2\mu(t)\left(\lambda(t) - \frac{1}{\lambda(t)^2}\right)\sum_{i=1}^{5} \frac{iC_i I_1(t)^{i-1}}{\lambda_m^{2(i-1)}} \tag{7.3.2}$$

In this equation, the shear modulus is replaced by the viscoelastic model defined previously in equation 7.3.1 and the maximal chain extensibility will be set at 100%

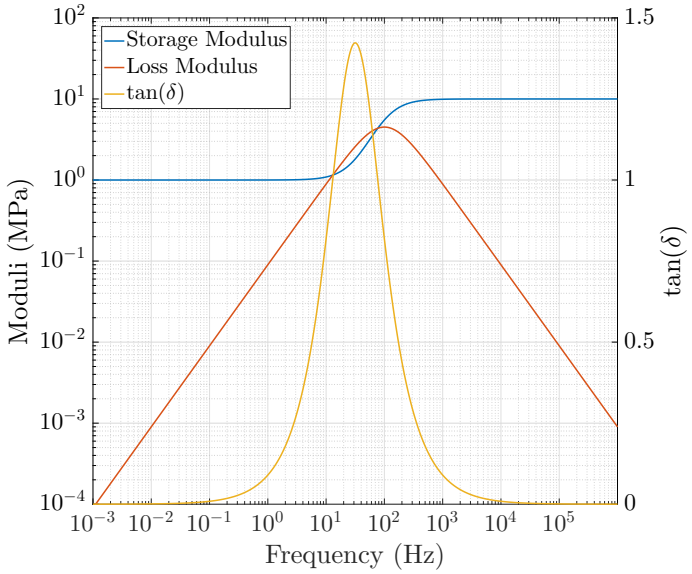

Figure 7.7: The storage and loss moduli as functions of frequency. The glass transition is observed around $100\,\mathrm{s}^{-1}$ and corresponds to the maximal dissipation.

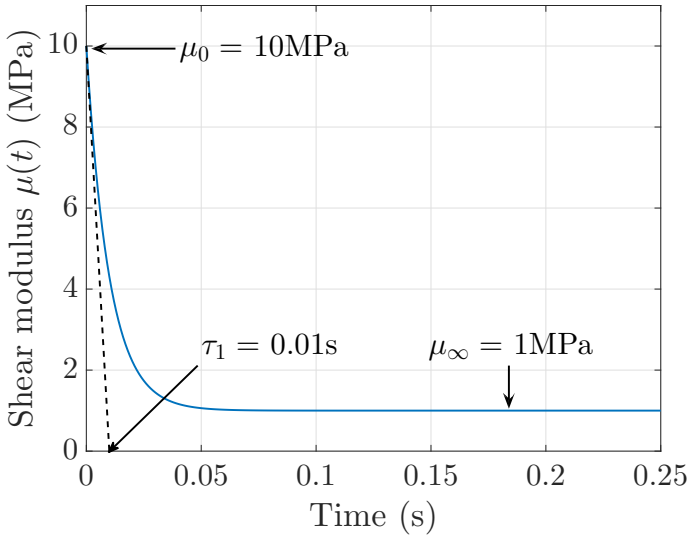

Figure 7.8: Relaxation function of the shear modulus for τ_1 =0.01 s and α_1 =0.9.

of strain (λ_m=2).

These different parameters were chosen to dissipate an large amount of energy at certain strain rates between $10\,s^{-1}$ and $100\,s^{-1}$. These strain rates will be activated close to the crack tip and in the bulk deformation zone. In Figure 7.9 one can see that at these strain rates, the dissipation is quite large and the material displays a strong strain hardening at strain larger than 100%. However, as soon as the strain rates are slower or higher, this model of the material tends towards a pure hyperelastic model in which there is little to no dissipation. Especially, at high strain rates, we have seen that this does not reproduce the real PVB behavior (Figure 3.12). The next step in the modeling work will have to take into account the viscoplastic part of the material description.

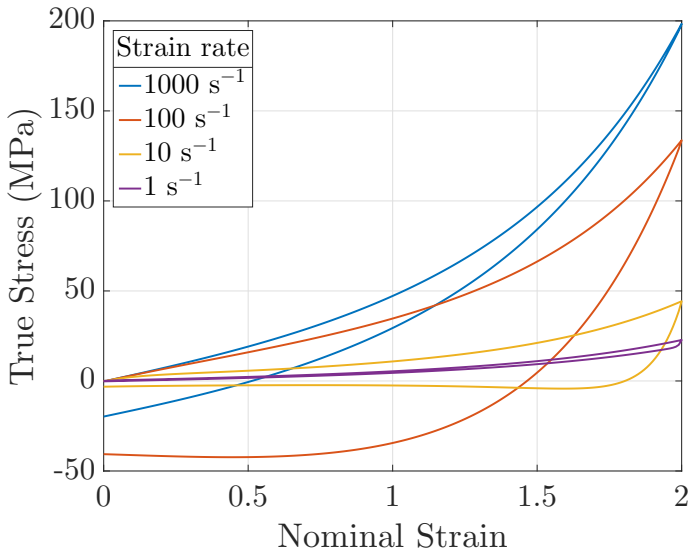

Figure 7.9: Calculated traction curve for our model polymer with $\mu = 10\,MPa$, $\lambda_m = 2$ and one relaxation time $\tau_1 = 0.01\,s$ and α_1 =0.9.The calculation was made for four different strain rates from $1\,s^{-1}$ to $1000\,s^{-1}$. These results can be compared with experimental curves in Figure 3.12.

7.4 Recovering a steady state delamination

The model extensively described in the previous part will now be used to recover qualitatively some experimental results. Especially a steady state delamination will be obtained and the main characteristics of the delamination and interlayer stretching will be extracted in this regime.

7.4.1 Decohesion processes

First, to check that the cohesive element response gives consistent results, we compare it to the expected theoretical response describe in 7.2. In Figure 7.10, different curves are plotted as a function of the distance to the delamination front. The stresses (measured at the top of the cohesive zone) in the two directions far from the front are equal to the hydrostatic value. When they reach the value T^0 one can notice that the damage coefficient d (in the cohesive elements) starts to increase. However, the stresses keep increasing after reaching T^0 up to T^* due to the viscosity introduced in the cohesive elements. When the damage coefficient reaches 0.99 the crack opening (position of the top nodes of the cohesive zone) is equal to the critical value $\Delta_s = 0.01\,\text{mm}$ and the cohesive elements break. Instead of going straight to zero, the stress relaxes due to the viscoelastic nature of the interlayer.

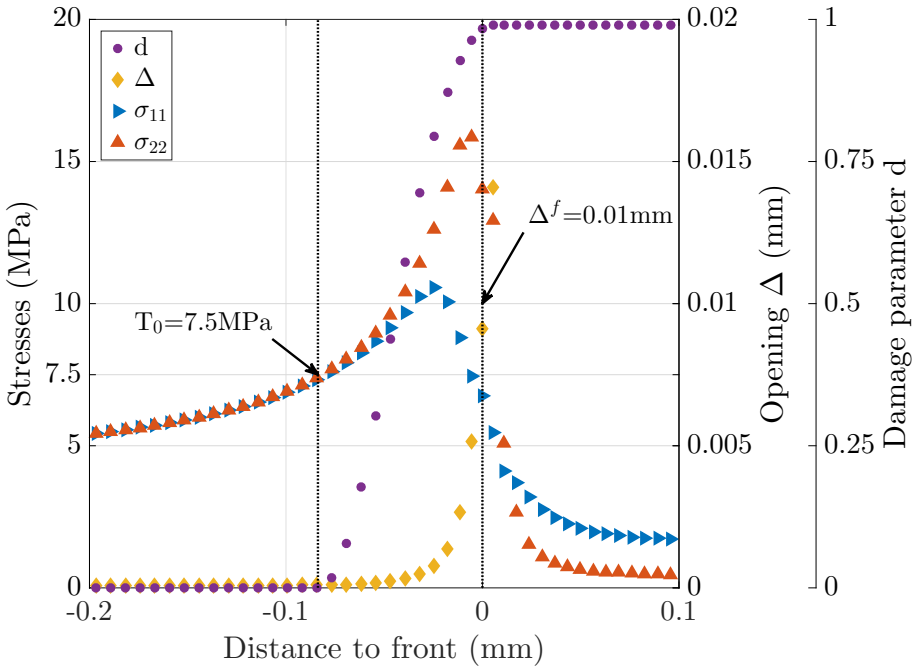

Figure 7.10: The stresses in the two directions and the position of the top nodes of the cohesive zone are plotted as functions of the distance to the delamination front. The damage parameter measured in the cohesive elements is also plotted.

In Figure 7.11, the three components of the stress tensor, measured at the top nodes of the cohesive zone, are plotted as functions of the crack opening. The shear stress is close to zero. This representation also shows that the cohesive element response is linear far from the delamination front where displacement of the cohesive elements node is below $\Delta^0 = 10^{-4}$mm. The stiffness of the elements in this region can be measured and is equal to $K^* = 7.5.10^4\text{MPa}\,\text{mm}^{-1}$ as prescribed. For an

opening greater than Δ^0, the cohesive elements are damaged as shown just before.

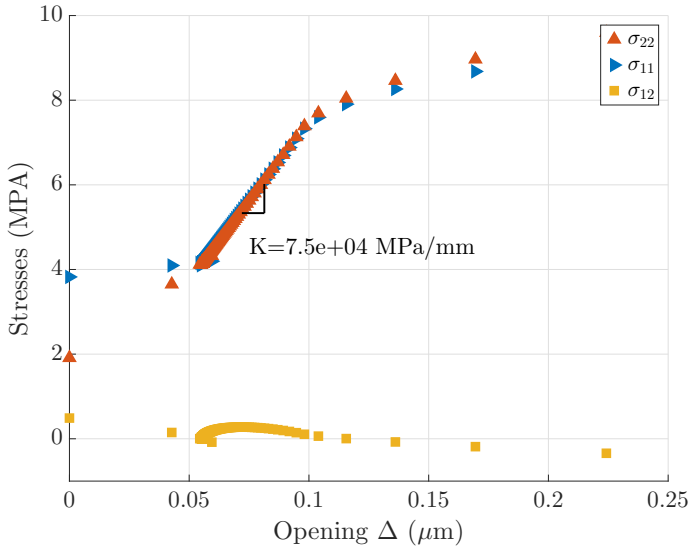

Figure 7.11: The different stress components are plotted as a function of the crack opening. The stresses σ_{11} and σ_{22} evolve linearly with the crack opening up to the opening Δ_0 =0.1 µm. A stiffness $K^* = 7.5e4\text{MPa}\,\text{mm}^{-1}$ is measured.

7.4.2 Hydrostatic stress induced by the boundary conditions and the incompressibility

One can notice in the previous picture that the stresses in directions 1 and 2 do not decrease to zero in the region which is not delaminated. This is due to the facts that the interlayer is described as an incompressible material and that boundary conditions imply that no displacement are permitted far from the delamination front. Thus hydrostatic stresses appear in the material. In Figure 7.12, the stress in direction 1 (pulling direction) in the material is plotted along the median plane as a function of the distance to the delamination front. One can see that the stress value is constant before the front and equal to 4.3. This value is the same for the stress in direction 2 (orthogonal to the pulling) before the front. The strains associated with this hydrostatic stress are of the order of $\epsilon_{11} = 10^{-4}$, $\epsilon_{22} = 10^{-5}$ and $\epsilon_{12} = 10^{-4}$. Thus energy associated to this hydrostatic component can be evaluated and is about $G_h \approx 10^{-4}\text{kJ}\,\text{m}^{-2}$. Even if the hydrostatic stress is not negligible, the energetic contribution of this stress can be neglected compared to the other energies.

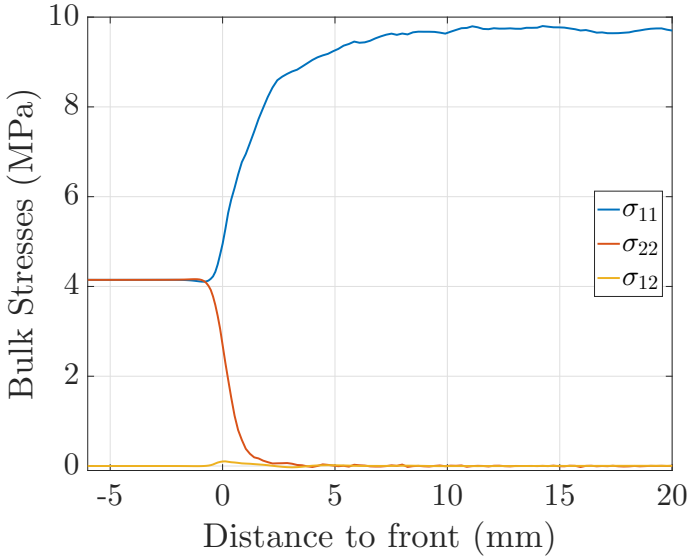

Figure 7.12: The different stress components along the median axis. Before the delamination front, a significant hydrostatic stress is observed.

7.4.3 Energy flows balance

In order to ensure that the calculation gives consistent results, one can look at the different energies recorded during the delamination. These energies are plotted as functions of the delamination front position (Figure 7.13). These plots show that a steady state delamination is reached as the energies are linear functions of front position. The energy release rates associated to these energies are calculated by taking the slope of these curves divided by the interlayer width equal to 1 mm. The different energy release rates are displayed in Table 7.1.

The sum of all energies is equal to the macroscopic work of fracture. This reflects the fact that the system reached a steady state in a consistent manner.

Secondly, the dissipated energy in the cohesive zone, corresponding to the viscous and damage dissipation in the cohesive elements, is dominated by viscous dissipation. This dissipation is much larger than the value of Γ_s that was defined in the model. We can thus define an effective adhesion energy Γ_s^* equal to $0.2\,\mathrm{kJ\,m^{-2}}$. Because the interlayer does not dissipates as much energy as the real material ($\mu_\infty = \mu_0/10$), the viscous dissipation and the elastically stored energy in the interlayer are of the same order of magnitude. The bulk stretching work Γ_{bulk} is equal to the sum of this elastic stored energy and viscoelastic dissipated energy in the interlayer: $\Gamma_{bulk} = \Gamma_{bulk}^{visco} + \Gamma_{bulk}^{el}$. The viscoelastic dissipation is sufficient to enhance the adhesion. Indeed, the energy required to break the cohesive elements is equal to $0.2\,\mathrm{kJ\,m^{-2}}$ and a macroscopic work of fracture equal to $5.9\,\mathrm{kJ\,m^{-2}}$ is required for the delamination

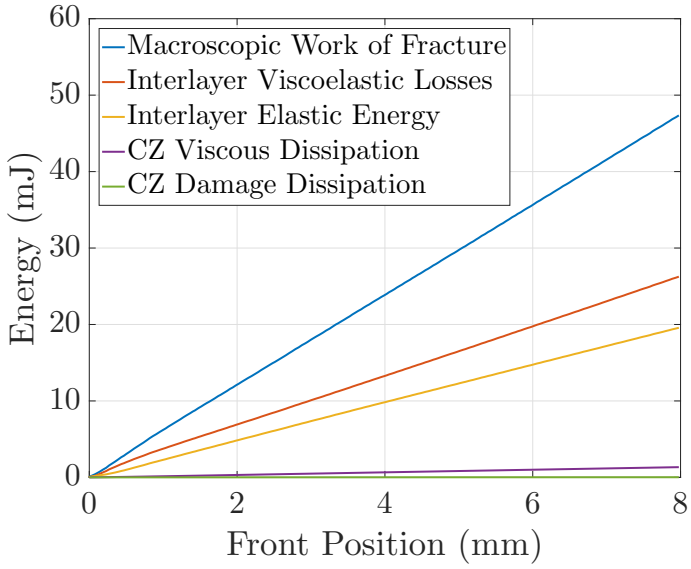

Figure 7.13: Different energies recorded during the delamination. A steady state delamination is reached as the energies increase linearly with the delamination front position. The macroscopic work of fracture G_m (blue) is the total work provided to the system. Both viscoelastic losses (red) and elastically stored (yellow) energies in the interlayer are plotted. The viscous (purple) and damage (green) dissipation in the cohesive zone (CZ) are also plotted.

Energies	$\mathrm{kJ\,m^{-2}}$
Macroscopic work of fracture	5.9
Elastic energy stored in the interlayer	2.5
Viscoelastic dissipation in the interlayer	3.2
Viscous dissipation in the cohesive elements	0.2
Damage dissipation in the cohesive elements	0.0026

Table 7.1: The different energies measured during the steady state delamination.

front to propagate. This macroscopic work of fracture corresponds to the energy brought to a quarter of the TCT sample and is similar to the values found in the experiments for half a sample ($\approx 10\,\mathrm{kJ\,m^{-2}}$ – see Figure 5.1).

7.4.4 Far field measurements

Several results will now be qualitatively compared to the experiment. The point is to ensure that the results found here are representative of what is occurring during the experiment. Even if the material behavior is only partially described and even if the effective adhesion energy is much larger than the energy provided by hydrogen bond adhesion between PVB and glass, the far from the delamination front behavior can be recovered.

First, the delamination front propagates at a constant velocity about $7\,\mathrm{mm\,s^{-1}}$. This value is of the same order of magnitude as the one found during the experiment (see Figure 4.5).

After a first transient state, the delamination occurs in a steady state manner. The strain on the right end side of the PVB is equivalent to the strain measured in between the delamination fronts during the TCT Test. This strain in direction 1 (pulling direction) is plotted, in Figure 7.14(b), as a function of time. One can see that the strain measured in direction 1 will reach a plateau value of 1.4 after approximately a time of 0.4 s. This value, corresponds to a delamination over a length of approximately 2 mm equal to the interlayer thickness (Figure 7.14(a)). The strain value is close to the one found in the TCT experiment (see Figure 4.6). The initial transient behavior spans over a length equal to the interlayer thickness as in the experiment (see Figure 5.2).

The relation between the applied displacment δ, the strain ϵ and the delamination front position a is here given by $\epsilon = \delta/a$ as we pull on half a TCT sample.

The stress in direction 1 on the right end side of the interlayer is plotted as a function of time in Figure 7.15. This stress reaches a steady state value of 10 MPa which lead to a force of 1000 N for an interlayer thickness of 2 mm and 50 mm width. As the interlayer thickness is only a parameter of the calculation, the force for an interlayer thickness of 0.76 mm can also be deduced from this stress value and would be about 380 N. These values are of the same order of magnitude as the one found in the experiment (see Figure 4.4).

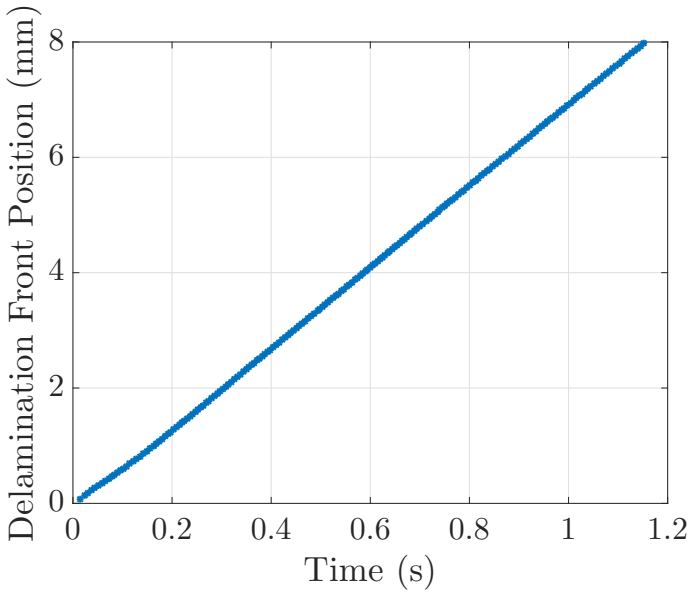

(a) Delamination front position.

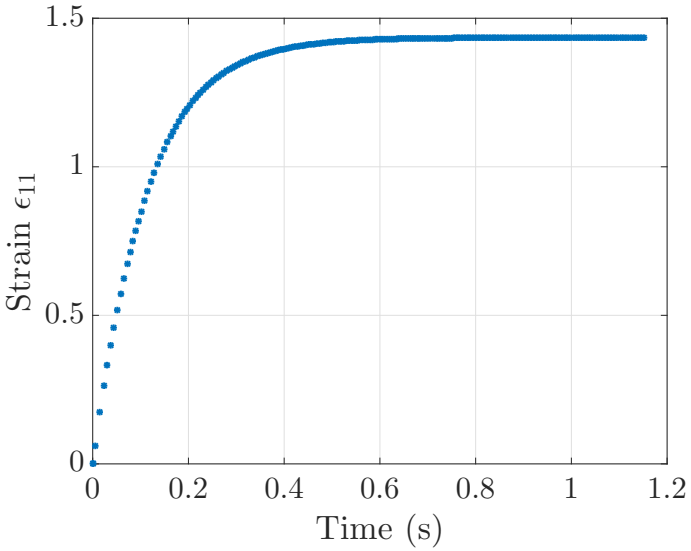

(b) Strain in direction 1 on the right end side of the interlayer.

Figure 7.14: (a) The delamination front position is plotted as a function of time. Delamination velocity is about $7\,\mathrm{mm\,s^{-1}}$. Compariason with experiment. (b) The strain in direction 1 on the right end side of the interlayer is plotted as a function of time. The steady state strain of 1.4 is reached after a delamination over a length equal to the interlayer thickness 2 mm.

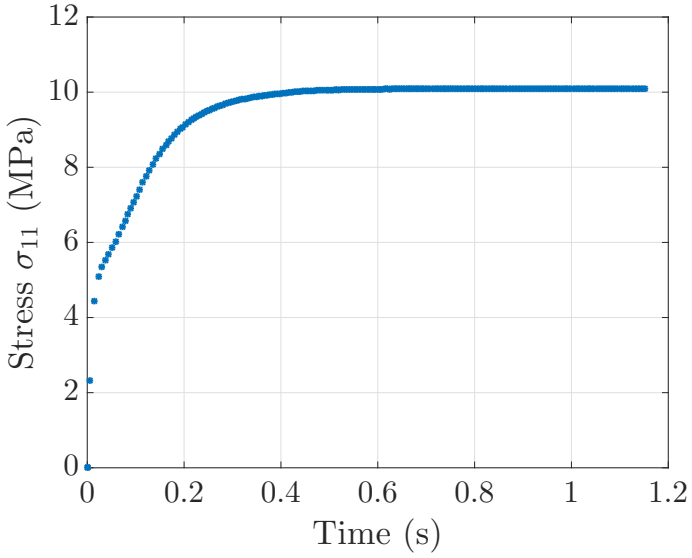

Figure 7.15: The steady state value reached by the stress on the right end of the polymer as a function of the crack tip position and the corresponding time.

7.5 Two zones of dissipation

A steady state has been observed as in the TCT experiments. In this steady state regime, the different zones of stretching of the interlayer will now be studied. The point of this model is indeed to get a better understanding of the process in the delamination front vicinity.

Two zones of deformation can clearly be identified in Figure 7.16 where the strain field in direction 1 (the applied displacement direction) is displayed.

The fast stretching zone appears with a strong gradient in the strain in direction 1. In particular on the median plane of symmetry this strain gradient corresponds to the one measured in the DIC experiment on the plane where ink dots were sprayed.

In the vicinity of the delamination front, a contraction zone in direction 1 (corresponding to a stretching zone in direction 2) is confined in a smaller area. This second stretching zone corresponds to the expected dissipation zone near the crack tip.

7.5.1 The fast stretching zone

First, in the fast stretching zone, we will compare our results to the ones obtained previously from the DIC experiments (see 4.4.2 and 5.3)

On the median axis of symmetry, the strain in direction 1 is plotted in Figure 7.17 as a function of the distance to the point right above the delamination front.

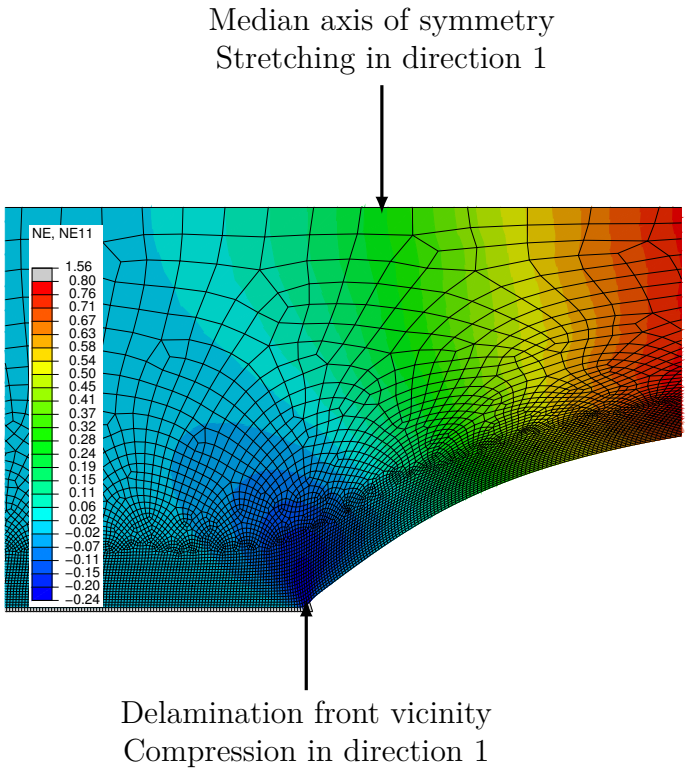

Figure 7.16: The finite element mesh is displayed with the strain in direction 1 field.

In this figure, the strain in direction 1 presents a spatial distribution which is highly similar to the one observed in the TCT test. Indeed, the strain increases rapidly over a length equal to the interlayer thickness h and then stabilizes at a steady state value. Moreover, the strain increases up to 70% of the steady state value on this distance h which is also similar to the result found in the DIC measurements (see Figure 4.12). In the experiment, the mean constant strain value $\epsilon^0_{\mathrm{TCT}}$ is reached much faster than in the finite element model. Indeed, the finite element calculation is made in real plain strain whereas in the experiment, the width narrowing spans over a much longer distance (close to the initial width 50 mm). This intermediate length scale is hidden in these two dimensional calculations.

Similarly to what has been found during the experiments, the strain rate on this length can be evaluated by $\dot{\epsilon}_{11} = \frac{V_{front}}{h} * \epsilon_{11} = 7 * 2 * 1.2 = 4.2\,\mathrm{s}^{-1}$. In this zone, the strain rate can reach a higher value as displayed in Figure 7.18. The maximal strain rate is about $5\,\mathrm{s}^{-1}$. The strain rates obtained here correspond to the maximum of dissipation of the viscoelastic interlayer with a relaxation time of 0.01 s.

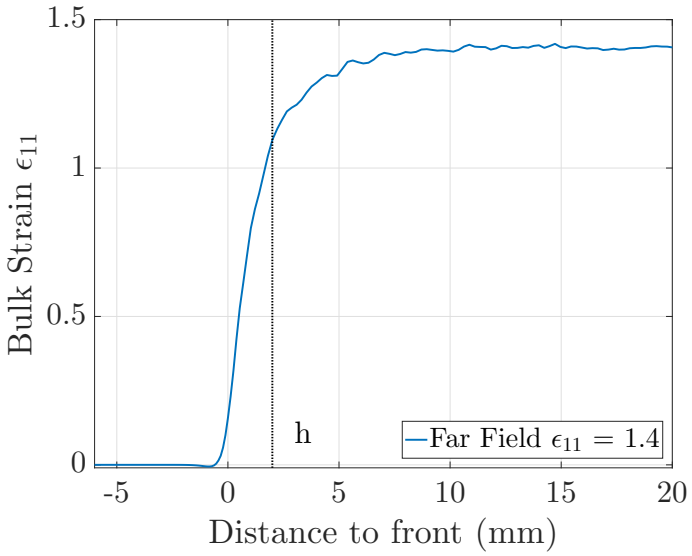

Figure 7.17: Steady state regime strain in direction 1 along the median axis of symmetry as a function of the distance to the crack tip. Deformation occurs mainly on a distance equal to the interlayer thickness.

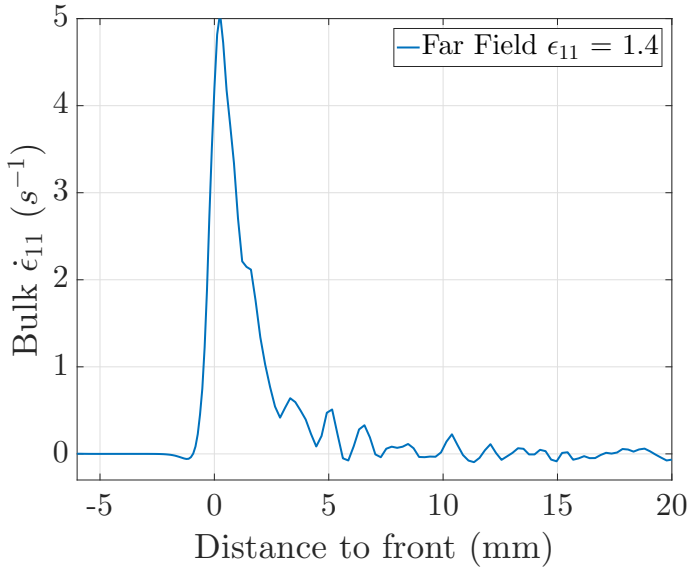

Figure 7.18: The local steady state strain rate in direction 1 along the median axis of symmetry as a function of the distance to the crack tip. The mean strain rate is about $1.5\,\mathrm{s}^{-1}$ but the maximal strain rate is about $5\,\mathrm{s}^{-1}$.

7.5.2 Near crack process zone

In the previous parts, the results were similar to the one found in the TCT experiments. The vicinity of the delamination front will be now described.

The results presented here, have to be taken with caution. Indeed close to the delamination front, the strain rate and the strain levels encountered by the interlayer in the real experiment are not properly described by the simple interlayer behavior used in this finite element model. Moreover, the mesh size might not be fine enough to describe the crack tip properly. In the vicinity of the crack tip, the strain distribution is completely different from the one just described in the bulk material. Indeed, the strain variations are concentrated in a small area around the crack tip. In this zone, the polymer is in tension in direction 2 and compression in direction 1. In this zone, the maximal strain in direction 2 is about 0.3. The large values of strain above 0.25 are concentrated on a surface of about 7.10^{-4}mm^2. However, the strain values higher than 10% are covering a much larger area which is approximately a disk of 0.4 mm of diameter. A rough estimation of the strain rate along the interface gives a value close to $30\,\text{s}^{-1}$ which is already much higher than in the fast stretching zone. However, the zone of strain concentration might not be meshed finely enough to get a proper description of the strain and the strain rates involved could be higher.

In the representations of the deformation field in direction 1 and 2 (Figure 7.19), the process zone close to the delamination front can spatially be from the fast stretching zone. It confirms the separation hypothesis made in 5.3 about the two different sources of dissipation. It is interesting to emphasize however, that this spatial separation of the two zones of dissipation does not imply the absence of interactions. These interactions were not studied here and could be at the core of future work on this topic.

7.6 Near crack work of fracture

One of the remaining questions at this point is how much energy is dissipated near the delamination front. To answer this question, the energy flow entering this area can be determined similarly to the Poynting vector used for electromagnetic fields. We use the approach of *Atkinson and Eshelby* [57] based on an energy-momentum tensor to determine the energy flow Π_S entering a given contour $\mathcal{C}$ around an area $\mathcal{A}$ surrounding the crack tip. Note that simultaneously *Rice* [58] used a similar approach to develop the concept of J-Integral for the case of elastic fracture. For

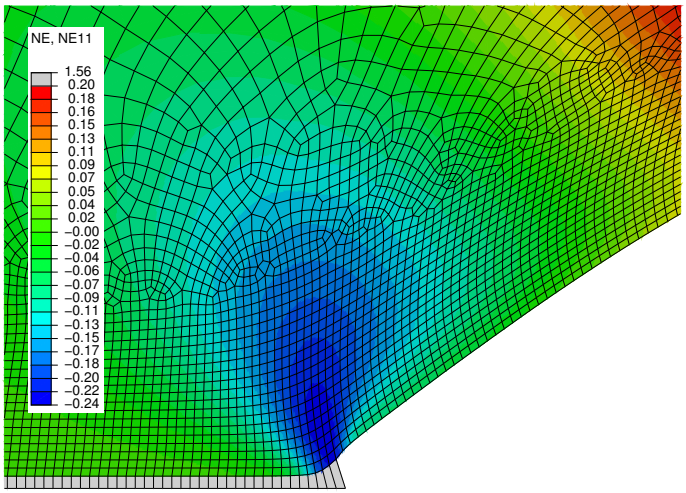

(a) Strain in direction 1

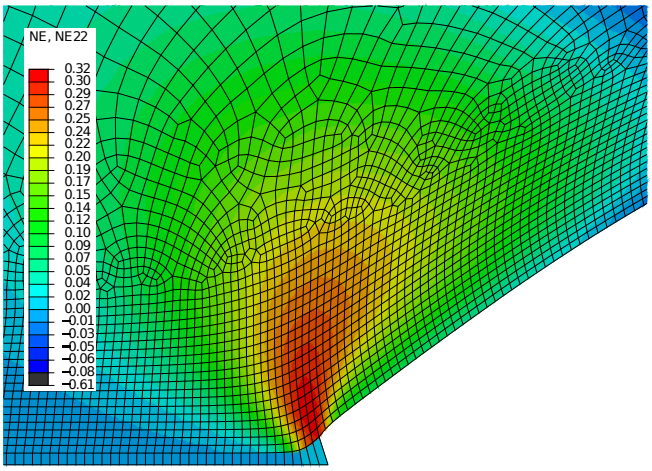

(b) Strain in direction 2

Figure 7.19: Strain field near the delamination front in the steady state regime.

our viscoelastic material, the specific properties of the J-Integral and especially its path independence do not hold. The energy flow is here defined by:

$$\Pi_S = \int_{\mathcal{C}} \left(W\delta_{jk} - \sigma_{ij}\frac{\mathrm{d}u_i}{\mathrm{d}x_k} \right) m_j \mathrm{d}s \tag{7.6.1}$$

As a energy flow, Π_S is a vector. In this equation W is the stored energy density defined as $W = \int_0^{\epsilon_{ij}} \sigma_{ij}\mathrm{d}\epsilon_{ij}$. σ_{ij} and ϵ_{ij} are the stress and strain field components. m_j is the vector normal to the contour $\mathcal{C}$ and $\mathrm{d}s$ the curvilinear abscissa along the same contour. Further information about the different terms and explanation about this integral can be found in *Bower*'s book [59].

This integral definition is valid in a region where the strains are small (though it can be extended to large strain). This is really appropriate in this case as there is a region in between the fast stretching zone and the delamination front process zone in which strain is low. In this region, a circular contour $\mathcal{C}$ will be drawn and used to calculate the energy flow. This contour is defined as a circle centered on the delamination front with a radius defined by the maximal strain encountered on his path. An example of contour is given in Figure 7.20. Through the interface part of the contour, the energy flow is equal to Γ_s^*. On the open crack part of the contour, the energy flow is zero. Thus the calculation is only made on the circular part of the contour. The radius of the circle is defined so it passes through a region where the maximal strain is lower than 5%.

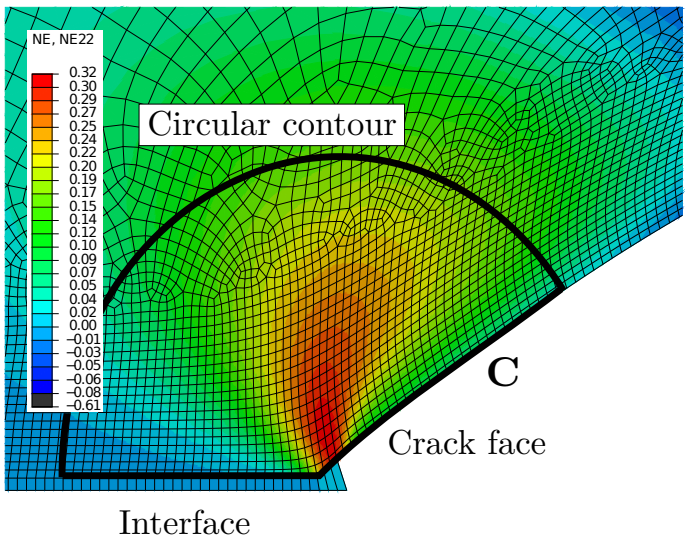

Figure 7.20: Contour used for the energy flow calculation, passing through a "small" strain area around the process zone in the vicinity of the delamination front.

The delamination propagates in direction $k = 1$. So to calculate the energy flow

we have to determine two terms. The first one corresponds to the work of external forces done on the contour $\mathcal{C}$ which in our case will be approximated by:

$$W\delta_{j1}m_j = \frac{1}{2}(\sigma_{11}\epsilon_{11} + \sigma_{22}\epsilon_{22} + 2\sigma_{12}\epsilon_{12})m_1 \tag{7.6.2}$$

The second term arises from the rate of change of mechanical energy inside the area $\mathcal{A}$. As σ and ϵ are symmetric tensors this term can be written as:

$$\sigma_{ij}\frac{\mathrm{d}u_i}{\mathrm{d}x_1}m_j = (\sigma_{11}\epsilon_{11} + \sigma_{12}\epsilon_{12})m_1 + (\sigma_{22}\epsilon_{12} + \sigma_{12}\epsilon_{11})m_2 \tag{7.6.3}$$

In the previously defined loading conditions and material description, the calculation of Π_S in direction $k = 1$ gives $\Pi_S^1 \approx 1\,\mathrm{kJ\,m^{-2}}$.

Π_S includes the viscoelastic losses in the interlayer and the viscous and damage dissipation in the cohesive elements:

$$\Pi_S = \Gamma_{crack} + \Gamma_s^* \tag{7.6.4}$$

Thus, as $\Gamma_s^* = 0.17\,\mathrm{kJ\,m^{-2}}$, $\Gamma_{crack} \approx 0.8\,\mathrm{kJ\,m^{-2}}$ are dissipated in the interlayer process zone close to the delamination front. This also means that the energy dissipated by viscoelastic losses in the interlayer stretching can be divided in $2.4\,\mathrm{kJ\,m^{-2}}$ dissipated in the fast stretching zone and the rest corresponds to the near crack work of fracture. The ratio between these two kinds of dissipation is comparable to the one found in the TCT experiment between Γ_{crack} and $\Pi_{bulk}h$ close to 0.5.

To sum up the result of this paragraph, the different energies are displayed in Figure 7.21 as parts of the macroscopic work of fracture. A schematic view of the delaminating interlayer gives the location of the related dissipation zone.

7.7 Impact of interlayer relaxation time and work of separation

The results found in the previous paragraph depend on both the interlayer behavior and work of separation. In order to compare their effects on the delamination process, we will focus on the propagation velocity of the delamination front, the maximal strain in direction 1 far from the delamination front, the total work, the energy dissipated in the vicinity of the delamination front and the length of the fast stretching. For each case, Γ_s^* will be evaluated.

The adhesion and the interlayer behavior were also studied during the experi-

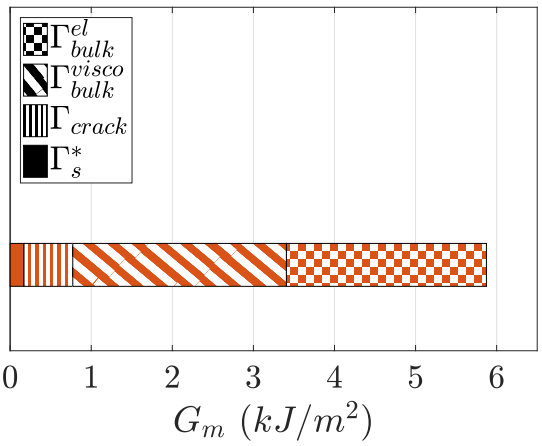

(a) Partition of G_m

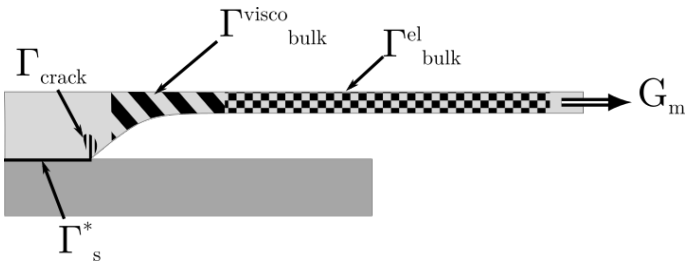

(b) Location of the dissipation zones

Figure 7.21: The macroscopic work of fracture is dissipated in different zones before some energy can be delivered to the crack tip for the crack to advance.

mental part. Experimentally it is challenging to change one without affecting the other (see 6). In the finite element model it is easier to change the interlayer behavior without acting on the adhesion and vice-versa. It has to be noted that a shift in the relaxation time of the interlayer viscoelastic response is equivalent to a change in the applied velocity.

7.7.1 Work of separation

Three different levels of the effective work of separation were tested numerically. The three parameters of the cohesive zone were changed simultaneously as it was found that keeping a similar shape of the traction separation law was leading to less convergence problem. Thus the standard adhesion refers to the previously used cohesive zone set of parameters $\Gamma_s = 0.038\,\mathrm{MPa\,mm}$, $T^0 = 10\,\mathrm{MPa}$ and $K^0 = 7.5\,\mathrm{MPa}$. The lower and higher levels of adhesion were obtained by respectively dividing and multiplying the three parameters by a factor 2.

The effective work of separation and effective maximal cohesive stress found for these three different adhesion levels are given in Table 7.2. The cohesive element viscosity is unchanged and still equal to $\eta = 0.001\,\mathrm{s}^{-1}$. As one can see, these are effectively three different levels of adhesion. Due to the viscosity, the effective work of separation Γ_s^* is 4 to 6 times larger than the original Γ_s and T^* is about 1.5 times T.

Adhesion level	Γ_s^* ($\mathrm{kJ\,m^{-2}}$)	T^* (MPa)	K^* (MPa mm)
Low $\div 2$	0.069	7.5	3.75
Standard	0.17	16	7.5
High $\times 2$	0.46	27	15

Table 7.2: Effective cohesive zone parameters for the three different level of adhesion.

In all these simulations, the loading velocity $\dot{\delta}$ is equal to $10\,\mathrm{mm\,s^{-1}}$. The change in adhesion leads to different front propagation velocities. In Figure 7.22, the delamination front position is plotted as a function of time for the three levels of adhesion. In the three cases, a steady state delamination regime is obtained. The higher the adhesion, the lower the delamination velocity: $10\,\mathrm{mm\,s^{-1}}$ for the lowest adhesion, $7\,\mathrm{mm\,s^{-1}}$ for the standard adhesion, $5.5\,\mathrm{mm\,s^{-1}}$ for the highest adhesion. Note that the front is advancing in the direction opposite to the pulling direction. Thus the stretching of the interlayer is given by: $\epsilon_{\mathrm{TCT}} = \delta/a$.

Figure 7.23 displays the strain ϵ_{11} calculated along the middle plane of the inter-

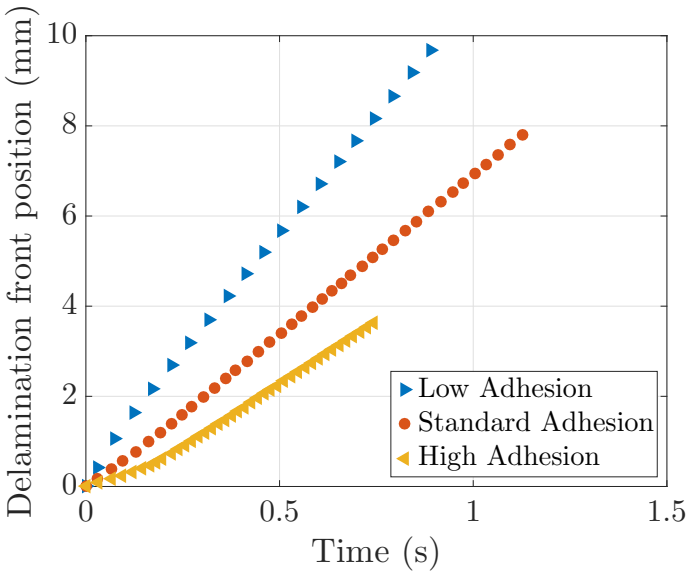

Figure 7.22: Delamination front position as a function of time for the three levels of adhesion tested. The delamination reaches a steady state in which the delamination front velocity is decreasing as the adhesion increases.

layer. This strain increases when adhesion increases as the front velocity decreases and the loading velocity is constant. This is similar to what has been found in the experiment: the OTES treatment lead to a weaker interface, the delamination front velocity was higher and the strain was found to be lower than for the non treated sample (see Figure 6.5).

For the three levels of adhesion, the fast stretching zone spans over the same length equal to the interlayer thickness h. This confirms that this effect is solely due to the sample geometry namely the interlayer thickness. However, the increasing strain and the decreasing delamination velocity have antagonist effects on the dissipated energy. In the case of the high adhesion, the delamination velocity is about $5.5\,\mathrm{mm\,s^{-1}}$ and the strain reached over the fast stretching zone is about 1.5. This leads to a strain rate close to $4.1\,\mathrm{s^{-1}}$. For the lowest adhesion, the delamination velocity close to $10\,\mathrm{mm\,s^{-1}}$ is higher but the strain reached over the fast stretching zone about 0.7 is lower. This results in a lower strain rate of $3.5\,\mathrm{s^{-1}}$. Thus a lower level of adhesion leads to both a lower strain and a lower strain rate which should lead to a lower amount of dissipated energy from the stretch mechanisms.

This last conclusion is confirmed by the macroscopic work of fracture G_m found in the steady state regime. In the case of the standard adhesion, G_m is equal to $5.9\,\mathrm{kJ\,m^{-2}}$. For the lowest adhesion level, $G_m = 2.5\,\mathrm{kJ\,m^{-2}}$ whereas for the highest level of adhesion G_m =$13\,\mathrm{kJ\,m^{-2}}$. This work is partially stored elastically (Γ^{el}_{bulk}) or

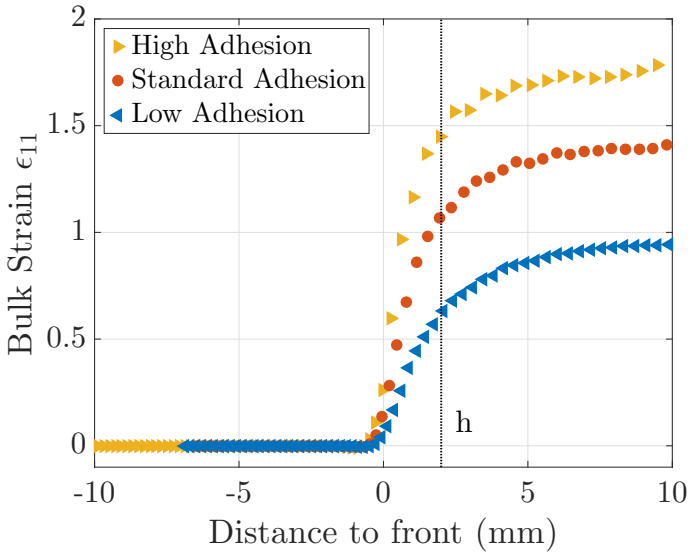

Figure 7.23: Bulk strain measured along the middle plane of symmetry in direction 1 for the three different levels of adhesion. As the adhesion increases the interlayer is stretched at a higher level of strain.

dissipated (Γ^{visco}_{bulk}) in the bulk interlayer: $\Gamma_{bulk} = \Gamma^{el}_{bulk} + \Gamma^{visco}_{bulk}$.

It is also dissipated near the crack tip Γ_{crack}. In Figure 7.24, the partition of this total work is displayed for the three levels of adhesion. The values of each energy release rate are also given in Table 7.3. As adhesion increases both values of the energy dissipated near the crack tip and in the bulk of the interlayer increases. Moreover, the ratio between the near crack work of fracture and the bulk stretching work is almost constant between the low and standard adhesion (close to 0.2) whereas it is tripled for the high level of adhesion (about 0.6).

Adhesion level	G_m	Γ_{bulk}		Γ_{crack}	Γ^*_s
		Γ^{el}_{bulk}	Γ^{visco}_{bulk}	$= J - \Gamma^*_s$	
Low	2.5	1.3	0.9	0.2	0.067
Standard	5.9	2.5	2.6	0.6	0.17
High	13	2.4	6.4	3.7	0.46

Table 7.3: Different energies dissipated during the steady state delamination for three different levels of adhesion. All values are in $\mathrm{kJ\,m^{-2}}$.

This shows that a change in adhesion affects the whole delamination process from the interlayer maximal stretch to the strain rates involved. This impacts the different zones of dissipation of energy in a non proportional manner. It emphasizes the interactions between the near front process zone and the fast stretching zone. These interactions, in which Γ^*_s and T^* play different roles, are yet not well understood.

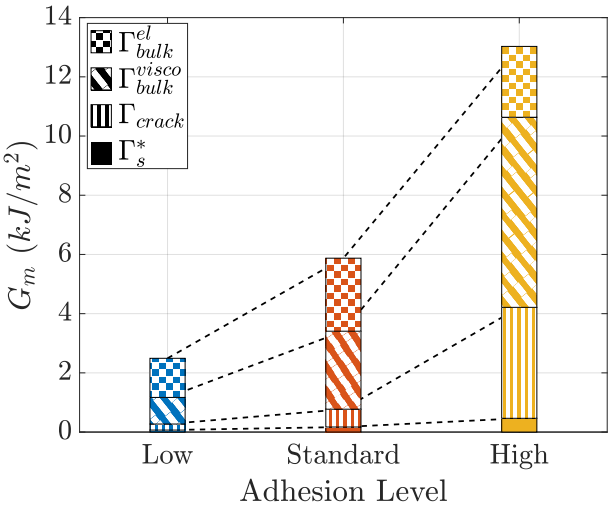

Figure 7.24: Partition of the macroscopic work of fracture (G_m) required for the steady state delamination. Energy is either stored elastically in the interlayer (Γ^{el}_{bulk}), dissipated by viscoelasticity in the bulk of the interlayer (Γ^{visco}_{bulk}) or dissipated near the crack tip (Γ_{crack}) before it can be used to separate the interface (Γ^*_s).

7.7.2 Viscoelastic relaxation time

Three different relaxation times τ_1 were tested 0.001 s, 0.01 s and 0.1 s. The rest of the material parameters are kept constant. The pulling velocity is also kept equal to 10 mm s^{-1}. The relaxation times have to be compared to this velocity. In Figure 7.25, a calculated cyclic uniaxial tension response up to 200% is plotted for the three different times at a strain rate of 100 s^{-1}. This numerical experiment qualitatively emulates the experiments conducted in Figure 3.12. One can see that a higher relaxation time is equivalent to a faster pulling speed and a lower relaxation time is equivalent to a slower pulling speed. The parameters of the cohesive zone for these three cases are given in Table 7.4. The effective adhesion energy Γ^*_s is similar for the lowest and intermediate times but it is slightly higher for the highest time, due to the higher crack velocity. The critical stress T^0_c has an effective value which is similar for the three times. The adhesion will thus be considered as not changed between the two lower times but significantly different for the highest time. This difference will be explained in the following paragraphs.

For τ_1 =0.001 s and τ_1 =0.01 s the delamination reaches a steady state regime (Figure 7.26). The front velocity is equal to 7 mm s^{-1} in both cases. The strains are comparable in the two cases and equal to 1.3 for τ_1 =0.001 s and to 1.4 for τ_1 =0.01 s (Figure 7.27). For these two cases, most of the stretch of the interlayer occurs over a length equal to its thickness.

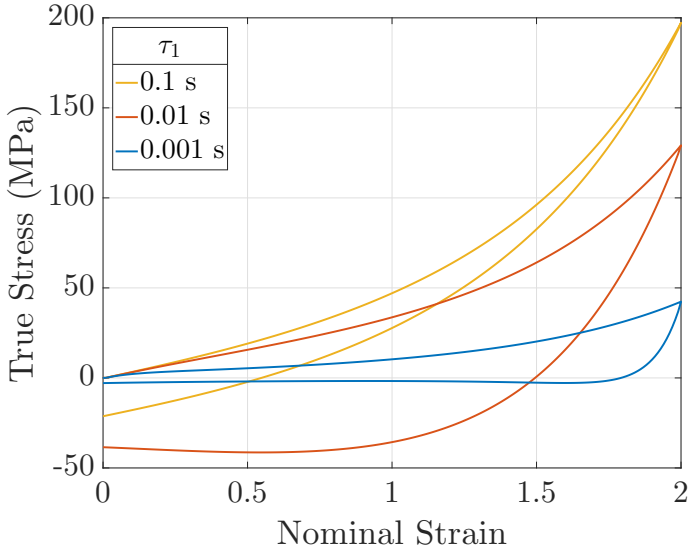

Figure 7.25: Uniaxial tension response at $100\,\mathrm{s}^{-1}$ for the three different relaxation times.

τ_1	Γ_s^* (kJ m^{-2})	T^* (MPa)	K^* (MPa mm)
0.001	0.22	18	7.5
0.01	0.17	16	7.5
0.1	0.39	20	7.5

Table 7.4: Effective cohesive zone parameters for the three different times.

On the contrary, for τ_1 =0.1 s no steady state is observed. The delamination front propagation is fast and only slows down because of the viscosity of the cohesive zone elements. In this case, the strain does not reach a steady state value and is lower than 0.9 when the calculation ends.

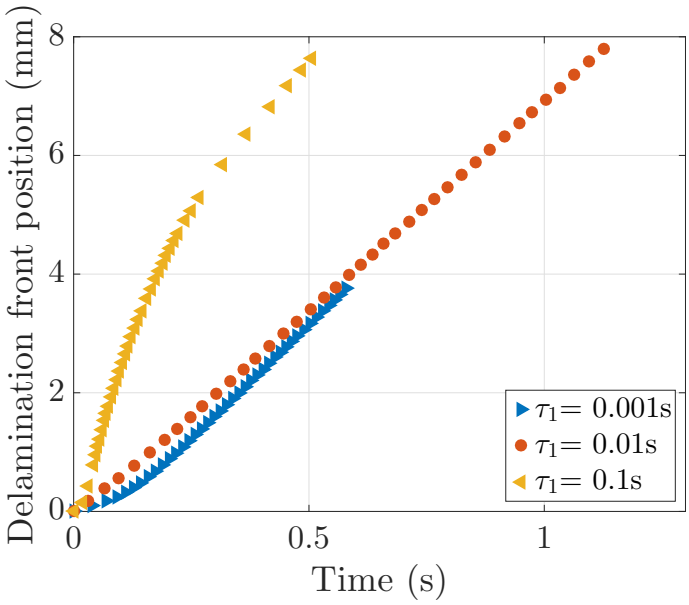

Figure 7.26: The delamination front position as a function of time for three relaxation times τ_1. For τ_1 =0.1 s no steady state was reached.

The partition of the macroscopic work of fracture is displayed in Figure 7.28 and the different energies are summarized in Table 7.5 for the three different relaxation times.

In the case of τ_1 =0.1 s, fast delamination and lower strain lead to a near crack work of fracture close to 0. Indeed, the Π_S calculation gives that all the energy flowing to an area close to the delamination front is used to separate the cohesive elements. None of this energy is dissipated in the vicinity of the crack tip. This could be due to very large strain rates, so the interlayer responds as an elastic material.

For the two lower times, Γ_s is equal to 0.2 kJ m^{-2}. Using a shorter relaxation time to describe the viscoelasticity of the material is equivalent to a slower pulling speed. This induces a smaller macroscopic work of fracture. Close to the crack tip, a larger amount of energy is dissipated for $\tau_1 = 0.001\,\mathrm{s}^{-1}$. This seems to be due to a huge maximal strain close to 1.4 reached in this zone. On the contrary, in the bulk interlayer, lower strain rates and a slightly lower strain, lead to smaller elastic and dissipated energy compared to the intermediate time. The ratio of viscoelastic dissipation over the elastic energy is constant close to 0.5 for $\tau_1 = 0.001$ s and $\tau_1 = 0.01$ s. Finally, between τ_1 =0.001 s and τ_1 =0.01 s, the decrease in the near

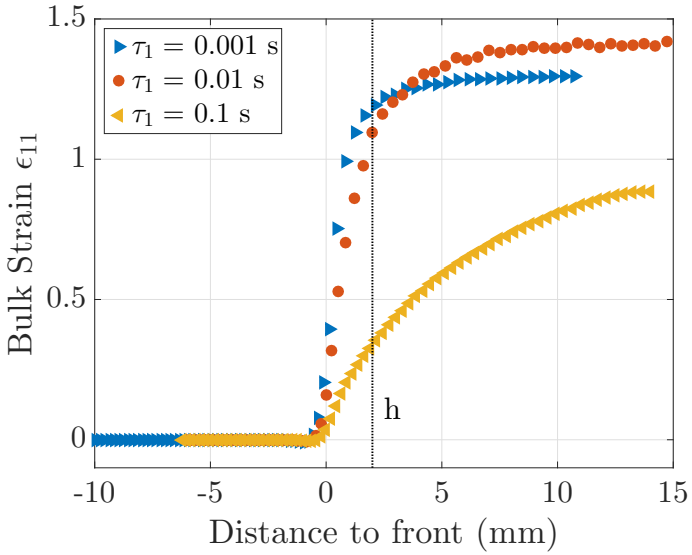

Figure 7.27: The strain along the mid plane is plotted as a function to the distance to the point at the vertical of the delamination front for the three relaxation times τ_1.

crack work of fracture is compensated by the increase in the bulkd stretching work leading to similar macroscopic work of fracture in the two cases. It appears that the increase of the relaxation times induces a transfer of the dissipation from the near crack process zone into the bulk stretching zone.

τ_1 (s)	G_m	Γ^{el}_{bulk}	Γ^{visco}_{bulk}	Γ_{crack}	Γ^*_s
0.001	4.8	0.95	1.3	2.2	0.22
0.01	5.9	2.5	2.6	0.6	0.17
0.1	3.9	0.73	2.8	0	0.39

Table 7.5: Different energies dissipated during the steady state delamination for three different viscoelastic relaxation times τ_1. All values are in kJ m^{-2}.

7.8 Coupling between the near crack and bulk stretch responses.

The previous section shows that the energy dissipation in the near crack process zone and in the bulk of the interlayer are connected and that this relationship depends on the material relaxation time and on adhesion. Here we will describe these interactions using the material behavior.

In [41], *Barthel and Fretigny* estimate the near crack work of fracture within a linear viscoelastic theory. In this approach, the creep function of the material is

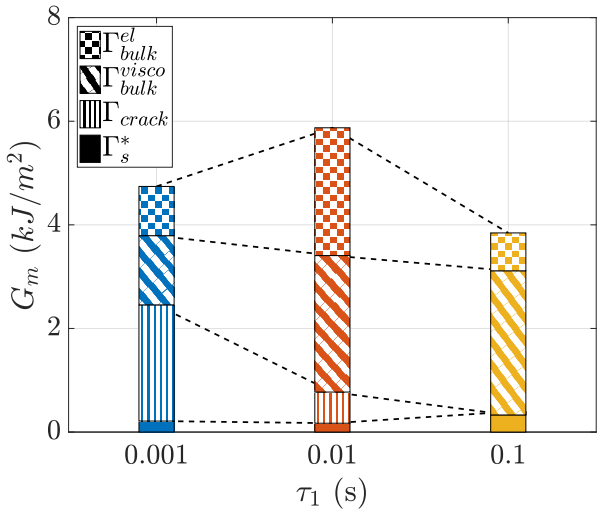

Figure 7.28: Partition of the total work required for the steady state delamination for three different viscoelastic relaxation times τ_1.

used to connect the far fireld to the near crack field.

This model defines, the length of the cohesive zone d_{CZ} by:

$$d_{CZ}(t_{CZ}) = V_{front} t_{CZ} \tag{7.8.1}$$

where V_{front} is the delamination front velocity and t_{CZ} is the time it takes to the delamination front to cross the length d_{CZ}.

ϕ is an effective creep function of the material for an advancing crack. Denoting k as the ratio between the long term and instantaneous moduli: $k = \frac{E_\infty}{E_0}$ and for a Zener model (single relaxation time τ_1, which corresponds to a creep time $\tau_c = \tau_1/k$) ϕ can be expressed as:

$$\phi(t) = \frac{2}{E_\infty}\left[1 + 2\frac{1-k}{(t/\tau_c)^2}(1 - t/\tau_c - \exp(-t/\tau_c))\right] \tag{7.8.2}$$

The work of separation is a constant defined as:

$$\Gamma^*_s = \frac{\pi}{8}(T^*)^2\phi(0)d_{CZ}(0) = \frac{\pi}{8}(T^*)^2\phi(t_{CZ})d_{CZ}(t_{CZ}) \tag{7.8.3}$$

Finally, the ratio between the near crack work of fracture and the work of separation is given by:

$$\frac{\Gamma_{crack}}{\Gamma^*_s} = \frac{\phi_\infty}{\phi(t_{CZ})}. \tag{7.8.4}$$

This last equation shows that the near crack work of fracture is related to the

work of separation through the ratio between the behavior of the relaxed material (far from the crack) and the material behavior close to the crack. Thus the underlying hypothesis is that far from the crack the material is in a relaxed state.

This approach will now be used to describe the previous results.

For the different adhesion levels used in 7.7.1, we can retrieve the near crack work of fracture using the creep function of equation 7.8.2. This method gives results (Table 7.6) of the same order of magnitude than the one found with the energy flow Π_S (see Table 7.3). This method also provides an estimation of d_{CZ} and t_{CZ}. The distance d_{CZ} decreases from 5 to 3 cohesive elements affected by the propagation of the crack. This is similar to what is found in the finite element calculations. The frequency at which the material is loaded at the crack tip increases with adhesion. These frequencies are on the glassy side of the glass transition (Figure 7.7). This is coherent with the fact that Γ_{crack} is 10 times higher than Γ_s*. According to this model, the dissipation at the crack tip is saturated for the three levels of adhesion.

Adhesion level	d_{CZ} (mm)	t_{CZ} (ms)	$\omega_{CZ} = 2\pi/t_{CZ}$ (Hz)	Γ_{crack} (kJ m^{-2})	Γ_s^* (kJ m^{-2})
Low	0.041	4.1	1530	0.60	0.067
Standard	0.023	3.3	1900	1.54	0.17
High	0.023	4.1	1530	4.1	0.46

Table 7.6: Evaluation of the near crack work of fracture Γ_{crack} and of the frequency ω_{CZ} in the vicinity of the delamination front using the creep function for three different levels of adhesion.

The same approach can be taken for the three relaxation times. The near crack work of fracture and t_{CZ} are evaluated in Table 7.7. The Γ_{crack} values found here are not comparable to the ones found previously with Π_S (Table 7.5). This can be explained by the fact that the ratio k used to estimate the creep function ϕ is no longer appropriate as for $\tau_1 = 0.001$ s and 0.1 s the assumption that the material is fully relaxed in the far field no longer applies.

τ_1	d_{CZ} (mm)	t_{CZ} (ms)	$\omega_{CZ} = 2\pi/t_{CZ}$ (Hz)	Γ_{crack} (kJ m^{-2})	Γ_s^* (kJ m^{-2})
0.001	0.016	2.3	2700	1.33	0.22
0.01	0.023	3.3	1900	1.54	0.17
0.1	0.040	1.0	6300	3.89	0.39

Table 7.7: Evaluation of the near crack work of fracture Γ_{crack} and of the frequency ω_{CZ} in the vicinity of the delamination front using the creep function for three different relaxation times.

Thus an extension of this model which could take into account the real behavior of the interlayer far from the delamination front, would be able to describe properly this situation.

7.9 Conclusion

The delamination of the interlayer has been modeled and some of the most important features of the experiment were recovered: especially the fast stretching zone length and the distribution of strain are found to be similar to the ones found in the experiment. The finite element model also confirmed the separation of the dissipated energy in two zones of dissipation: a fast stretching zone and a process zone in the delamination front vicinity. By calculating the energy flow Π_S, the energy dissipated in this latter zone has been evaluated.

One can also note that the fast stretching zone can be modeled as in paragraph 5.6 by a uniaxial stretching of the interlayer at the appropriate strain rate. Here, using the polymer model defined in 7.3, at $4.2\,\mathrm{s}^{-1}$, the interlayer stretched up to 120% dissipates $4.2\,\mathrm{kJ\,m}^{-2}$. This value is close to the one deduced from the Π_S calculation ($2.4\,\mathrm{kJ\,m}^{-2}$).

At the crack tip the delamination of the interlayer occurs mainly in mode I despite the remote loading which is similar to a 0° peel test. The blunting of the interlayer close to the delamination front leads to its stretching in direction 2. In this near crack process zone the strain rates are of the range from 100 s to 1000 s for which dissipation is at a maximum.

Finally, the dependence of the delamination response with the interlayer viscoelastic relaxation time and work of separation has evidenced strong coupling between the different zones of dissipation. It was difficult to show clear tendencies for a change of the viscoelastic time. This is due to the fact that the interlayer viscoelastic description with only one relaxation time leads to a narrow glass transition. Changing adhesion had the expected impact on delamination: an increase in adhesion leads to an increase in interlayer stretching and to an increase of the dissipated energy. However, a too stiff increase in adhesion should lead to stretch the interlayer at strain too large for the calculation to converge. Similarly a very weak adhesion will not be possible in terms of calculation convergence as the front will propagate “instantaneously“ and a problem similar to the high relaxation time will be encountered.

Future work will have to focus on the description of the interlayer behavior to take into account a larger amount of dissipated energy at large strains and high strain rates. Most of the calculation time is spent on reaching the steady state delamination. Thus a clear improvement will be to develop an Eulerian formulation instead of the actual Lagrangian formulation, as described by *Dean and Hutchinson* in [60].

Main results

- The steady state delamination is recovered:
  - The steady state delamination velocity, strain and stresses are comparable to the experiment.
  - The fast stretching zone length is equal to the interlayer thickness.
- The separation of the macroscopic work of fracture in two dissipation zones has been confirmed.
- The near crack work of fracture is evaluated thanks to the energy flow Π_S and the different components of the macroscopic work of fracture have been deduced from there.
- The effects of different levels of adhesion and of different relaxation times on the delamination response have been studied.
- Using the material creep law, the coupling between the near crack instantaneous response and the relaxed response of the interlayer, far from the delamination front, has been displayed.

Chapter 8

Conclusions and perspectives

The main purpose of this study was to make the link between impact performance of laminated glass, interlayer rheology and loss of adhesion. For thin enough glasses, the impact results in glass breakage, followed by interlayer delamination and stretching to large deformation. To identify the source of the dissipation mechanisms, the interlayer mechanical behavior has been thoroughly studied in relation to microstructure. To connect this behavior to the delamination processes and to characterize different dissipation zones, a model experiment has been setup and analyzed.

The small strain behavior of the PVB interlayer displays a classical time/temperature dependence (section 3.3.1). At large strain the PVB response is highly non linear with a complex behavior depending on the applied strain rates and temperatures (section 3.3.2). At high strain rates or low temperatures, the interlayer presents a yield stress at moderate strains and a strong strain hardening for higher strains. In this regime more than 80% of the energy provided to stretch the interlayer is dissipated. For lower strain rates and higher temperatures these features disappear and a more classical non linear viscoelastic behavior is observed. About 40% of the energy is dissipated in these conditions.

Using photoelastic measurements (section 3.4) and complementary DSC (section 3.5.1) and SAXS experiments (section 3.5.2), we were able to establish a model for the interlayer polymer network (3.5.3). In this model, two interpenetrated networks correspond to two modes of energy dissipation. A first network presents a viscoplastic like behavior. It is composed of chains crosslinked by hydrogen bond nodules. The second network is not involved in the H bond nodules, but it is connected to the rest of the polymer network through entanglements and isolated hydrogen bonds. Due to the presence of the second viscoelastic network, the plastic response of the first network can be activated only at high strain rates (section 3.6).

The interlayer behavior being more clearly understood, the question was: What type of dynamic loading does the polymer undergo during delamination? In the TCT test, a steady state delamination regime was first identified in a certain range of temperatures and applied velocities (section 4.2). In this regime, the delamination occurs in a symmetric way, the delamination fronts are straight and propagate at constant velocity. The delamination velocity has been found to be proportional to the applied velocity. The steady state regime is bounded by two other regimes (section 4.3). Most of the time, at higher velocities or lower temperatures, the delamination stops due to the rupture of the more brittle interlayer, which is more sensitive to experimental defects. At lower velocities or higher temperatures an interesting unstable regime was observed; the delamination fronts start to undulate and often stops leading to interlayer rupture.

In the steady state delamination regime, two different dissipation mechanisms were identified (section 5.3). In the immediate vicinity of the delamination fronts the rupture of the interface combined with a local deformation of the interlayer leads to a non negligible near crack work of fracture. Ahead of the fronts, the interlayer gets deformed through its whole thickness in a fast stretching zone at high levels of strain. Digital image correlation and photoelastic measurements have shown that this stretching of the bulk material occurs over a length equal to the interlayer thickness. This result is of prime interest as it enables to estimate the strain rate applied on the interlayer knowing the delamination velocity. In this zone, interlayer stretching can be described mainly as a uniaxial tension (section 5.6). Thus we have demonstrated that a uniaxial tension test, at the appropriate strain rate, can be used to estimate the volume density of the bulk stretching work.

Finally, the effects of applied velocity, temperature and interfacial toughness on these dissipation mechanisms have been studied. The near crack work of fracture and volume density of the bulk stretching work increase when the velocity increases or when the temperature decreases (section 5.7). Three levels of adhesion have also been obtained with silanized glass surfaces (section 6.2). At higher level of adhesion, no delamination was observed and the interlayer was immediately ruptured. For lower adhesion, the delamination occurs faster and induces a lower strain level than for the reference level of adhesion (section 6.3.2).

A finite element model has been implemented to describe the delamination mechanisms in a qualitative manner. The interlayer is described as a viscoelastic-hyperelastic material and the interface is modeled with cohesive elements. Some characteristics of the TCT test have been retrieved (section 7.4): the steady state

delamination, the large interlayer stretch and the length of the fast stretching zone in which most of the interlayer deformation occurs as in the experiment. This model confirms the tentative breakdown of dissipation into two process zones and two mechanisms. A strong coupling between these two processes appear, but the major parameters and how they affect the overall response have not been demonstrated yet. A preliminary estimation of the energy dissipated in the crack vicinity has also been performed (section 7.6). It has been used to compare different simulations with different loading conditions and different adhesion levels (section 7.7).

♢

From this picture of the delamination and of the associated dissipative processes in the TCT test, we can derive a better understanding of the coupling between the remote loading and the crack tip mechanisms occurring during delamination of this viscous interlayer. In our case, the polymer ligament is stretched at high levels of deformation and because of the dissipation mechanisms in the interlayer rheology, a large amount of energy is dissipated. Similarly to what has been observed in the peeling of adhesives [61], a large deformation zone is observed ahead of the crack tip. In the case of thin films of adhesive, the formation of fibrils and their subsequent rupture leads to the dissipation of energy. However, a second dissipation zone also exists in the immediate vicinity of the crack, similar to what is observed in thicker films.

♢

Still, many points of our study could be investigated in future studies.

First, concerning the structure of the PVB interlayer, the size of the H bond nodules and the distance between these nodules has not been clearly identified by the SAXS experiments. In particular, the distance in between the nodules could be better measured by diffraction of visible or near UV light as it seems to be of the order of hundreds of nm. Moreover, such experiments could confirm the nature of these nodules.

PVB is not the only interlayer that is being used in the laminated glass industry. Thus the results that have been established with PVB in the TCT test have to be compared to other interlayers such as PU which is used in more high end applications (plane or bulletproof windshields) or EVA which is used in less demanding applications in terms of impact performance (interior walls, decorative panels,...).

The interest of such studies could be to have materials with a simpler mechanical behavior to further challenge our conclusions.

Concerning the TCT test, a lot of work still needs to be done on the dependence of the bulk and crack related dissipation processes on different parameters such as applied velocity and temperature (see 5.7). The trends that have been established are not as precise as they should be to estimate the energy dissipated during the impact for different impacting object velocities and at different temperatures. We believe that this could be an interesting tool from the industrial point of view.

An interesting preliminary work has also been done together with *Raphaëlle Kulis* on the dependence of the TCT response on adhesion. There is plenty to be done on this road. A finer tuning of adhesion could confirm the trends observed during this study, though it could be difficult to get a higher level of adhesion in which the polymer does not rupture. We believe that a solution could be to increase the temperature or to slow down the applied displacement to get a steady state delamination.

Concerning the finite element modeling a future step could be to transfer most of the viscous dissipation of the cohesive elements either in the damage dissipation of these elements or in the interlayer material itself. The transfer of this dissipation will ensure more control over the interfacial rupture energy and stresses. The transfer in the damage dissipation of the cohesive elements is not difficult to implement but it will considerably increase the calculation time. To transfer the viscous dissipation in the interlayer behavior will be more difficult and requires a better description of the PVB rheology. A better description of the interlayer behavior is also required to get a better picture of the processes in the neighborhood of the delamination front. This description will have to include the plastic like behavior of the PVB at high strain rates and low temperatures. A *Bergström-Boyce* model [25] is a good example of the kind of model that could be implemented to model the interlayer behavior as it takes into account both large strain and plastic behavior. This model can also be extended to viscous behavior. The drawback of such a model is the large number of parameters that have to be tuned.

Up to now, the TCT test model has reproduced the whole initiation and propagation process (even if, there was no attempt to reproduce anything real about the initiation part of the problem). In this Lagrangian formulation, the whole calculation, is thus used to reach the steady state delamination regime in which a single step of the calculation is analyzed. A more efficient way to make this calculation could be to use a Eulerian formulation as described by *Dean and Hutchinson* in [60]

or *Landis et al.* in [62].

The whole part of the impact concerning the first microseconds after the impact has not been tackled at all. It should be of high interest to look during these first instants of the impact at the effect of the interlayer on the propagation of cracks in the glass. This work could be related to the results of *Vandenberghe et al.* [63] in which the number of cracks is connected to the impacting object velocity and to the interfacial energy required to propagate a crack in glass. It is possible that a higher apparent interfacial energy will be measured in the case of laminated glass. As pointed out by *Chen et al.* [10] the crack propagation velocity should also be lower in the case of laminated glass. The effect of the interlayer thickness or of other relevant parameters such as the glass thickness, the temperature or the humidity rate and the nature of the interlayer could also be investigated.

Résumé

Les verres feuilletés sont des structures constituées d'un intercalaire polymère pris entre deux plaques de verres (Figure 8.1). Cet intercalaire améliore les performances du verre feuilleté en empêchant la perforation par l'objet impactant et en retenant les éclats de verre. Ces propriétés en font un matériau particulièrement adapté pour de multiples applications dans le bâtiment (façades, vitrines, sols et plafonds) ou dans les véhicules (pare-brises d'avions et de voitures ou vitres blindées).

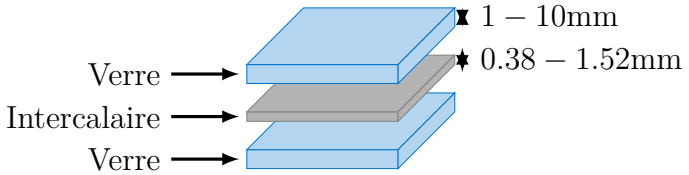

FIGURE 8.1 : Structure d'un verre feuilleté

Ces verres sont soumis à des tests normés qui consistent généralement en un ou plusieurs impacts sur une large plaque de verre feuilleté, dans des conditions reproduisant une situation particulière. Ainsi, dans le cadre de la norme pour l'habitat EN 356 une une bille de 4 kg est lâchée d'une hauteur de 3 m à trois reprises, sur une plaque d'environ 1 m^2. Le test est considéré comme réussi si la bille ne traverse pas la plaque et si aucun éclat trop important n'est projeté. Ces tests mettent en jeu des phénomènes rapides (rupture du verre et de l'interface) et un profil de fractures complexe. La mise en place de mesures quantitatives est particulièrement difficile dans ces conditions. On ne peut donc pas, la plupart du temps, utiliser un tel test pour remonter à la source d'éventuels problèmes ou pour développer de nouveaux produits. C'est pour cette raison que des études précédentes ont cherché, entre autres, à relier des tests à l'échelle du laboratoire avec les résultats des tests normés ([5] et [9]). Cette relation s'est avérée difficile à mettre en œuvre et de nombreuses lacunes dans la compréhension des mécanismes de dissipation d'énergie lors de l'impact sont apparues.

Les évènements qui se succèdent au cours de l'impact sont à la fois complexes et

rapides. On peut cependant distinguer deux étapes principales (Figure 8.2). Durant les dix premières microsecondes de l'impact, un profil de fractures en étoile, assez nettement défini apparaît sous l'objet impactant. La plaque, à cet instant, n'est pas encore en flexion. Dans les microsecondes qui suivent, les fissures dans le verre propagent jusqu'au bord de la structure, rebondissent et, combinées à l'effet de la flexion de la plaque, génèrent le profil de fractures complexe que l'on observe post mortem. Durant cette deuxième étape, la flexion de la plaque conduit les morceaux de verres à s'écarter les uns des autres, en étirant entre eux l'intercalaire qui se décolle. C'est précisément, l'étirement de l'intercalaire qui permet de dissiper une grande quantité d'énergie lors de l'impact, comme l'a montré entre autres *Nourry* [8].

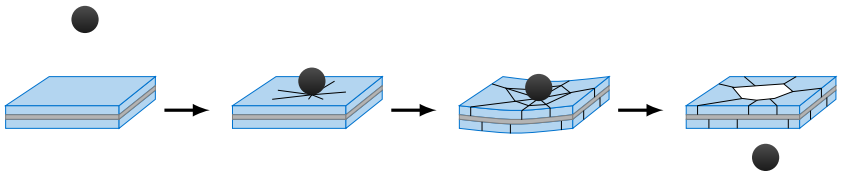

FIGURE 8.2 : Le déroulement d'un impact peut être décomposé en deux grandes étapes. Durant les premières micro secondes, la plaque n'est pas encore globalement en flexion, un profil simple de fissures en étoile apparaît sous l'objet impactant. Puis, un profil complexe de fissures se développe notamment sous l'effet de la flexion de la plaque. Cette flexion conduit par ailleurs à l'écartement des morceaux de verre et à l'étirement de l'intercalaire délaminé.

Dans cette thèse, nous nous sommes attachés à l'étude de cette étape de l'impact durant laquelle l'intercalaire délamine du verre et subit des déformations importantes. **Nous avons pour objectif de caractériser les liens entre le comportement de l'intercalaire et l'adhésion afin d'expliquer la quantité importante d'énergie dissipée lors de l'impact.**

Pour ce faire nous avons abordé le problème en considérant deux axes d'étude. Nous avons cherché d'une part à caractériser le comportement de l'intercalaire dans un régime de déformation et de vitesse approprié. D'autre part nous avons utilisé une expérience qui modélise l'écartement des morceaux de verre durant l'impact. Cette expérience nous a permis d'étudier les sollicitations imposées à l'intercalaire lors de sa délamination.

L'intercalaire le plus couramment utilisé dans les verres feuilletés est le Polyvinylbutyral ou PVB. Il s'agit d'un polymère statistique composé de 3 monomères : vinylacetate (1-2wt%), vinylalcool (18wt%) et vinylbutyral (80wt%). Le matériau,

qui n'est pas réticulé chimiquement, contient également 20% en masse de plastifiant. Les mesures du comportement en petites déformations permettent d'explorer une large gamme de fréquences et de températures. Elles montrent notamment que l'intercalaire PVB présente une large transition vitreuse autour de 25 °C ainsi qu'une dépendance en temps et températures qui peut être modélisée en utilisant la loi WLF. Lors de la délamination l'intercalaire est sollicité dans un régime de grandes déformations et il est donc nécessaire de caractériser le comportement de l'intercalaire dans cette gamme d'étirement. Pour cela des essais de traction uniaxiale sont réalisés à différentes températures et taux de déformation. Des essais cycliques (Figure 8.3) montrent que le PVB dissipe une quantité d'énergie qui représente jusqu'à 90% du travail fourni à basse température (10 °C) ou à grande vitesse de déformation ($1\,s^{-1}$). Dans cette gamme de températures et de taux de déformations, le polymère présente entre 10 et 40% de déformation un plateau de contrainte, ainsi qu'un fort raidissement au delà de 100% de déformation. A plus basse vitesse ($0{,}001\,s^{-1}$ ou à plus haute température 50 °C, le PVB dissipe moins d'énergie mais présente une extensibilité plus grande. On constate également que le comportement viscoélastique présente un moins fort raidissement et que le plateau de contrainte disparaît.

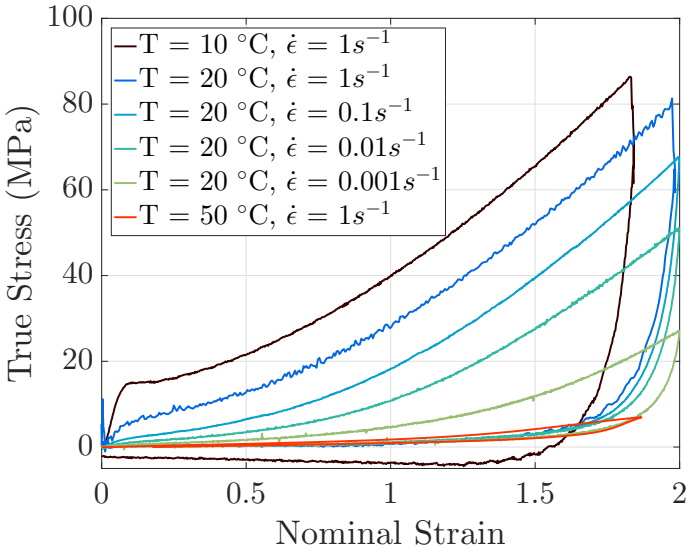

FIGURE 8.3 : Cycles en traction uniaxiale à différentes températures et taux de déformation jusqu'à 200% de déformation. Les vitesses de charge et de décharge sont identiques.

Afin de relier ce comportement à la structure du matériau, des mesures de biréfringences sont réalisées au cours des essais de traction. Pour cela l'échantillon de PVB, soumis à une traction uniaxiale, est placé entre deux polariseurs croisés. L'intensité de la lumière monochromatique traversant l'ensemble polariseurs/échantillon

est mesurée. L'intensité oscille entre des franges sombres et lumineuses qui reflètent l'orientation des chaines du matériaux et leurs interactions avec la lumière polarisée. En particulier, on remarque que le nombre de franges est d'autant plus grand que le taux de déformation est élevé ou que la température est basse. Ces observations font écho aux différences de comportement présentées précédemment. Mais l'image d'un polymère dont les chaines seraient non réticulées chimiquement et seulement enchevêtrées se heurte à d'autres observations. En effet, lors d'un essai de relaxation (charge puis maintien du niveau de déformation) on observe que, pendant que la contrainte relaxe rapidement, le niveau de biréfringence reste globalement constant (Figure 8.4). La relaxation de la contrainte suggère une relaxation du réseau polymère, au contraire le niveau de biréfringence constant invite à penser que les chaines restent orientées dans la direction de traction. Cette contradiction peut s'expliquer par la coexistence de deux réseaux interpénétrés.

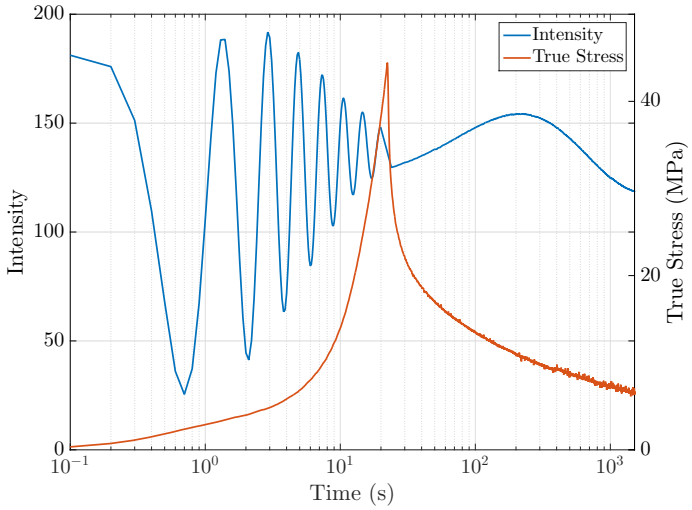

FIGURE 8.4 : Lors d'un essai de relaxation suivi par biréfringence on constate que la contrainte relaxe rapidement alors que le niveau de biréfringence varie peu après la montée en charge.

Cette hypothèse est étayée par différentes observations. Tout d'abord, des expériences de calorimétrie différentielle montrent qu'une perte d'organisation intervient autour de 70 °C (Figure 8.5).

Des mesures de diffraction de rayon X confirment l'existence d'une structure organisée. Cette structure pourrait s'expliquer, comme suggéré par *Schaefer* [23] par la présence de nodules de liaisons hydrogènes. On sait que les groupes hydroxyles des monomères vinylalcool sont susceptibles de former de telles liaisons entre les chaines du PVB. Il est probable que localement des amas de liaisons hydrogènes se forment. Ces nodules plus solides qu'une liaison hydrogène isolée, engendrent

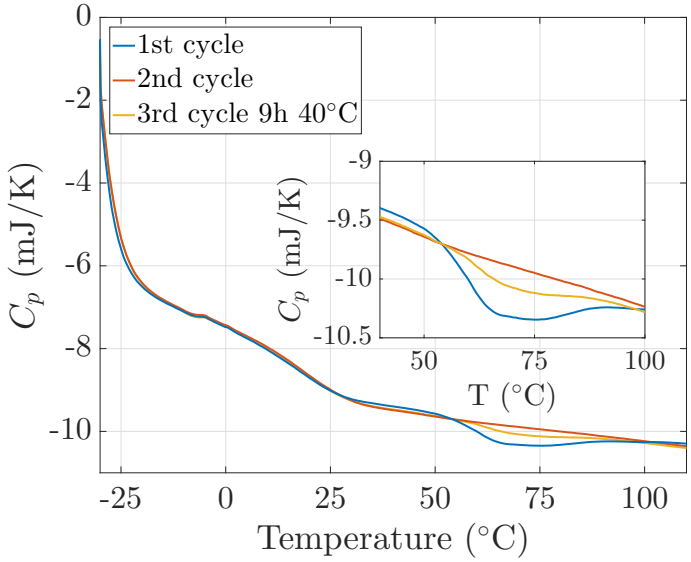

FIGURE 8.5 : La calorimétrie différentielle à balayage permet entre autre de mettre en évidence une transition ordre/désordre autour de 70 °C. Cette structure n'est recouvrée partiellement qu'après une attente de 9 h à 40 °C.

localement une organisation plus importante des chaines de polymère environnantes. Enfin les expériences de diffraction permettent d'estimer que la distance entre ces nodules est supérieure à 300 µm.

Cette description de la structure du PVB permet d'expliquer la grande quantité d'énergie dissipée lors de la déformation du matériau.

Ayant identifié les mécanismes de dissipation d'énergie dans le comportement de l'intercalaire, nous nous sommes intéressés à sa délamination du verre. Pour cela nous avons utilisé une expérience modèle consistant en une traction uniaxiale sur un verre feuilleté pré-entaillé ("Through Crack Tensile Test" ou TCTT), identique à celle conduite par *Seshadri* dans ses travaux [22] (Figure 8.7).

Nous avons tout d'abord établi que dans une certaine gamme de température et de vitesse, la délamination se fait de manière stationnaire. Dans ce régime, les fronts de délamination, relativement réguliers, progressent à vitesse constante. L'intercalaire est étiré entre ces fronts. Nous avons montré que de manière similaire au pelage d'un élastomère depuis un substrat rigide, la force de délamination et la déformation macroscopique de l'intercalaire atteignent rapidement un plateau. Notamment, le PVB est étiré à des niveaux de déformation de l'ordre de 150% à 20 °C et pour une vitesse de déplacement de 10 mm s^{-1} (Figure 8.8). Dans ce régime stationnaire nous avons montré que la délamination de l'intercalaire dépend de la vitesse de déplacement imposée et de la température.

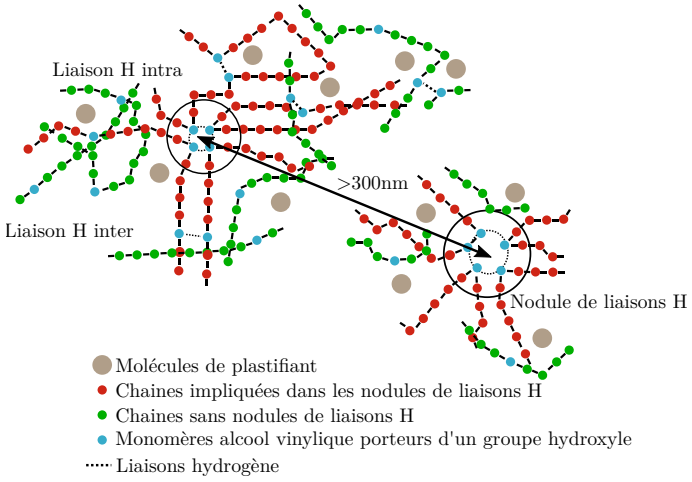

(a) Structure du PVB

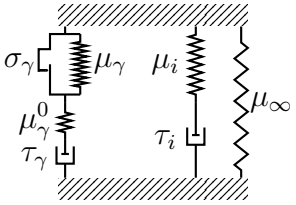

(b) Modèle rhéologique du PVB

FIGURE 8.6 : L'intercalaire présente une structure constituée de deux réseaux interpénétrés.

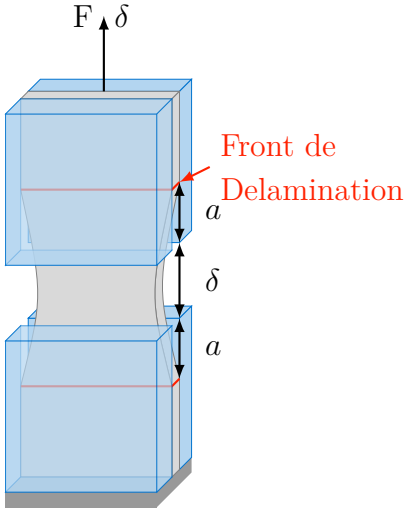

FIGURE 8.7 : Vue schématique de l'expérience modèle de délamination sur verre pré-entaillé : Through Crack Tensile Test.

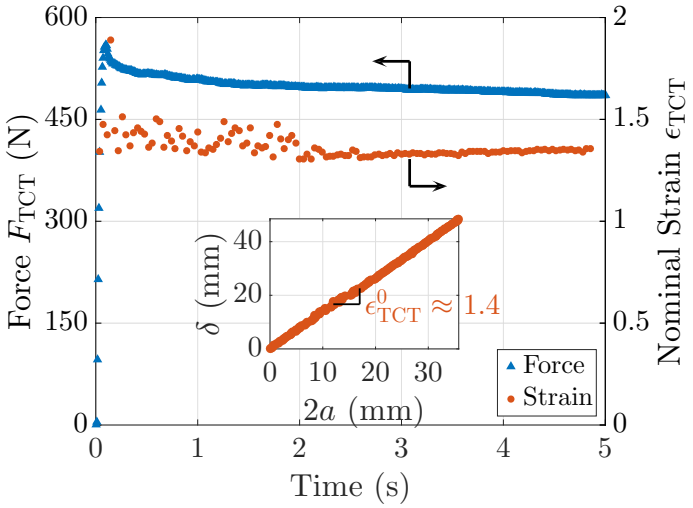

FIGURE 8.8 : Force de délamination et déformation de l'intercalaire sont constants au cours de la délamination stationnaire à 20 °C et 10 mm s^{-1}.

En revanche lorsque la température augmente ou lorsque la vitesse diminue, on observe un régime de délamination que nous qualifions d'instable. Dans ces conditions, les fronts ondulent et s'arrêtent conduisant à la rupture de l'intercalaire. À hautes vitesses et à basses températures, un problème différent empêche la mesure de la force de délamination et de la déformation. En effet, le polymère, plus fragile, devient plus sensible aux défauts de l'expérience et notamment à ceux introduits par un mauvais alignement des mors ou par la préparation de l'échantillon. Si la propagation semble d'abord similaire au régime stationnaire de délamination, la rupture de l'intercalaire met rapidement fin à l'expérience.

Dans le régime stationnaire, il nous est possible de calculer un travail de fracture appliqué loin du front à partir de la force et de la déformation du PVB. Ce travail, de l'ordre de 10 kJ m^{-2} est largement supérieur à l'énergie des liaisons hydrogènes qui constituent l'interface verre/polymère, de l'ordre de 0,01 kJ m^{-2}. Cette amplification de l'énergie dissipée est liée aux grandes déformations que subi le PVB. La Figure 8.9 montre l'évolution de ce travail en fonction de la température et de la vitesse de déplacement appliquée, ainsi que les différents régimes de délamination.

Afin de déterminer les différentes zones sur lesquelles l'intercalaire est sollicité lors de la délamination, nous avons montré que le travail de fracture loin du front est une fonction affine de l'épaisseur de l'intercalaire (Figure 8.10). On peut voir notamment sur cette figure que l'ordonnée à l'origine est loin d'être négligeable. Ce résultat suggère que ce travail peut être décomposé en une composante volumique et une composante surfacique. La partie volumique correspond à l'étirement d'un ligament de PVB et elle est caractérisée par la pente de la droite précédente (densité

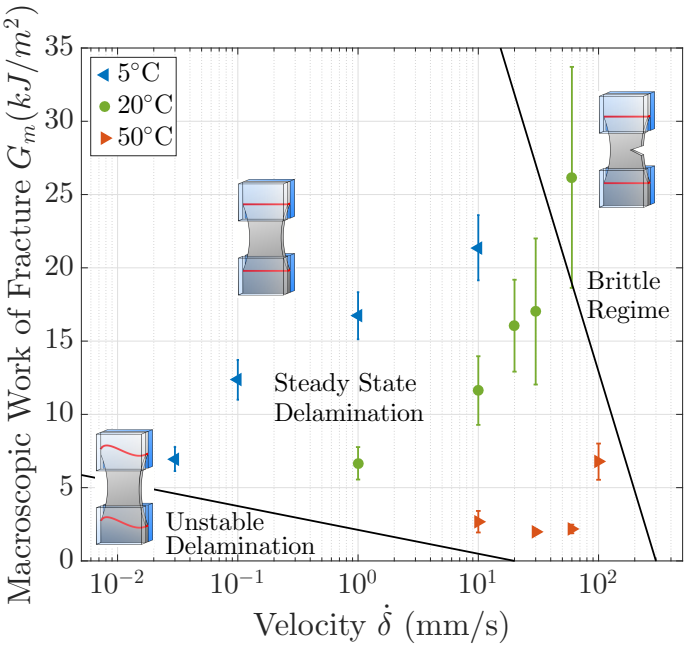

FIGURE 8.9 : Le travail fourni loin du front varie en fonction de la température et de la vitesse de déplacement imposée. Les limites entre les trois régimes de délamination sont également grossièrement indiquées sur cette figure.

d'énergie dissipée en volume Π_{bulk}). La partie surfacique correspond elle, non seulement à la rupture des liaisons hydrogènes à l'interface, mais aussi à la déformation de l'intercalaire à proximité du front de délamination. Cette dissipation au voisinage du front est caractérisée par l'ordonnée à l'origine Γ_{crack}.

C'est donc dans deux zones distinctes que le PVB est sollicité. La zone à proximité du front de délamination est difficilement observable expérimentalement. En revanche, nous avons pu caractériser la zone de déformation volumique de l'intercalaire en utilisant la corrélation digitale d'images. Nous avons pour cela déposé un mouchetis d'encre au milieu d'un empilement de deux feuilles d'intercalaire assemblées dans un verre feuilleté. Ces mesures nous ont permis de déterminer le champ de déformation sur le plan médian de l'expérience de délamination. Nous avons ainsi pu observer que l'intercalaire se déforme sur une distance égale à son épaisseur (Figure 8.11). Cette courte distance d'étirement associée au fort niveau de déformation et à la grande vitesse de délamination, implique des taux de déformation importants (de l'ordre de $3\,s^{-1}$ à $20\,°C$ pour une vitesse de déplacement imposée de $10\,mm\,s^{-1}$). Nous avons alors montré, que la sollicitation dans la zone d'étirement rapide de l'intercalaire pouvait être assimilée à un essai de traction uniaxiale, à une température et à un taux de déformation appropriés. Ce modèle fournit une méthode simple pour quantifier la densité d'énergie dissipée en volume par l'étirement du PVB lors de la

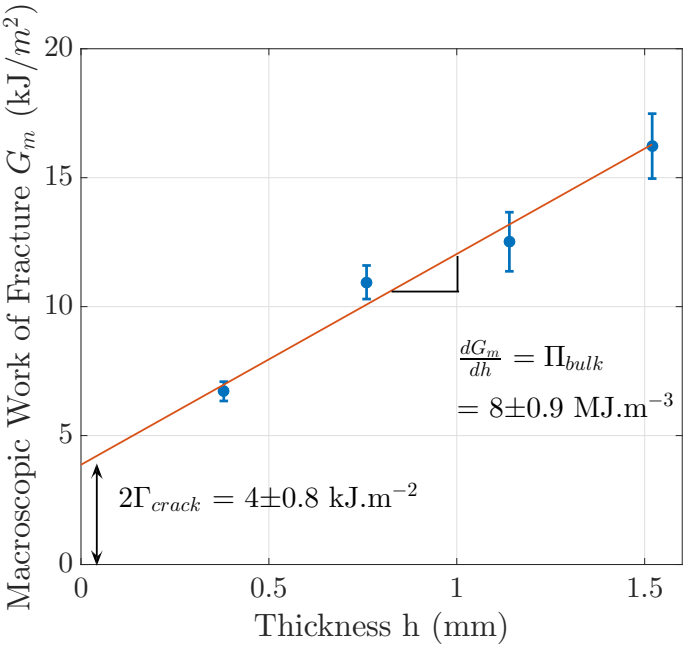

FIGURE 8.10 : Le travail fourni loin du front est un fonction affine de l'épaisseur suggérant qu'il existe deux zones de dissipation d'énergie : l'une où la dissipation provient de la déformation en volume de l'intercalaire, l'autre en relation avec les processus à proximité du front de délamination.

délamination.

Afin d'étudier l'impact du niveau d'adhésion sur ces mécanismes dissipatifs, il faut pouvoir modifier l'interface verre/polymère sans changer le comportement de ce dernier. Les travaux réalisés avec *Raphaëlle Kulis* dans le cadre de son stage de master [13] ont montré la possibilité de modifier l'adhésion en silanisant la surface du verre. Ainsi, le (3-Aminopropyl) triethoxysilane (APTS) permet d'augmenter fortement l'adhésion verre/PVB. Au contraire l'utilisation de l'Octyltriethoxysilane (OTES) la diminue sensiblement. Avec l'APTS, aucune rupture de l'interface n'a pu être observée en utilisant l'expérience de délamination. Dans le cas de la faible adhésion, une délamination stationnaire a pu être observée. Cependant le régime de délamination stationnaire semble être déplacé vers les basses températures et hautes vitesses en comparaison avec le niveau d'adhésion standard. Les expériences avec l'OTES, ont aussi montré qu'une adhésion plus faible conduisait, toutes choses égales par ailleurs, à des niveaux de déformation et de force plus faibles au cours de la délamination. Ainsi, l'énergie dissipée dans ce cas s'en trouve diminuée.

L'exploration de la délamination de l'intercalaire est approfondie à l'aide d'un modèle éléments finis. Des éléments cohésifs sont utilisés pour modéliser l'inter-

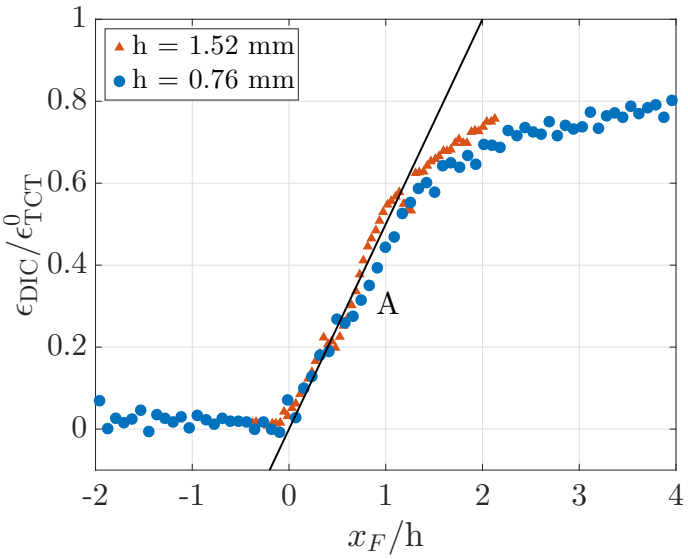

FIGURE 8.11 : La mesure par corrélation digitale d'image de la déformation, dans la direction de traction et à proximité du front, montre que l'intercalaire est étiré sur une distance égale à son épaisseur. L'amplitude de la déformation représente environ 60% de la déformation maximale. On a représenté ici, la déformation locale normalisée par la déformation loin du front en fonction de la distance à la verticale du front de délamination normalisée par l'épaisseur de l'intercalaire.

face pendant que l'intercalaire est modélisé comme un polymère viscoélastique non-linéaire. Cette modélisation partielle du comportement de l'intercalaire, ne permet pas de reproduire parfaitement l'expérience de délamination mais conduit tout de même à des résultats qualitatifs intéressants. Ce modèle a tout d'abord permis de confirmer certains résultats expérimentaux. On retrouve ainsi une délamination stationnaire, un niveau de force et de déformation loin du front constant et une longueur de la zone de déformation de l'intercalaire égale à son épaisseur. Le modèle confirme également la localisation des mécanismes dissipatifs dans deux zones distinctes spatialement : l'une en volume, l'autre à proximité du front de délamination (Figure 8.12). Dans cette deuxième zone, que nous n'avions pas pu explorer expérimentalement, l'intercalaire est principalement sollicité dans la direction orthogonale à l'interface. Ainsi, malgré l'application d'un déplacement en mode II, l'ouverture de l'interface se fait en mode I en raison de l'émoussement important de la fissure. Nous avons également pu estimer grâce à ce modèle l'énergie dissipée dans chaque zone. Enfin nous avons montré l'influence de différent paramètres comme l'adhésion, le comportement de l'intercalaire ou les conditions de chargement sur les différentes composantes de l'énergie dissipée. Cela nous a permis de mettre en évidence les relations existantes entre le chargement lointain et les processus locaux de dissipation

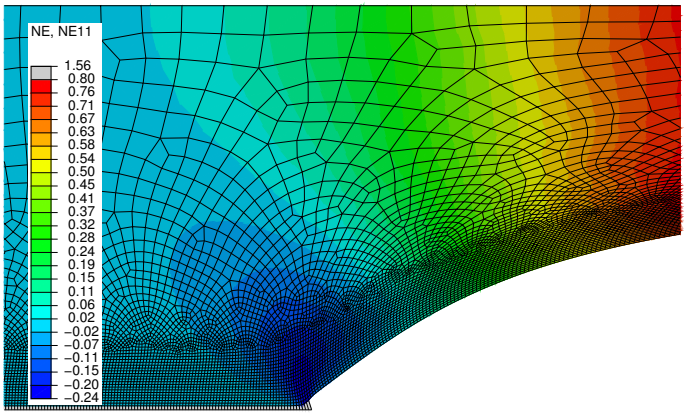

FIGURE 8.12 : Le modèle éléments finis permet entre autre de visualiser deux zones de dissipation spatiallement distinctes : l'une en pointe de fissure l'autre dans le volume du matériau. Ici, le champ de déformation dans la direction de traction (direction 1) présente un gradient positif le long de l'axe médian et dans le volume du ligament de polymère ainsi qu'un gradient négatif (contraction) au voisinage de la fissure

d'énergie.

La description de la structure de l'intercalaire et des mécanismes dissipatifs associés permettent d'imaginer l'utilisation de polymères présentant des liaisons physiques équivalentes à celle du PVB, pour le développement de nouveaux verres feuilletés. Par ailleurs l'étude de la délamination de l'intercalaire a permis d'identifier et de caractériser l'origine de la dissipation d'énergie lors d'un impact sur un verre feuilleté. Au delà de la volonté de confirmer certaines observations préliminaires, notamment en ce qui concerne l'influence de la modification de l'interface, les efforts futurs devront sans doute s'attacher à étudier l'influence de l'intercalaire sur les premiers instants de l'impact. La modélisation éléments finis que nous avons proposée ici est en outre très incomplète et un raffinement de la description du comportement de l'intercalaire ainsi que de la pointe de fissure sont envisageables.

Appendices

A Effect of the thermal treatment during laminated glass preparation on the mechanical behavior of the interlayer

Three different PVB were tested.

- Standard PVB as received (referred to as Standard PVB).
- PVB subjected to the heat treatment of the autoclaving process (1,5 h, 130 °C and 10 bar), in-between two pieces of glass put protected by a silicon film from adhesion to glass (referred to as Thermally treated PVB).
- PVB delaminated from the glass after the laminated glass assembly and the heat treatment of the autoclaving process (referred to as the Delaminated PVB).

Two mechanical tests were conducted. For small strain measurements, DMA experiments were conducted on a range of temperature from −40 °C to 60 °C (steps of 10 °C), for frequencies ranging from 0,1 Hz to 10 Hz. For large strain measurements, a uniaxial tension test was conducted at 20 °C and $1\,s^{-1}$ strain rate.

There is almost no differences between the standard PVB, the thermally treated PVB and the delaminated PVB. This also shows that the PVB, even after it has been subjected to large deformation during a delamination experiment (more than 100% deformation), does not present any plastic deformation and that it's behavior is the same after a few hours of recovery.

A small difference can be noted at long time for the DMA results. However, in the range of corresponding temperature from 50 °C to 60 °C the DMA starts to loose its accuracy and this difference is difficult to relate to an actual difference in the mechanical behavior.

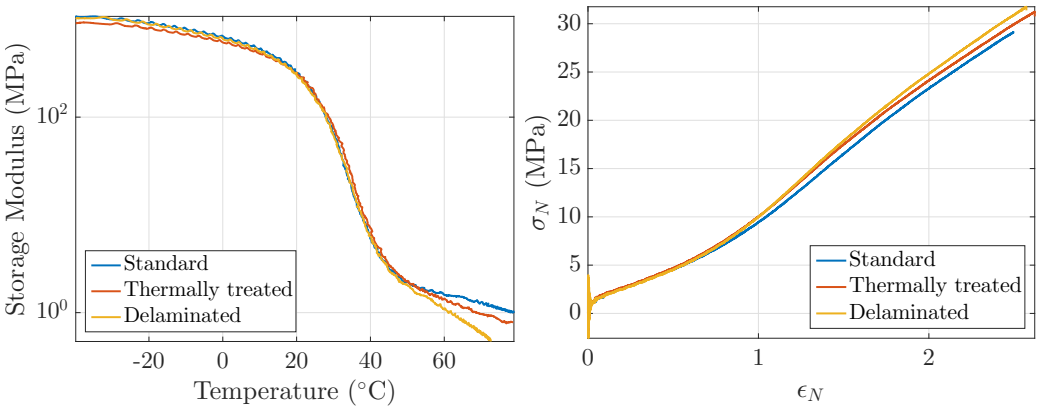

(a) DMA (b) Uniaxial tension

Figure 8.13: Comparison between the Standard PVB, a cured PVB and a delaminated PVB. No large difference was found on the small or large strain behavior.

B Arruda Boyce Model

A polymer chain can be seen as a collection of N monomer blocks of length l. The chain can then be described by the length r in between its two ends (Figure 8.14). This distribution of distance r is characterized by its probability density function. The initial chain length r_0 is simply given by a random walk of N steps of length l: $r_0 = \sqrt{N}l$

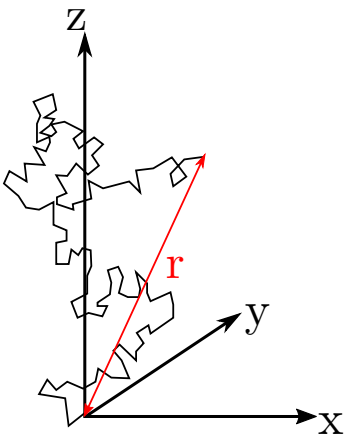

Figure 8.14: Polymer chain in a random position that can be described by different statistical model. (after [64])

This function can be a Gaussian probability but in this case one has to assume that the chain is always far from its complete extension $r_l = Nl$. In order to describe the chain extensibility statistic at high strains, a Langevin statistic can be used [64].

However, these model describe a single chain outside of the network. Hence,

Flory [65] and Treloar [66] were using a tetrahedral model of the network in which, three polymer chains are connected together in the center of a tetrahedron on one end and at the summit of the tetrahedron on the other end. When a deformation is applied on this small network all the chain will be stretched according to the choosen probability. However, due to the anisotropic nature of the initial chain orientation, the system entropy is difficult to calculate as it requires to average the different orientation contributions. Thus, Arruda and Boyce used a eight chain model (Figure 8.15), which present a cubic symmetry regarding the principal direction of stretch.

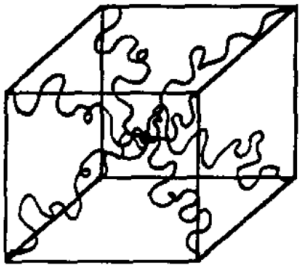

Figure 8.15: The eight chain network model used by Arruda and Boyce [16].

We can first define the extension of the chain as $\frac{r}{Nl}$ which is defined by the Langevin function:

$$r/Nl = \coth\beta - 1/\beta \tag{B.1}$$

β is the inverse Langevin function $\beta = \mathcal{L}^{-1}(\frac{r}{Nl})$. Treloar [66] gives the logarithmic probability density $p(r)$:

$$\ln p(r) = c - N\left(\frac{r}{Nl}\beta + \ln\frac{\beta}{\sinh\beta}\right) \tag{B.2}$$

with c a constant. From this probability density, the probability $P(r)$ is obtained by

$$P(r)\mathrm{d}r = 4\pi r^2 p(r)\mathrm{d}r \tag{B.3}$$

From this the entropy is defined by $s = k\ln p(r)$:

$$s = c' - kN\left(\frac{r}{Nl}\beta + \frac{\beta}{\sinh\beta}\right) \tag{B.4}$$

with c' another constant.

This result is given for a single chain. If we denote n the chain volumic density,

as all chain are equivalent, the global entropy is: $S = ns$. Finally, the Helmholtz free energy is:

$$W = T\Delta S = NkTn\left(\frac{r}{Nl}\beta + \ln\frac{\beta}{\sinh\beta}\right) - Tc'' \tag{B.5}$$

with c'' an other constant and T the temperature.

Now this model is used inside the eight chain network model. In this network model, the length of the chain at a given state of stretch is given by:

$$r = \frac{1}{\sqrt{3}}\sqrt{N}l(\lambda_1^2 + \lambda_2^2 + \lambda_3^2)^{1/2} = \frac{1}{\sqrt{3}}\sqrt{N}lI_1^{1/2} \tag{B.6}$$

where I_1 is the first invariant $I_1 = \lambda_1^2 + \lambda_2^2 + \lambda_3^2$ and the λ_i the stretch in direction i. Moreover, the stretch of the chain is defined as $\lambda_{chain} = r/r_0 = r/\sqrt{N}l$ and it can now be written $\lambda_{chain} = \frac{1}{\sqrt{3}}I_1^{1/2}$

By using equation B.5, one gets:

$$W = nkT\sqrt{N}\left(\lambda_{chain}\beta + \ln\frac{\beta}{\sinh\beta}\right) - Tc'' \tag{B.7}$$

As the Langevin function is not so easy to use and to differentiate to get the stress expression, most of the time the following approximation is used:

$$\begin{aligned} W =& nkT\left(\frac{1}{2}(I_1 - 3) + 2\frac{1}{20N}(I_1^2 - 9) + 3\frac{11}{1050N^2}(I_1^3 - 27)\right) \\ &+ nkT\left(4\frac{19}{7000N^3}(I_1^4 - 81) + 5\frac{519}{673750N^4}(I_1^5 - 243)\right) \end{aligned} \tag{B.8}$$

We call the maximal chain extensibility λ_m which is given by $\lambda_m = Nl/\sqrt{N}l = \sqrt{N}$ and μ the shear modulus given by $\mu = nkT$. For a uniaxial traction test in direction 1 $\lambda_1 = \lambda$ and for an incompressible material $\lambda_1\lambda_2\lambda_3 = 1$ we get the following expression of the stress:

$$\begin{aligned} \sigma =& \lambda\frac{\mathrm{d}W}{\mathrm{d}\lambda} \\ =& 2\mu\left(\lambda - \frac{1}{\lambda^2}\right)\sum_{i=1}^{5}\frac{iC_iI_1^{i-1}}{\lambda_m^{2(i-1)}}. \end{aligned} \tag{B.9}$$

Where the C_i are the coefficients of the Langevin function: $C_1 = 1/2$, $C_2 = 1/20$, $C_3 = 11/1050$, $C_4 = 19/7000$ and $C_5 = 519/673750$.

Bibliography

[1] Jean-Marie Michel. Contribution à l'histoire industrielle des polymères en france : l'histoire du verre triplex, 2012.

[2] European Committe for Standardization. European Standard – EN 12600. Glass in building - Pendulum test - Impact test method and classification for flat glass., 2003.

[3] European Committe for Standardization. European Standard – EN 356. Glass in building - Security glazing - Testing and classification of resistance against manual attack., 2000.

[4] J.R. Huntsberger. Adhesion of plasticized poly(vinyl butyral) to glass. *Journal of Adhesion*, 13:107–129, 1981.

[5] B. Vidal. *Modélisation d'impacts sur vitrages feuilletés.* PhD thesis, Ecole supérieure d'Arts et Métiers, 1998.

[6] F.W. Flocker and L.R. Dharani. Stresses in laminated glass subject to low velocity impact. *Eng. Struc.*, 19(10):851–856, 1997.

[7] P.A. Hooper, R.A.M. Sukhram, B.R.K. Blackman, and J.P. Dear. On the blast resistance of laminated glass. *Int. Journ. Sol. Struc.*, 49:899–918, 2012.

[8] E. Nourry. *Comportement des vitrages feuilletés.* PhD thesis, Ecole supérieure d'Arts et Métiers, 2005.

[9] R. Decourcelle. *Comportement mécanique des vitrages feuilletés sous chargements statiques et dynamiques.* PhD thesis, Université de Rennes 1, 2011.

[10] J. Chen, J Xu, X. Yao, Liu B, X. Xu, Y. Zhang, and Y. Li. Experimental investigation on the radial and circular crack propagation of PVB laminated glass subject to dynamic out-of-plane loading. *Engineering Fracture Mechanics*, 112–113:26–40, 2013.

[11] J. Chen, X Xu, Yao, X. Xu, B. Liu, and Y. Li. Different driving mechanisms of in-plane cracrack on two brittle layers of laminated glass. *International Journal of Impac Engineering*, 69:80–85, jul 2014.

[12] S. Muralidhar, A. Jagota, S.J. Bennison, and S. Saigal. Mechanical behaviour in tension of cracked glass bridged by an elastomeric ligament. *Acta Materialia*, 48:4577–4588, 2000.

[13] R. Kulis. Role of the pvb/glass adhesion on the behaviour of laminated glass. Master's thesis, École polytechnique féédérale de Lausanne, 2016.

[14] Malcolm L. Williams, Robert F. Landel, and John D. Ferry. The temperature dependence of relaxation mechanisms in amorphous polymers and other glass-forming liquids. *Journal of the American Chemical Society*, 77(14):3701–3707, 1955.

[15] E. Wiechter. Gesetze der elastischen nachwirkung für constante temperatur. *Annalen der Physik*, 286(10):335–348, 1893. Annalen der Physick published by Wiley in 2006.

[16] E.M. Arruda and M.C. Boyce. A three dimensional constitutive model for the large stretch behavior of rubber elastic materials. *Journal of the Mechanics and Physics of Solids*, 41(2):389–412, 1993.

[17] L.R.G. Treloar. The photo-elastic properties of rubber. part i.: Theory of the optical properties of ststrain rubber. *Transaction of the Faraday Society*, 43:277–284, 1947.

[18] F. Mertz. *Etude de la synthèse et de la caractérisation du Polyvinylbutyral. Influence des caractéristiques du polymère sur la structure des films. Répartition de l'Eau au sein des Films plastifiés.* PhD thesis, ENSCMu, 1992.

[19] D. Klock. *Contribution à l'étude des feuilletés verre-polymère: synthèse et structure du poly(vinylbutyral) en relation avec ses propriétés mécaniques et adhésives.* PhD thesis, ENSCMu, 1989.

[20] P.A. Hooper and B.R.K. Blackman. The mechanical behavior of poly(vynil butyral) at different strain magnitudes and strain rates. *Journal of Material Science*, 47:3564–3576, 2012.

[21] J. Xu, Y. Sun, B. Liu, M. Zhu, X. Yao, Y. Yuan, Y. Li, and C. Xi. Experimental and macroscopic investigation of dynamic crack patterns in PVB laminated glass sheets subject to light-weight impact. *Engineering Failure Analysis*, 18:1605–1612, 2011.

[22] M. Seshadri. *Mechanics of glass-polymer laminates using multi-length scale cohesive zone Models.* PhD thesis, Carnegie Mellon University, Department of civil and environmental engineering, Carnegie Mellon University, June 2001.

[23] J. Schaefer, J.R. Garbow, E.O. Stejskal, and J.A. Lefelar. Plasticization of poly(butyral-co-vinyl alcohol). *Macromolecules*, 20(6):1271–1278, 1987.

[24] M. Sonego, L.C. Costa, and J.D. Ambrosio. Flexible thermoplastic composite of polyvinyl butyral (pvb) and waste of rigid polyurethane foam. *Scientific technical*, 25(2):175–180, 2015.

[25] J.S. Bergstrom and M.C. Boyce. Constitutive modeling of the large strain time-dependent behavior of elastomers. *Journal of Mechanics and Physics of Solids*, 46(5):931–954, 1998.

[26] I. Lapczyk and J.A. Hurtado. A viscoelastic-elastoplastic finite strain framework for modeling polymers. In *ASME 2014 International Mechanical Engineering Congress and Exposition*, page 10, 2014.

[27] J. Pelfrene, S. Van Dam, and W. Van Paepegem. Numerical analysis of the peel test for characterisation of interfacial debonding in laminated glass. *International Journal of Adhesion and Adhesives*, 62:146–153, 2015.

[28] A. Jagota, S.J. Bennison, and C.A. Smith. Analysis of a compressive shear test for adhesion between elastomeric polymers and rigid substrates. *International Journal of Fracture*, 104:105–130, 2000.

[29] M. Seshadri, S. Saigal, A. Jagota, and S.J. Bennison. Scaling fracture energy in tensile debonding of viscoelastic films. *Jour. App. Phys.*, 101:1–7, 2007.

[30] Y. Sha, C. Y. Hui, E.J. Kramer, P.D. Garret, and J.W. Knapczyk. Analysis of adhesion and interface debonding laminated safety glass. *Journal of adhesion science and technology*, 11:49–63, 1997.

[31] M. Overend, C. Butchart, H. Lambert, and M. Prassas. The mechanical performance of laminated hybrid glass units. *Composite Structures*, 110:163–173, 2014.

[32] S. Nhamoinesu and M. Overend. Simple models for predicting the post fracture behaviour of laminated glass. In *In the Proceedings of the XXV A.T.I.V 2010, International Conference, Parma, Italy*, 2010.

[33] D. Delincé, D. Sonck, J. Belis, D. Callewaert, and R. Van Impe. Experimental investigation of the local bridging behaviour of the interlayer in broken laminated glass. In *International Symposium on the Application of Architectural Glass*, pages 41–49, Munich, 2008.

[34] S. Malcikan. *Numerical Momodell of adhesive failure in delamination of laminated glass*. PhD thesis, Gent Universiteit, Faculteit Ingenieurswetenshappen en Architectuur, 2013.

[35] C. Butchart and M. Overend. Delamination in fractured laminated glass. In *International Conference at glasstec, Düsseldorf, Germany*, 2012.

[36] D. Ferretti, M. Rossi, and G. Royer-Carfagni. Through crack tensile delamination tests with photoelastic measurements. In IOS Press, editor, *Challenging Glass 3 - Conference on Architectural and Structural Application of Glass*, pages 641–652, 2012.

[37] R.A. Schapery. A theory of crack initiation and growth in viscoelastic media : I. theoretical development. *Int. Journ. of Fracture*, 11:141–159, 1975.

[38] P.G. de Gennes. Fracture d'un adhésif faiblement réticulé. *C.R. Acad. Sci. Paris*, 307(2):1949–1953, 1988.

[39] F. Saulnier, T. Ondarçuhu, A. Aradian, and E. Raphaël. Adhesion between a viscoelastic material and a solid surface. *Macromolecules*, 37:1067–1075, 2004.

[40] A.N. Gent. Adhesion and strength of viscoelastic solids. is there a relationship between adhesion and bulk properties? *Langmuir*, 12:4492–4496, 1996.

[41] E. Barthel and C. Fretigny. Adhesive contact of elastomers: effective adhesion energy and creep function. *Journal of Physics D: Applied Physics*, 42:195302–195311, 2009.

[42] C. Creton and M. Ciccotti. Fracture and adhesion of soft materials: A review. *Rep. Prog. Phys.*, 79(4):046601, 2016.

[43] B.Z. Newby and M.C. Chaudhury. Effect of interfacial slippage on viscoelastic adhesion. *Langmuir*, 13(6):1805–1809, 1997.

[44] N. Amouroux, J. Petit, and L. Leger. Role of interfacial resistance to shear stress on adhesive peel strength. *Langmuir*, 17(21):6510–6517, 2001.

[45] B. Cotterell and J.K. Reddel. The essential work of plane stress ductile fracture. *International journal of fracture*, 13(3):267–277, 1977.

[46] F.M. Fowkes, D.W. Dwight, J.A. Manson, T.B. Lloyd, D.O. Tichler, and B.A. Shah. Enhancing mechanical properties of polymer composites by modification of surface acidity or basicity of fillers. In Materials Research Society, editor, *MRS Proceedings*, volume 119, pages 223–235, 1988.

[47] R. Faure and A. Lecointre. Overview of silanes use as a monolayer in sgr. Technical Report SGR/PCRS – RF/SR – N0293/15, Saint-Gobain Recherche, 2015.

[48] A. Miller and J. Berg. Effect of silane coupling agent adsorbate structure on adhesion performance with a polymeric matrix. *Composites Part A: Applied Science and Manufacturing*, 34(4):327–332, 2003.

[49] Y.Y. Lin and H.Y Chen. Effect of large deformation and material nonlinearity on the JKR (Johnson–Kendall–Roberts) test of soft elastic materials. *Journal of Polymer Science Part B: Polymer Physics*, 44(19):2912–2922, 2006.

[50] P. Rahulkumar, A. Jagota, S.J. Bennison, S. Saigal, and S. Muralidhar. Polymer interfacial frature simulation using cohesive elements. *Acta Materialia*, 47:4161–4169, 1999.

[51] D.S. Dugdale. Yielding of steel sheets containing slits. *J. Mech. Phys. Solids.*, 8:100–104, 1960.

[52] V. Tvergaard and J. W. Hutchinson. The influence of plasticity on mixed mode interface toughness. *Journal of the mechanics and physics of solids*, 41(6):1119–1135, 1993.

[53] X.P. Xu and A. Needleman. Void nucleation by inclusion debonding in a crystal matrix. *Modelling and simulation in materials science and engineeering*, 1(2):111–132, 1993.

[54] P.P. Camanho and C.G. Davila. Mixed-mode decohesion finite elements for the simulation of delamination in composite materials. Technical report, NASA, 2002.

[55] J.F. Faou, G. Parry, S. Grachev, and E. Barthel. Telephone cord buckles – a relation between wavelength and adhesion. *Journal of the mechanics and physics of solids*, 75:93–103, 2015.

[56] Y.F. Gao and A.F. Bower. A simple technique for avoinding convergence problems in finite element simulations of crack nucleation and growth on cohesive interfaces. *Modelling and simulation in materials science and engineering*, 12:453–463, 2004.

[57] C. Atkinson and J. D. Eshelby. The flow of energy into the tip of a moving crack. *International Journal of Fracture Mechanics*, 1968.

[58] J.R. Rice. A path independent integral and the approximate analysis of strain concentration by notches and cracks. *Journal of Applied Mechanics*, 35:379–386, 1968.

[59] A.F. Bower. *Applied Mechanics of Solids*. CRC Press Taylor and Francis, 2010.

[60] R.H. Dean and J.W. Hutchinson. Quasi-static steady crack growth in small scale yielding. *Fracture Mechanics: 12th Conference ASTM STP*, 700:383–405, 1980.

[61] R. Villey, C. Creton, P.P. Cortet, M.J. Dalbe, T. Jet, B. Saintyves, S. Santucci, L. Vanel, D.J. Yarusso, and M. Ciccotti. Rate dependent elastic hysteresis

during the peeling of pressure sensitive adhesives. *Soft Matter*, 11(17):3480–3491, 2015.

[62] C.M. Landis, T. Pardoen, and J.W. Hutchinson. Crack velocity dependent toughness in rate dependent materials. *Mechanics of Materials*, 32:663–678, 2000.

[63] N. Vandenberghe, R. Vermorel, and E. Villermaux. Star-shaped crack pattern of brocken windows. *Physical Review Letters*, 110:174302–1–5, 2013.

[64] W. Kuhn and F. Grun. Beziehungen zwischen elastischen konstanten und dehnungsdoppelbrechung hochelastischer stoffe. *Kolloid-Zeitschrift*, Volume 101(3):248–271, 1942.

[65] P.J. Flory and Jr. Rehner. Statistical mechanics of cross-linked polymer networks i. rubberlike elasticity. *The journal of chemical physics*, 11:512–520, 1943.

[66] L.R.G. Treloar. The elasticity of a network of long-chain molecules iii. *Transactions of the Faraday Society*, 42:83–94, 1946.

Laminated glass: dynamic rupture of adhesion

Laminated glass has been discovered more than a century ago. It is composed of a polymeric interlayer sandwiched in-between two glass plies. This interlayer dramatically enhances the performance during impact. Even if the glass breaks, the partial delamination and the stretching of the interlayer will dissipate a large amount of energy. This dissipation will protect people from the impacting object while the glass splinters will stick on the interlayer, preventing harmful splinters projection. During my PhD work, I have identified and characterized the dissipation mechanisms associated with the interlayer rheology and its delamination from glass.
The interlayer behavior was studied using uniaxial tension tests combined with photoelastic measurements. A model experiment was developed to study the interlayer stretching during its delamination from glass. This test consists in a uniaxial tension on a pre-cracked laminated glass sample. Finally, digital image correlation measurements were used to quantify the stretching of the interlayer ahead of the delamination fronts.
The different dissipating mechanisms of the interlayer rheology have been identified. A rheological model was developed to link this behavior to the polymer macromolecular structure. The model delamination experiment displayed a steady state delamination regime in a certain range of applied velocities and temperatures. In these steady state conditions, two zones of dissipation have been identified. Large strains and high strain rates in these two zones explain the large amount of dissipated energy during delamination. Finally, a finite element model has been developed to confirm experimental observations and to describe the close vicinity of the delamination fronts.

Keywords: Adhesion, Laminated Glass, Rupture, Interface, Viscoelasticity, Large strain

Verre feuilleté : rupture dynamique d'adhésion

Il y a plus d'un siècle que les verres feuilletés ont été découverts. Il s'agit d'une structure formée d'un intercalaire polymère pris entre deux plis de verre. Cet intercalaire améliore considérablement les performances à l'impact de l'assemblage. Ainsi, même si le verre se brise, la délamination et l'étirement de l'intercalaire dissipent une grande quantité d'énergie. Les personnes sont protégées par cette dissipation de l'objet impactant qui ne traverse pas le verre feuilleté, mais aussi des projections potentiellement dangereuses d'éclats de verre. Au cours de cette thèse, nous avons identifié et caractérisé les mécanismes de dissipation d'énergie associés au décollement de l'intercalaire et à l'étirement qui s'en suit.
Le comportement de l'intercalaire a été étudié en relation avec sa structure macromoléculaire à l'aide de test de traction uniaxiale couplés à des observations de biréfringence. Nous avons par ailleurs utilisé une expérience modèle afin d'établir les sollicitations subies par l'intercalaire lors de sa délamination du verre. Cette expérience consiste en un essai de traction uniaxiale sur un verre feuilleté pré-entaillé. Enfin des mesures de corrélation digitale d'images ont permis de quantifier la dynamique de déformation de l'intercalaire en aval du front de délamination.
Les différents mécanismes dissipatifs du comportement de l'intercalaire ont été identifié. Un modèle rhéologique a été développé afin de relier le comportement de l'intercalaire à sa structure. L'expérience sur le verre pré-entaillé a montré l'existence d'un régime de délamination stationnaire dans une gamme limitée de température et de vitesse de déplacement imposée. Dans ces conditions stationnaires, nous avons identifié deux zones de dissipation d'énergie. L'amplitude et la vitesse de sollictiation dans ces deux zones permettent d'expliquer la grande quantité d'énergie dissipée observée lors de la délamination. Enfin à l'aide d'un modèle éléments finis nous avons confirmé les observations expérimentales et décrit le voisinage du front de délamination.

Mots clés : Adhésion, Verre feuilleté, Rupture, Interface, Viscoélasticité, Grandes déformations